NORTHWESTERN UNIVERSITY

Five Projects in Pattern Formation, Fluid Dynamics and Computational Neuroscience

A DISSERTATION

SUBMITTED TO THE GRADUATE SCHOOL
IN PARTIAL FULFILLMENT OF THE REQUIREMENTS

for the degree

DOCTOR OF PHILOSOPHY

Field of Applied Mathematics

By

Alexander C. Roxin

EVANSTON, ILLINOIS

December 2003

ABSTRACT

Five Projects in Pattern Formation, Fluid Dynamics and Computational Neuroscience

Alexander Roxin

This dissertation is a compilation of five projects, which span the fields of pattern formation, fluid dynamics and computational neuroscience. The first two chapters deal with spatio-temporal patterns that may arise in various spatially extended systems driven far from equilibrium. In the first, the interaction of dispersionless traveling waves with a long-wave mode is studied, revealing two distinct instabilities, one of the phase and the other of the amplitude of the traveling waves. The amplitude-driven instability can lead to localized pulses in some cases. In the second the effect of anisotropy in rotating convection is investigated using a phenomenological Swift-Hohenberg equation. Stability results from an amplitude-equation approach are used to explain spirals and targets seen in experiment.

In the third chapter the question of fluid slip at a solid interface is addressed at a molecular scale using methods from solid-state physics and nonlinear dynamics theory. We propose a modification of the well-known Frenkel-Kontorova model based on results from molecular dynamics simulations. The resulting dynamics explain the phenomenon of slip as the motion of defects in the fluid layer adjacent to the solid.

The fourth and fifth chapters enter the realm of computational neuroscience. The fourth chapter discusses how CA1 pyramidal neurons in the hippocampus actively integrate their two principal excitatory inputs. Extensive numerical simulations using NEURON with realistic morphological data reveals that dendritic sodium spikes may forward-propagate to the soma causing a somatic action potential if the inputs are sufficiently synchronous. The final chapter introduces a model of excitable integrate-and-fire neurons in a small-world network, a network with regular, local coupling and a number randomly placed, long-range connections. The ensemble average of the network dynamics exhibits a transition from persistent activity to failure as a function of the density of global connections. Patterns of activity can be periodic or chaotic depeding on parameters and the network is bistable in the persistent regime.

ACKNOWLEDGEMENTS

First and foremost I thank my thesis advisor Hermann Riecke for his patience and guidance. My collaboration with him has taught me much, not only about how to conduct research, but about the role of a researcher more broadly.

I thank all those people with whom I've had the pleasure of working: Bill Kath, Seth Lichter, Shreyas Mandre, Hermann Riecke, Sara Solla, and Nelson Spruston. I also thank the Spruston lab for their hospitality and for humoring me.

I appreciatively acknowledge the support and funding of the NSF-IGERT grant "Dynamics of Complex Systems in Science and Engineering" and those faculty members who run the program day to day. Thanks also to Judy Piehl and Edla D'Herckens for all of their help during my stay in the Department of Engineering Sciences and Applied Mathematics.

I would also like to acknowledge the following grants: Engineering Research Program of the Office of Basic Energy Sciences at the Department of Energy (DE-FG02-92ER14303), NSF (DMS-9804673), NSF-IGERT fellowship through grant DGE-9987577.

Finally, I reserve my deepest gratitude to my girlfriend Libertad who taught me that putting in a full day at work is not the same as leading a full life.

Contents

List of Figures

Chapter 1

Introduction

Most of the work presented in this dissertation is an outgrowth of my involvement in the NSF IGERT-funded program 'Dynamics of Complex Systems'. In line with the motivation behind the program itself, the present work addresses nonlinear phenomena in very different fields. The diversity of topics makes an in-depth review of the relevant literature for each individual topic too lengthy an undertaking. Therefore I have restricted myself to a very brief introduction for each project at the start of each chapter. In this general introduction, therefore, I will not discuss the content of each project, but rather my contribution to each one as well as the contribution of others.

The first project is entitled "Traveling Waves in an Advected Field". The project was begun by my advisor Hermann Riecke, who derived the model of traveling waves coupled to an advected field. He also carried out much of the analysis for the linear instability associated with the phase of the traveling waves. I completed this analysis, and extended it to the instability associated with the amplitude of the pattern. All numerical simulations were carried out with pre-existing code written by Glen

Granzow.

The second project, “Modulated Rotating Convection”, is work motivated by a presentation given by Prof. Guenter Ahlers at the 2001 American Physical Society Meeting, Division of Fluid Dynamics. The model Swift-Hohenberg equation and the framework for analysis were devised by Hermann Riecke and myself, and all numerical simulations were carried out with pre-existing code written by Glen Granzow and Fil Sain. I conducted the linear and weakly-nonlinear analysis both analytically and numerically, with my own code.

The third project, “Slip at a Liquid-Solid Interface”, began as an IGERT project course in 2001. Seth Lichter, who concieved of the project, formulated the model and provided an intellectual framework, has worked with Shreyas Mandre and myself. Shreyas Mandre has written and carried out all Molecular Dynamics simulations, while I have studied the Frenkel-Kontorova model both analytically and numerically. Seth Lichter has guided our efforts and provided the fluid-mechanical insight necessary to present our results meaningfully.

The fourth project, “Interaction of Schaeffer Collateral and Temporo-Ammonic Inputs in a Model of a CA1 Pyramidal Cell”, is work done in collaboration with Nelson Spruston and Bill Kath. The bulk of the model was written by Bill Kath. My contribution was to add synapses and a graphical-user-interface to control the synaptic input. Nelson Spruston crucially guided the modeling effort with his expertise in the electrophysiology of CA1 pyramidal cells.

The last project, “Excitable Integrate-and-Fire Neurons in a Small-World Network” is work done in collaboration with Hermann Riecke and Sara Solla. The project was motivated to some extent by the IGERT project course taught by Hermann Riecke and Sara Solla in 2002. The relevance of the mean-field result by Neuman, Moore and Watts was pointed out by Sara Solla and Hermann Riecke. My contribution has been to carry out numerical simulations and analyze the resulting data. The result concerning the distribution of failure rates, equation (6.29) was derived by Hermann Riecke, as was the notion of the pathways of activity shown in figure 6.21.

Chapter 2

Traveling Waves in an Advected Field

2.1 Overview of Small-Amplitude Waves in Fields

Nature presents us with unending examples of complex patterns such as waves on the ocean surface or stripes on a tiger's fur. The theory of pattern formation has proven successful in explaining how such patterns arise in non-equilibrium systems. Essentially, as some parameter of the system is varied, correlations emerge in space or time or both on a scale over which the system was previously homogeneous. Mathematically, the correlations are related to a linear instability of a given solution. The ultimate evolution of the instability and resulting pattern depends on the nonlinear nature of the system. Near the onset of the instability one can examine this evolution quantitatively by means of a multiple-scale analysis. Near onset, the dynamics depend essentially only on the symmetries of the system and the nature of the instability. Therefore one can study a given system and then extend the results to other different systems with the same symmetries.

This project examines the interaction of small-amplitude traveling waves, arising through a spatio-temporal instability, with an additional, weakly-damped mode that is homogeneous in space, to leading order. Various systems have been shown to exhibit bifurcations to spatially periodic patterns in the presence of an additional, weakly damped mode. If that mode corresponds to a conserved quantity, it constitutes a true zero mode as in, e.g., translation of the fluid interface in two-layer Couette flow [1] or a shift in the displacement velocity of seismic waves in a viscoelastic medium [2]. Examples of weakly damped modes include the large-scale concentration field in binary-fluid convection [3, 4] or the real, slow mode in the 4-species Oregonator model of the Belousov-Zhabotinsky (BZ) reaction [5]. The evolution of instabilities in these and similar systems will be coupled to the dynamics of the weakly-damped mode. Within the context of a weakly nonlinear approach near onset of the pattern-forming instability, the Ginzburg-Landau model is altered through the coupling to an evolution equation for the additional mode. The precise form of the coupling depends on the physics and symmetries of the system.

Steady instabilities in conserved systems with and without reflection symmetry have been considered. With reflection symmetry the instability, setting in at finite wavenumber, was found by Mathews and Cox [6] to be amplitude-driven, leading to a supercritical modulation of the underlying pattern. In the absence of reflection symmetry, Malomed [2] identified modulated patterns by deriving longwave equations for the phase of the underlying pattern coupled to the zero-mode. A particle-in-a-potential model in a moving frame was then derived for the local wavenumber, which admits both traveling and steady modulations. Ipsen and Sørensen [5] investigated the effect of a real, slow mode in reaction- diffusion systems near a supercritical Hopf bifurcation. They found that the slow mode leads to new finite-wavenumber instabilities which alter traditional Eckhaus and Benjamin-Feir stability criteria for periodic waves. Barthelet and Charru [7] studied instabilities of interfacial waves in two-layer Couette-Poiseuille flow with Galilean invariance and no reflection symmetry, where the zero-mode is a shift of the fluid interface. The corresponding model of waves coupled to the zero-mode, derived and worked out by Renardy and Renardy [8], results in multiple, separated stability regions for periodic waves in contrast to the Eckhaus stable band exhibited by a single Ginzburg-Landau equation. The critically damped mode corresponding to a two-dimensional mean-flow in stress-free convection becomes relevant for not too large values of the Prandtl number. Bernoff [9] derived a Ginzburg-Landau equation coupled to the mean-flow mode from the Bousinesq equations and calculated the skew-varicose and oscillatory skew-varicose stability boundaries. This calculation brought into agreement previous work by both Siggia and Zippelius [10] and Busse and Bolton [11], who investigated the effect of mean-flow modes with non-zero vertical vorticity on the stability of rolls in Rayleigh-Benard convection.

In binary-fluid convection, Riecke [3] derived an amplitude equation for traveling waves arising in a Hopf bifurcation coupled to a critically damped mode related to large-scale modulations of the concentration field in the limit of small Lewis number. Instabilities of periodic waves within these equations were found to lead to localized traveling pulses which exhibited the anomalous slow drift observed in experiment [12], and in numerical simulations [13]. Riecke and Granzow presented a similar model on phenomenological grounds to describe the dynamics of traveling waves in electroconvection in nematic liquid crystals [14]. This model for oblique (zig and zag) waves coupled to a slow mode, possibly corresponding to a charge-carrier mode, exhibits instabilities to localized, worm-like structures as seen in experiment [15]. A striking feature of the worms is that although the extended waves bifurcate supercritically from the basic, conductive state, the worms themselves are bistable with the latter.

In the present chapter, we consider traveling waves arising in a supercritical Hopf-bifurcation coupled to a real, slowly varying field. The field is advected by the waves and, in turn, can affect the dynamics of the waves through coupling to their growth rate. We briefly introduce the model and present a brief linear analysis in section 2, which reveals distinct phase and amplitude instabilities of the waves. In sections 3 and 4 we are concerned with characterizing the linear and nonlinear behaviors of the phase and amplitude instabilities, respectively. In both cases we derive an envelope equation for the instability near its threshold and compare the results to full numerical simulations of the original equations. The envelope equations, in agreement with the numerics, indicate that the phase-instability leads to a backward Hopf bifurcation, while the amplitude-driven instability leads to modulated waves, arising super- or subcritically. In the latter case, the subcritical branch can be bistable with the basic, conductive state and localized wave pulses arise.

2.2 The Extended Ginzburg-Landau Equations

We consider a model of a traveling wave with complex amplitude A and group velocity s coupled to a real, weakly damped mode C. The general form of the equations to orders η^3, η^4 respectively, where η is a measure of the distance from threshold of the bifurcation to traveling waves ($a_1 = O(\eta^2)$), is dictated by symmetry,

$$\begin{aligned}
\partial_t A + s\partial_x A &= d_1\partial_x^2 A + (a_1 + a_2 C)A - b|A|^2 A, && (2.1)\\
\partial_t C &= d_2\partial_x^2 C - a_3 C + a_4 C^2 + (h_1 + h_2 C)|A|^2 + h_3|A|^4 + h_4\partial_x|A|^2 + h_5\partial_x^2|A|^2 \\
&\quad + h_6 i(\bar{A}\partial_x A - A\partial_x\bar{A}) + h_7 i\partial_x(\bar{A}\partial_x A - A\partial_x\bar{A}) + h_8\partial_x A\partial_x\bar{A}. && (2.2)
\end{aligned}$$

The coefficients d_1, a_1, a_2, b in (1) are, in general, complex. All coefficients can be calculated for a particular system through a perturbative, normal-mode expansion of the relevant variables with slowly varying amplitudes,

$$\mathbf{\Phi} = \eta(\mathbf{u}A(x,t)e^{i(q\tilde{x}+\omega\tilde{t})} + c.c.) + \eta^2(\mathbf{v}C(x,t) + ...) + h.o.t. \qquad (2.3)$$

We consider a field C that relaxes to a unique state in the absence of forcing by the wave and thus consider the contribution of the term proportional to a_4, which could introduce a second branch through a transcritical bifurcation, to be of higher order. We furthermore focus on the effect of advection by the traveling waves on C by retaining only the gradient coupling in (2.2). Thus, we eliminate the effect of spatially homogenous forcing and that of the curvature of the magnitude of the pattern-amplitude on the field C by setting the coefficients h_1 and h_5 to 0, respectively. The remaining terms express the wavenumber-dependence of h_1 and h_4, as can be seen by considering an expansion of the wavenumber-dependent coefficient $h_1 = h_1(q)$

about the critical wavenumber of the pattern at onset, q_c,

$$h_1(q) = h_1(q_c) + \partial_q h_1(q_c)(q - q_c) + \frac{1}{2}\partial_q^2 h_1(q_c)(q - q_c)^2 + h.o.t. \tag{2.4}$$

The local wavenumber is given by the gradient of the underlying phase, and thus $(q - q_c) = \partial_x \phi$, where $A(x,t) = R(x,t)e^{i\phi(x,t)}$. Representing the complex amplitude in such a form and plugging it into (2.2) yields for the terms proportional to h_6 and h_8,

$$\begin{aligned}
h_6 i(\bar{A}\partial_x A - A\partial_x \bar{A}) &= h_6 i(\bar{A}\partial_x\phi\partial_\phi A - A\partial_x\phi\partial_\phi \bar{A}), \\
&= h_6 i\partial_x\phi(\bar{A}\partial_\phi A - A\partial_\phi \bar{A}), \\
&= h_6 i(q - q_c)(i|A|^2 + i|A|^2), \\
&= -2h_6(q - q_c)|A|^2. && (2.5) \\
h_8\partial_x A\partial_x \bar{A} &= h_8(\partial_x\phi)^2\partial_\phi A\partial_\phi \bar{A}, \\
&= h_8(q - q_c)^2|A|^2. && (2.6)
\end{aligned}$$

Comparison of (2.5, 2.6) with (2.4) reveals $h_6 = -\frac{1}{2}\partial_q h_1(q_c)$ and $h_8 = \frac{1}{2}\partial_q^2 h_1(q_c)$. The coefficient h_7 analogously expresses the wavenumber-dependence of h_4 and, as such, is a higher-order effect. Furthermore we also simplify (2.1) by assuming real-valued coefficients, thereby neglecting dispersion. It should be mentioned that neglecting dispersion in (2.1) means ignoring the Benjamin-Feir instability as well as other possible destabilizing mechanisms. In addition, an imaginary contribution to the coefficient a_2 has been shown to destabilize periodic patterns [16].

However, models retaining solely the advective mechanism have proven fruitful in explaining certain qualitative features of localized patterns, as in, e.g., binary-fluid convection and electroconvection in nematic liquid crystals ([3], [14]). As a side-note, in the case of thermal binary-fluid convection it turns out that the term proportional to h_1, which is formally of lower order than the gradient term, only contributes at higher order [17]. Of course, in systems where C corresponds to a conserved quantity certain terms like those involving h_1, h_2, h_3 and h_5 are not allowed and the gradient coupling is the relevant forcing [1], [6].

Based on the abovementioned considerations, we investigate in this chapter the following system,

$$\begin{aligned} \partial_t A + s\partial_x A &= \partial_x^2 A + (a + C)A - |A|^2 A, & (2.7) \\ \partial_t C &= \delta\partial_x^2 C - \alpha C + h\partial_x |A|^2, & (2.8) \end{aligned}$$

in which $h_1 = h_5 = h_6 = h_7 = h_8 = 0$. Equations (2.7, 2.8) describe the dynamics of a traveling wave without dispersion, which advects a real, slowly varying field C. The strength and sign of advection is given by the coefficient h. No homogeneous scaling is possible in these equations due to the presence of gradient terms which contribute to lower order in the limit of large-scale modulations. The scalings $\partial_x = O(\eta), \partial_t = O(\eta^2)$ require $s = O(\eta), h = O(\eta)$ for strict validity of (2.7,2.8), indicating small group velocity and weak coupling. Modulations on a longer length scale ($\partial_x = O(\eta^2)$) allow for O(1) values of s and h although the diffusive terms now contribute at higher order. The system thus becomes hyperbolic in this limit. Counterpropagating waves near onset have been studied in the hyperbolic limit [18], and can exhibit both sub- and supercritical secondary bifurcations as well as more complex dynamics. In this chapter we choose not to reduce the equations (2.7,2.8) to a simpler form in a distinguished limit by fixing the scale. Instead we retain all terms as O(1) quantities and consider the equations as a phenomenological model of traveling waves coupled to a critically damped mode. It is, however, noteworthy that the most interesting instability of waves in (2.7, 2.8) is also captured in the abovementioned, asymptotically correct, hyperbolic limit (cf. discussion after eq. (2.21)), and will therefore also be relevant in realistic systems in which, quite generally, the group velocity s and coupling h are order one quantities.

Our goal is to identify instabilities of waves in (2.7,2.8) and characterize their nonlinear evolution. We note that in the absence of coupling (h=0) or in the limit of rapid decay of the C-field ($\alpha \to \infty$) (2.7,2.8) reduce to a single Ginzburg-Landau equation which exhibits a long-wave phase instability for waves with wavenumber $q^2 > \frac{a}{3}$. We shall refer to (2.7,2.8) as the extended Ginzburg-Landau equations (EGLE).

The complex amplitude A in (2.7) can be described by its real magnitude and phase $A = Re^{i\theta}$. Thus, in a frame moving with the waves (2.7,2.8) can be decomposed into the three following coupled equations,

$$\begin{aligned} \partial_t R &= \partial_x^2 R + R[(a + C) - R^2 - (\partial_x \theta)^2], && (2.9) \\ R^2 \partial_t \theta &= \partial_x [R^2 \partial_x \theta], && (2.10) \\ \partial_t C &= \delta \partial_x^2 C - \alpha C + s \partial_x C + 2hR\partial_x R. && (2.11) \end{aligned}$$

To determine instabilities of the traveling waves we linearize about the wave solution by considering an ansatz,

$$
\begin{aligned}
R &= \sqrt{a-q^2} + \tilde{R}e^{ipx+\sigma t}, &(2.12)\\
\theta &= qx + \tilde{\theta}e^{ipx+\sigma t}, &(2.13)\\
C &= \tilde{C}e^{ipx+\sigma t}. &(2.14)
\end{aligned}
$$

We first consider instabilities in the longwave limit by expanding the growth rate σ for small p. The three eigenvalues, corresponding to the real amplitude, phase and C-field respectively, are,

$$
\begin{aligned}
\sigma_{amp}(p) &= -2R^2 - 2\frac{ihR^2}{(2R^2-\alpha)}p \\
&\quad -\frac{[4R^6\beta - 2shR^4\alpha + (R^2+2q^2)(2R^2-\alpha)^3]}{R^2(2R^2-\alpha)^3}p^2 + O(p^3), &(2.15)\\
\sigma_{phase}(p) &= -D_E p^2 + 2\frac{ihq^2}{\alpha R^2}p^3 - 2\frac{q^2[\beta + \frac{\alpha^2 q^2}{R^4}]}{\alpha^2 R^2}p^4 + O(p^5), &(2.16)\\
\sigma_{field}(p) &= -\alpha + \frac{i(2R^2(s+h) - s\alpha)}{(2R^2-\alpha)}p \\
&\quad -\frac{[-4R^4\beta + 2shR^2\alpha + (2R^2-\alpha)^3\delta]}{(2R^2-\alpha)}p^2 + O(p^3). &(2.17)
\end{aligned}
$$

Here $R^2 = a - q^2$ is the amplitude of the plane wave and,

$$
D_E = \frac{R^2 - 2q^2}{R^2}. \qquad (2.18)
$$

The parameter $\beta = h(s+h)$ is introduced for simplicity; it will prove to be useful in characterizing the type of instability.

We notice that to leading order, the eigenvalues corresponding to the amplitude (2.15) and advected field (2.17) are negative for finite values of R^2 and α. The critical mode, corresponding to the phase, exhibits a longwave instability when the diffusion coefficient D_E changes sign; this occurs at the Eckhaus curve $q^2 = \frac{a}{3}$. However, the coupling of the advected field now raises the possibility of the quartic order term balancing the quadratic term in (2.16) as $D_E \rightarrow 0$. This would indicate a small-, yet finite-wavenumber instability. [1]

Indeed, within the longwave limit (2.16), a necessary condition for this phase instability to occur is that $\beta + \frac{\alpha^2 q^2}{R^4} < 0$. Figure 1(a) shows the eigenvalue of the phase mode which exhibits this finite- wavenumber instability, i.e. sufficiently small wavenumbers are damped. In Figure 1(c) we see the corresponding linear stability diagram. Here plane waves become linearly unstable already before the Eckhaus curved is reached. However, we note that near onset of the traveling waves, i.e. as $a \rightarrow 0$ for finite α, (2.7, 2.8) can be rescaled, and C adiabatically eliminated to yield a single Ginzburg-Landau equation. In this limit the contribution of the C-field is formally of higher order and we recover the Eckhaus instability (cf. Fig. 2.2(a), below).

We next consider waves which are phase-stable in this regime ($D_E \gg p^2$ or $\beta + \frac{\alpha^2 q^2}{R^4} > 0$ or both). In the limit as $\alpha \rightarrow 0$, the eigenvalue corresponding to the C-field can become positive through a balance between the leading order term and that at $O(p^2)$. Consider, for example, the eigenvalues at bandcenter (q=0),

---

[1] Strictly speaking, one should consider the distinguished limit in which both $p, D_E \rightarrow 0$ and the ratio $\frac{p^2}{D_E} \rightarrow k$ where k is a constant. Then, stability is determined based on whether $k \gtrless k^*$ (cf. eq. (2.29))

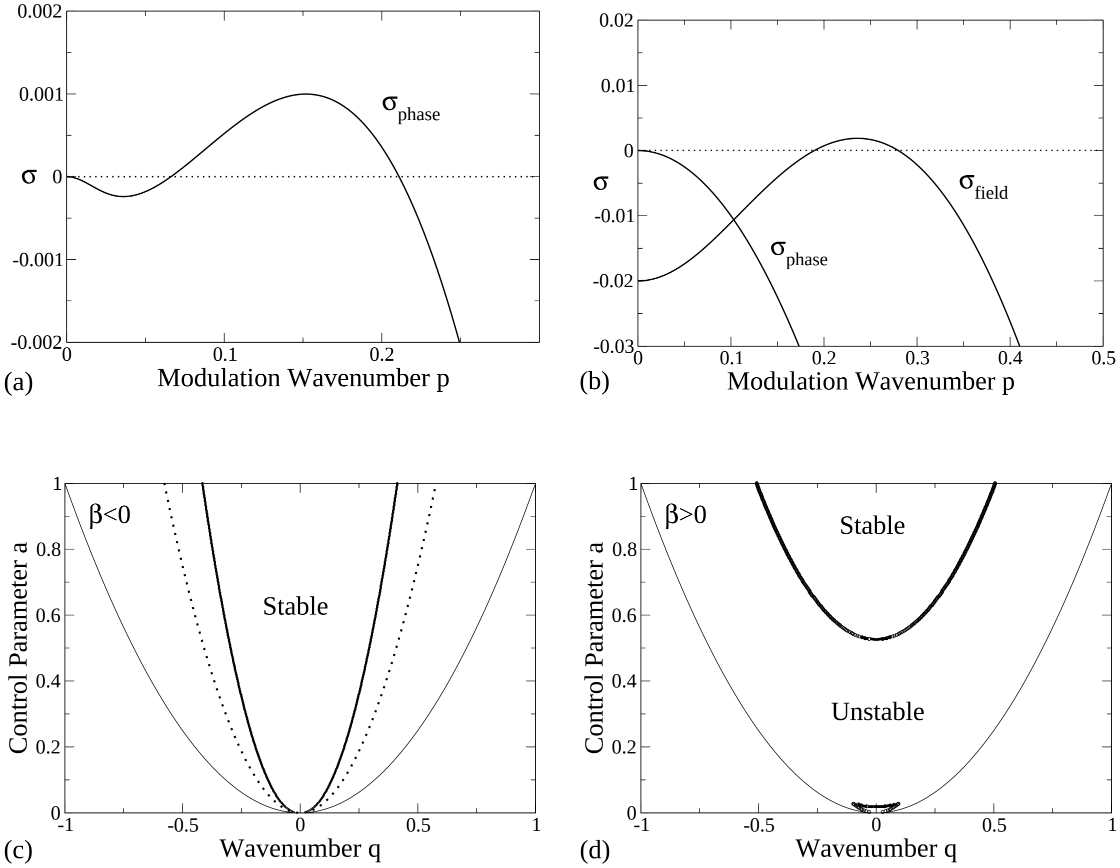

Figure 2.1: For all 4 figures h=1, α=0.02, δ=1.0 In (a) s=-1.5, q=0.425, a=1.0. This is a shortwave phase instability. The other two eigenvalues are large and negative. In (b) s=1.0, q=0, a=0.5. This is a shortwave instability of the C-field. The phase-eigenvalue is marginal for p=0 due to translation symmetry while the amplitude-eigenvalue is large and negative. (c) is the linear stability diagram for the values of the coefficients given in (a). The dotted line is the Eckhaus curve, given here for comparison. (d) is the linear stability diagram for the same coefficients as in (b).

$$\sigma_{amp}(p) = -2a - 2\frac{iha}{(2a-\alpha)}p - \frac{[4a^2\beta - 2sha\alpha + (2a-\alpha)^3]}{(2a-\alpha)^3}p^2 + O(p^3), \tag{2.19}$$

$$\sigma_{phase}(p) = -p^2, \tag{2.20}$$

$$\begin{aligned}\sigma_{field}(p) &= -\alpha + \frac{i(2a(s+h) - s\alpha)}{(2a-\alpha)}p \\ &\quad - \frac{[-4a^2\beta + 2sha\alpha + (2a-\alpha)^3\delta]}{(2a-\alpha)^3}p^2 + O(p^3).\end{aligned} \tag{2.21}$$

While for finite a as $\alpha \to 0$, both the amplitude and phase eigenvalues are stable, the field-eigenvalue can become unstable if $-4\beta + 8a\delta < 0$. This condition can only be satisfied for $\beta > 0$ and implies additionally that there is an upper bound on the control parameter a for fixed β and δ above which this instability cannot exist ($a_{bound} = \frac{\beta}{2\delta}$). Such a case is seen in Figure 2.1(b), where the eigenvalue corresponding to modulations of the C-field indicates positive growth for finite-wavenumber perturbations. The linear stability diagram Figure 2.1(d) confirms the existence of the linear instability over a finite range of the control parameter a, resulting in a small stability-island near onset. Here we also note that a linear stability analysis of (2.7, 2.8) in the asymptotically correct, hyperbolic limit yields, in its longwave limit, the same expression (2.21) for σ_{field} with $\delta = 0$. Thus the instability persists in this limit.

As β passes from negative values through zero, the linear stability diagram given in Figure 2.1(c) changes continuously to that shown in 2.1(d). The intermediate regime is not captured analytically in the longwave expansions we have used thus far and must be investigated numerically. Figure 2.2(b) shows how the region of linear stability of the traveling waves changes as β passes through zero. The stability boundary, outside of which the waves are phase-unstable to finite-wavenumber modulations for $\beta < 0$, develops a bottle-necked region which pinches off as β becomes more positive, resulting in two separated plane-wave-stable regions (cf. Fig.2.1(d)). This change is continuous, and there are values of β for which numerical simulations have revealed both phase- and amplitude-instabilities. That is, amplitude-modulated waves can arise whose underlying phase undergoes slips until a phase-stable wavenumber is achieved.

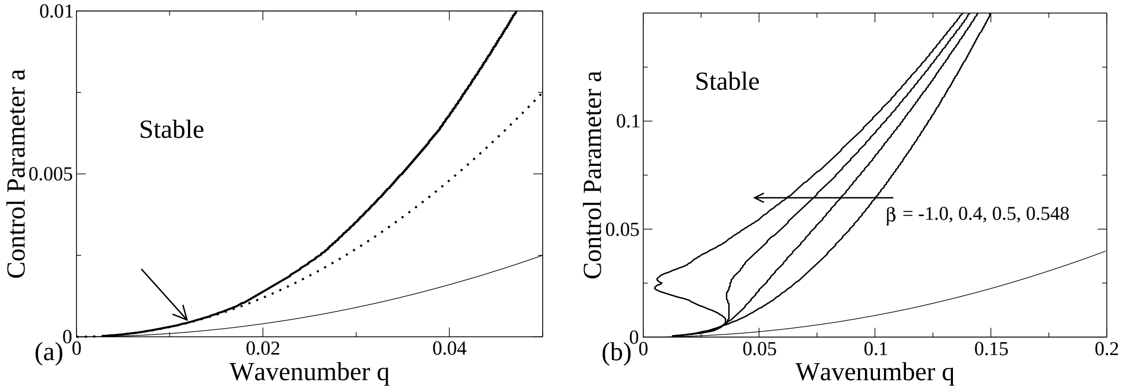

Figure 2.2: (a) Linear Stability diagram near threshold of the traveling waves ($a \ll 1$). The stability boundary approaches the Eckhaus curve as $a \to 0$ (arrow). (b) Linear stability diagram with h=1.0, α=0.02, δ=1.0, s=-1.1, -0.6, -0.5, -0.452. In this intermediate regime both phase and amplitude instabilities can set in.

2.3 Phase Instability

To facilitate the analysis of the phase instability, we make use of the large, negative eigenvalue of the magnitude of A to derive coupled phase and field equations in a longwave limit. If the longwave limit is taken at finite α, both the magnitude and the advected field can be adiabatically eliminated and, to leading order, one obtains the usual phase equation with the usual Eckhaus stability limit. The effect of the C-field can be captured, however, in a distinguished longwave limit in which $\alpha \to 0$ as well. Then the amplitude can be adiabatically slaved to the dynamics of the phase and C-field, given that we are sufficiently far from the neutral stability boundary ($R^2 \not\ll 1$).

We consider an ansatz of the form $A = R(T,X)e^{\frac{i}{\epsilon}\phi(T,X)}$, where $X = \epsilon x, T = \epsilon^2 t$, and additionally $\alpha = \epsilon^2 \alpha_2$. This scaling allows for large variations in the phase, although slow in time and space. To leading order we obtain an algebraic relationship relating the slaved amplitude to the C-field and local wavenumber,

$$R^2 = a + C - (\partial_X \phi)^2. \tag{2.22}$$

Combining equations at orders ϵ and ϵ^2 yields the longwave equations for the phase and the C-field,

$$\begin{aligned} \partial_T \phi &= D_E \partial_X^2 \phi + \frac{\partial_X \phi \partial_X C}{R^2}, && (2.23) \\ \partial_T C &= \delta \partial_X^2 C - \alpha_2 C + (s+h)\partial_X C - h\partial_X (\partial_X \phi)^2. && (2.24) \end{aligned}$$

The phase-diffusion coefficient D_E is defined as before (cf. (2.18)), where R^2 is now given by (2.22) and the local wavenumber is now given by the gradient of the phase, $q = \partial_X \phi$. As before, we linearize the longwave equations about the plane wave state with an ansatz,

$$\begin{aligned} \phi &= qX + \tilde{\phi} e^{ipX + \sigma T}, && (2.25) \\ C &= \tilde{C} e^{ipX + \sigma T}. && (2.26) \end{aligned}$$

The linearized longwave equations yield a complex, quadratic dispersion relation. As for the full EGLE, we expand the growth rate σ in powers of the modulation wavenumber p,

$$\sigma_{phase}(p) = -D_E p^2 + 2\frac{ihq^2}{R^2\alpha_2}p^3 - 2\frac{q^2\beta}{R^2\alpha_2^2}p^4 + O(p^5), \tag{2.27}$$

$$\sigma_{field}(p) = -\alpha_2 + i(s+h)p - \delta p^2 + O(p^3). \tag{2.28}$$

As expected, phase modes with infinitesimal wavenumber become unstable when D_E changes sign. However, according to (2.27), for $\beta < 0$ phase modes with finite wavenumber p become unstable already for $D_E > 0$ if

$$p^2 > 2D_E\frac{R^2\alpha_2^2}{q^2|\beta|}. \tag{2.29}$$

Thus, although we have identified the instability in the longwave limit, it is a shortwave instability and to determine the value of the critical modulation wavenumber p for which σ first passes through zero we must solve the dispersion relation exactly.

The action of the linearized operator of the longwave equations on (2.25, 2.26) yields a 2x2 matrix, the determinant of which must equal zero for a nontrivial solution to exist. If we consider the real and imaginary parts of the growth rate $\sigma = \sigma_r + i\omega$, this dispersion relation can be written as,

$$\sigma_r^2 + c_1\sigma_r + c_2 = 0, \tag{2.30}$$

$$c_3\sigma_r + c_4 = 0, \tag{2.31}$$

where

$$\begin{aligned} c_1 &= (p_1^2(D_E+\delta)+\alpha_2), && (2.32)\\ c_2 &= -\omega^2+\omega p(s+h)+p_1^2 D_E(p_1^2\delta+\alpha_2), && (2.33)\\ c_3 &= 2\omega-p(s+h), && (2.34)\\ c_4 &= \omega(p^2(D_E+\delta)+\alpha_2)-\frac{p^3}{h}(D_E(\beta-h^2)+h^2). && (2.35)\end{aligned}$$

At criticality ($\sigma_r = 0$), (2.31) and (2.35) yield the Hopf-frequency,

$$\omega_{Hopf} = \frac{p^3}{h}\frac{(D_E(\beta-h^2)+h^2)}{(p^2(D_E+\delta)+\alpha_2)}. \tag{2.36}$$

From equations (2.30) and (2.33) we arrive at a bi-cubic polynomial in p, the roots of which give the critical modulation wavenumber for the oscillatory instability,

$$\begin{aligned} &-p^4(D_E(\beta-h^2)+h^2)^2+p^2\beta(D_E(\beta-h^2)+h^2)(p^2(D_E+\delta)+\alpha_2)+\\ &h^2D_E(\delta p^2+\alpha_2)(p^2(D_E+\delta)+\alpha_2)^2=0. && (2.37)\end{aligned}$$

Solving for p directly in the sixth-order polynomial is not analytically feasible, but we note that the parameter β is merely quadratic in (2.37) and so seek a solution for β,

$$\begin{aligned}\beta_{1,2} &= -\frac{h^2(1-D_E)(p^2(\delta-D_E)+\alpha_2)}{2D_E(p^2\delta+\alpha_2)}\\ &\pm\frac{p(p^2(D_E+\delta)+\alpha_2)}{2D_Ep^2(p^2\delta+\alpha_2)}\sqrt{h^2p^2(1-D_E)^2-4D_E^2(p^2\delta+\alpha_2)^2}. && (2.38)\end{aligned}$$

It can be shown that $\sigma_r > 0$ only if the real quantity $\beta = h(s+h)$ is in the range $\beta_1 < \beta < \beta_2$. Thus, the finite-wavenumber instability can only arise if $\beta_{1,2}$ are real, requiring the discriminant to be positive, $h^2 p^2 (1-D_E)^2 > 4D_E^2(p^2\delta + \alpha_2)^2$. This can be interpreted as a constraint on the modulation wavenumber p,

$$|p^2 - \frac{h^2(1-D_E)^2 - 8D_E^2\delta\alpha_2}{8D_E^2\delta^2}| < \frac{h(1-D_E)}{8D_E^2\delta^2}\sqrt{h^2(1-D_E)^2 - 16D_E^2\delta\alpha_2}. \qquad (2.39)$$

This implies the additional constraint $h^2(1-D_E)^2 > 16D_E^2\delta\alpha_2$, which can be simplified to

$$q^2 > \frac{a}{3 + \frac{|h|}{2\sqrt{\alpha_2\delta}}}. \qquad (2.40)$$

This somewhat intricate analysis of (2.37) can now be summarized concisely. A *sufficient* condition for stability of the waves with respect to shortwave instabilities is that the underlying wavenumber of the waves be in the band given by $q^2 < \frac{a}{3+\frac{|h|}{2\sqrt{\alpha_2\delta}}}$, which is narrowed with respect to the traditional Eckhaus band. Thus, with respect to phase instabilities, the band of stable wavenumbers is bounded below by (2.40) and above by the Eckhaus curve,

$$\frac{a}{3 + \frac{|h|}{2\sqrt{\alpha_2\delta}}} < q^2_{phase} < \frac{a}{3}. \qquad (2.41)$$

If (2.41) is satisfied, there exists a range in β given by (2.38) for which the plane wave is unstable. For a given β from this range, the destabilizing modulation wavenumbers are given by the condition that the associated interval $[\beta_1, \beta_2]$ include that value of β.

In the limit of zero coupling ($h \to 0$) or large decay rate of the concentration field

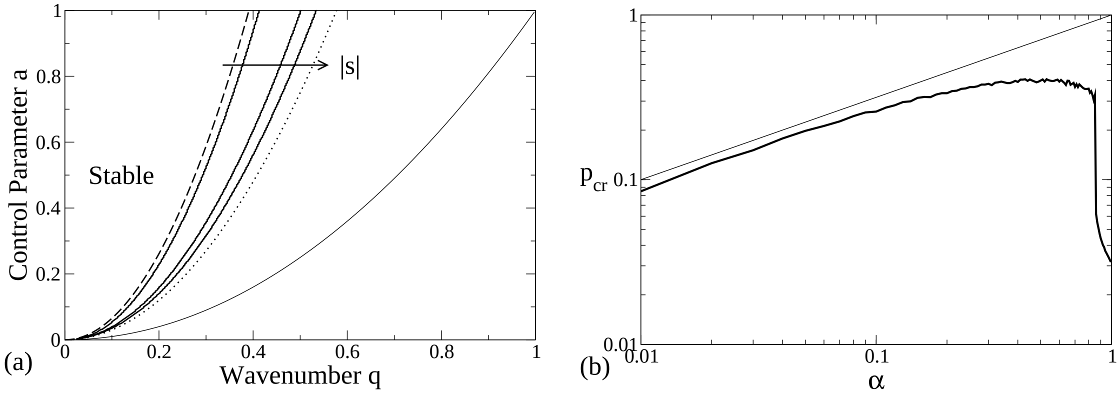

Figure 2.3: (a) Stability boundary as a function of the group velocity s. The boundary is bounded to the left by the stability condition derived from the dispersion relation of the longwave equations and to the right by the Eckhaus curve. Here h = 1, α = 0.02 δ = 1.0 and s = -1.5, -3.0, -5.0. (b) Dependence of the critical modulation wavenumber on the decay rate of C, α. The thick line is numerically calculated from the full dispersion relation while the thinner line is p=$\sqrt{\frac{\alpha}{\delta}}$. (2.43) is thus valid only for small enough α. (a=1.0, h=1.0, s=-1.5, δ=1.0)

($\alpha_2 \to \infty$), the Eckhaus band is recovered in a consistent manner. A linear stability diagram of waves as obtained from the full EGLE (2.7, 2.8) is shown in Figure 2.3(a) for various values of the group velocity s. It can be seen that inequality (2.41) is satisfied.

Weakly Nonlinear Analysis of Phase Instability

To examine the weakly-nonlinear behavior of the phase-instability one must solve (2.37) for given values of the system parameters. In the general case this yields a numerical value for the critical modulation wavenumber p which can then be used in a weakly-nonlinear analysis. The coefficients of the resulting amplitude equation must then be evaluated numerically. However, if we restrict the wavenumber of the waves to lie on the curve representing the lower bound of existence of the shortwave instability, we can obtain analytical values for the critical modulation wavenumber and Hopf-frequency and consequently also for the coefficients of the amplitude equation. Along that curve,

$$\begin{aligned}
q_{cr}^2 &= \frac{a_0}{3 + \frac{|h|}{2\sqrt{\alpha_2 \delta}}}, && (2.42)\\
p_{cr}^2 &= \frac{\alpha_2}{\delta}, && (2.43)\\
\omega_{cr} &= -\mathrm{sgn}(p_{cr} h) \frac{p_{cr}^2}{1 + \frac{4\sqrt{\alpha_2 \delta}}{|h|}}, && (2.44)\\
\beta_{cr} &= -4 p_{cr} \delta \left(1 - \frac{1}{2\delta (1 + \frac{4\sqrt{\alpha \delta}}{|h|})} \right). && (2.45)
\end{aligned}$$

It is good to keep in mind that these values fix a unique value of the parameter $\beta = h(s+h)$ given by (2.45) and are in this sense restrictive. In addition, (2.42-2.44) are obtained in a longwave analysis, which requires that $p, \alpha \ll 1$. Figure 2.3(b) indicates the values of α for which (2.42-2.44) are valid.

We expand the phase and C-field in small-amplitude, normal modes, where $\epsilon = \sqrt{\frac{(a-a_0)}{a_2}}$ is a measure of the distance from the bifurcation point (a_0, q_{cr}),

$$\begin{pmatrix} \phi \\ C \end{pmatrix} = \begin{pmatrix} q_{cr} X \\ 0 \end{pmatrix} + \epsilon \left[\begin{pmatrix} \Phi_0 \\ C_0 \end{pmatrix} A_0(\tau) e^{i(p_{cr} X + \omega_{cr} T)} + c.c + h.o.t. \right]. \qquad (2.46)$$

The complex amplitude A_0 of the unstable mode evolves on the superslow time scale $\tau = \epsilon^2 T$. Inserting this ansatz into (2.23, 2.24) and solving order by order leads

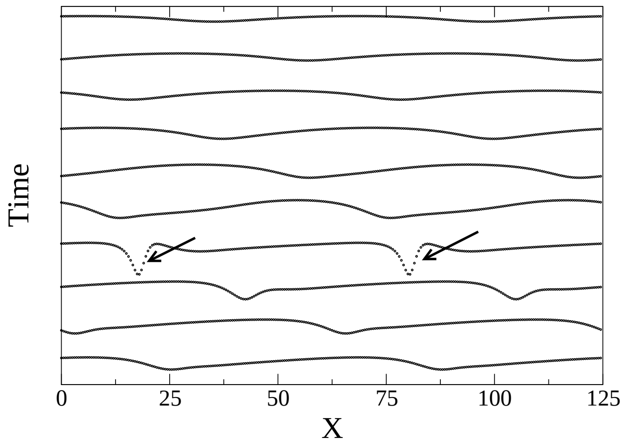

Figure 2.4: Space-time diagram of the evolution of the magnitude $|A|$ leading to a phase slip (arrows), here indicated by the dip in amplitude. s=-1.5, h=1 , α =0.02, δ =1.0

to a solvability condition at O(ϵ^3), which yields a differential equation for A_0,

$$\partial_\tau A_0 = -\Sigma(a_0, \alpha_2, \delta, h) a_2 A_0 + \Gamma(a_0, \alpha_2, \delta, h)|A_0|^2 A_0. \tag{2.47}$$

We are interested in the real part of the cubic coefficient, the sign of which gives the nature of the Hopf-bifurcation (forward/backward). The coefficient Γ is a complicated expression of δ, α_2, a, and h, but we can expand it for small α_2 to obtain an asymptotic approximation (α must be small from Figure 2.3(b)),

$$\begin{aligned}\Sigma &= \frac{1}{(2\delta+1)}\left(\frac{2|h|}{a_0^3\delta^{1/2}}\right)^{1/2}(1+i\mathrm{sgn}(h))\alpha_2^{3/4} + O(\alpha^{5/4}), &(2.48)\\ \Gamma &= \frac{1}{a^2\delta^{3/2}(2\delta+1)}\left(\frac{404}{5|h|}\alpha_2^{1/2} + i\mathrm{sgn}(h)\left[\frac{12}{\delta^{1/2}} + \frac{4}{5}\frac{(494\delta+451)}{(2\delta+1)}\alpha_2^{1/2}\right]\right)\alpha_2^3 \\ &\quad + O(\alpha_2^{9/4}). &(2.49)\end{aligned}$$

Thus in the limit $\alpha_2 \to 0$, $Re(\Gamma)> 0$ for all values of the coefficients, and the phase mode undergoes a backward Hopf-bifurcation. Solving the coefficient Γ numerically over a wide range of parameter values always yielded a positive real part. This analysis does not indicate whether or not the instability saturates at higher order or if the phase becomes undefined, signaling a phase slip. To investigate the nonlinear behavior of the phase, (2.7, 2.8) were integrated numerically using a linearized Crank-Nicholson scheme. It was found for the parameter values tested, that the waves outside the stability band underwent a phase slip when perturbed, relaxing to the plane-wave- stable band as seen in Figure 2.4, which shows a space-time diagram of the magnitude $|A|$ of the waves.

2.4 Amplitude Instability: Modulated Waves

We now investigate the instability corresponding to the eigenvalue of the C-field passing through zero in (2.21), which occurs only for $\beta > 0$. Figure 2.5(a) indicates that plane waves are stable at onset, becoming linearly unstable as the control parameter is increased until , for large enough values of the control parameter, they once again regain stability. In addition, the band of stable wavenumbers is bounded by the Eckhaus curve outside the range of the amplitude instability. Thus for $\beta > 0$ two distinct instabilities are possible, depending on the wavenumber of the waves and the distance from threshold. Figure 2.5(b) shows the relevant eigenvalue as a function of the modulation wavenumber for increasing values of the control parameter. The wavenumber of the fastest growing mode increases continuously over the range of values of the control parameter for which the waves are linearly unstable.

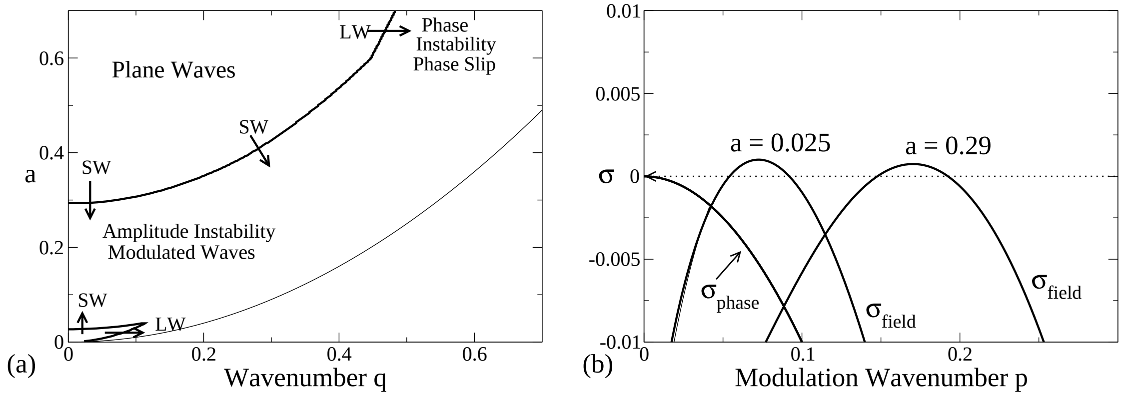

Figure 2.5: A linear stability diagram is given in (a) for h=1, s=1, α=0.02, δ=1.5. LW and SW denote longwave and shortwave instabilities respectively. In (b) the largest positive eigenvalue of the system is plotted versus the modulation wavenumber at bandcenter. Shortwave instabilities occur as the control parameter a is increased from the stable region near onset of the plane waves and as a is decreased from the stable region far beyond threshold.

At bandcenter, the system (2.9, 2.10, 2.11) decouples in the case of unperturbed plane waves. Perturbing the plane-wave solution with the ansatz (2.12, 2.13, 2.14) where $q = 0$, introduces a quadratic coupling of the phase to the real amplitude through $(\partial_x \theta)^2$, which does not appear in the linearized system. Thus it is sufficient to consider the following equations for the linear stability of the waves at bandcenter,

$$\partial_t R = \partial_x^2 R + R[(a + C) - R^2], \tag{2.50}$$

$$\partial_t C = \delta \partial_x^2 C - \alpha C + s \partial_x C + 2hR\partial_x R. \tag{2.51}$$

Linearizing about the plane-wave solution in the above equations yields, for spatially periodic modulations, a complex, quadratic polynomial in the growth rate σ. As in section 3, setting $\sigma_r = 0$ gives a value for the Hopf-frequency,

$$\omega_{Hopf} = p\frac{(2a(s+h)+sp^2)}{((2a+\alpha)+(1+\delta)p^2)}, \tag{2.52}$$

and a polynomial in p, the roots of which give the values of the critical modulation wavenumber,

$$\begin{aligned} -p^2(2a(s+h)+sp^2)^2 + sp^2(2a(s+h)+sp^2)((2a+\alpha)+(1+\delta)p^2) \\ +(p^2+2a)(\delta p^2+\alpha)((2a+\alpha)+(1+\delta)p^2)^2 = 0. \end{aligned} \tag{2.53}$$

For given values of the parameters, (2.53) must be solved for the critical modulation wavenumber p_{cr} implicitly. Requiring additionally that $\frac{\partial\sigma_r}{\partial p} = 0$ allows us to determine the value of the control parameter a for which the eigenvalue first passes through zero as p is varied. We denote this value as $\hat{a_o}$.

If we are to solve (2.9),(2.10),(2.11) to higher order, we must consider the coupling of the phase to the amplitude. We take an expansion of the form,

$$\begin{pmatrix} R \\ \theta \\ C \end{pmatrix} = \begin{pmatrix} \sqrt{\hat{a_0}} \\ 0 \\ 0 \end{pmatrix} + \hat{\epsilon}\begin{pmatrix} R_0 \\ \theta_0 \\ C_0 \end{pmatrix} + \hat{\epsilon}^2\begin{pmatrix} R_1 \\ \theta_1 \\ C_1 \end{pmatrix} + \dots \tag{2.54}$$

Substituting this into (2.10) yields the following series of equations for the phase,

$$\begin{aligned}\partial_t\theta_0 &= \partial_x^2\theta_0, && (2.55)\\ \partial_t\theta_k &= \partial_x^2\theta_k + \partial_x\left(\sum_{n=1}^{k-1}\frac{1}{n!}\frac{\partial^n(R^2)}{\partial\epsilon^n}(\epsilon=0)\epsilon^n\right)\partial_x\theta_j, && (2.56)\end{aligned}$$

where $n + j = k$ and $k > 0$. Thus to leading order the phase satisfies the constant coefficient diffusion equation. Higher orders include a forcing term proportional to the gradient of all lower order terms, which must all decay to zero for long times due to (2.55). We conclude that the long-term behavior of small-amplitude instabilities at bandcenter will not be affected by the phase and consider (2.50, 2.51) the relevant dynamics.

Weakly Nonlinear Analysis

In order to capture the dynamics of the instability near onset at both extremes of the unstable band in the control parameter, we carry out a weakly nonlinear analysis. Since solving the polynomial (2.53) for the critical modulation wavenumber is intractable we leave p as an implicit variable.

We again introduce a slow time scale $\tau = \hat{\epsilon}^2 t$ and define the distance from onset $\hat{\epsilon} = \sqrt{\frac{(a-\hat{a_0})}{\hat{a_2}}}$. We consider a small-amplitude expansion,

$$\begin{pmatrix} R \\ C \end{pmatrix} = \begin{pmatrix} \sqrt{\hat{a_0}} \\ 0 \end{pmatrix} + \hat{\epsilon}\left[\begin{pmatrix} R_0 \\ C_0 \end{pmatrix} A_0(\tau)e^{i(p_{cr}x+\omega_{cr}t)} + c.c + h.o.t.\right],$$

and systematically arrive at a solvability condition at order $\mathrm{O}(\epsilon^3)$ which yields a

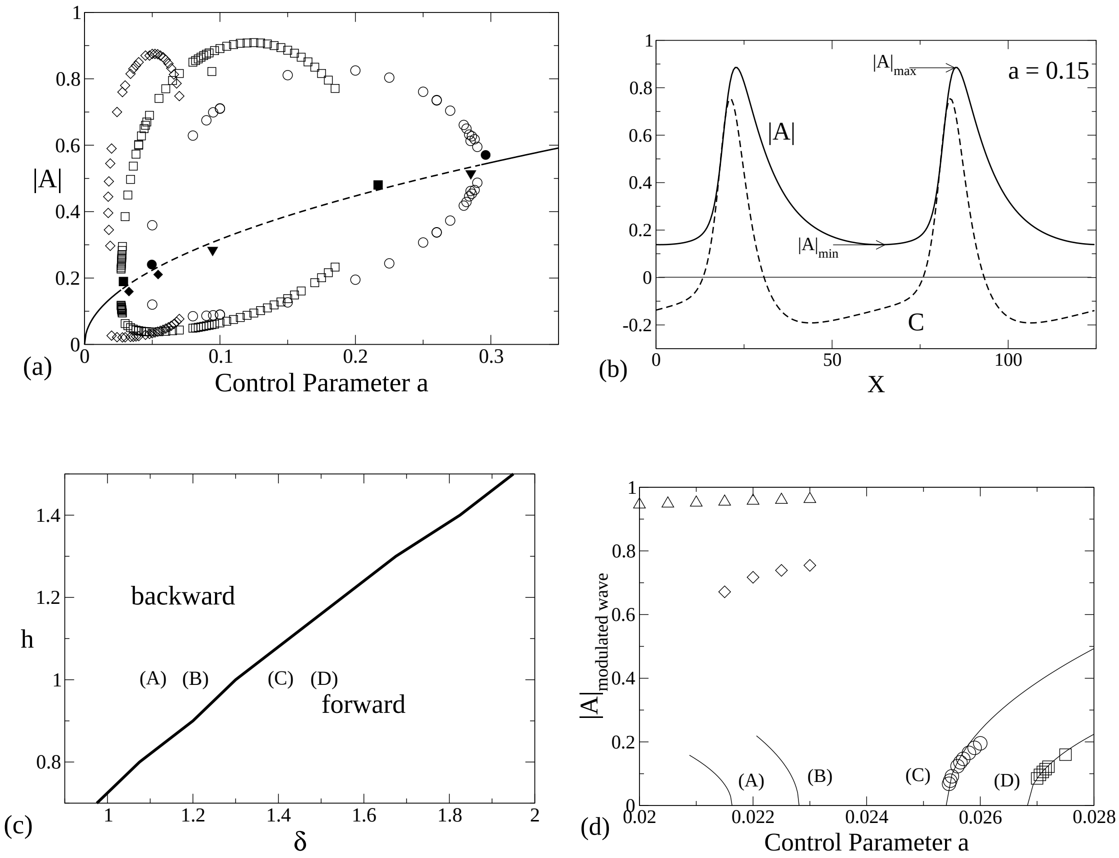

Figure 2.6: (a) Bifurcation diagram of modulated waves. Diamonds indicate minima and maxima of a single-wavelength modulation, squares and circles two and three wavelengths respectively. Solid symbols indicate the point at which the corresponding mode linearly destabilizes the traveling wave (triangles indicate four-wavelength instability although solution branches are not shown). Parameter values are s=1, h=1, δ=1.5, α=0.02 with a system size L=125. (b) Solution with 2-wavelength modulation. (c) Switch of the bifurcation from backward to forward according to (2.57). (d) Comparison of the results from the amplitude equation (solid lines) to numerical simulations confirms this transition. Enough data points where taken for (A),(B) to indicate the presence of bistability and thus confirm the subcritical nature of the bifurcations. s=1, h=1, α=0.02, and δ=1.1 (triangles),1.2 (diamonds),1.4 (circles),1.5 (squares) with a system size L=62.5.

differential equation for A_0,

$$\partial_\tau A_0 = \Lambda(\hat{a_0}, \alpha, \delta, h, s; p(\hat{a_0}, ..))\hat{a_2} A_0 + \Pi(\hat{a_0}, \alpha, \delta, h, s; p(\hat{a_0}, ..))|A_0|^2 A_0. \qquad (2.57)$$

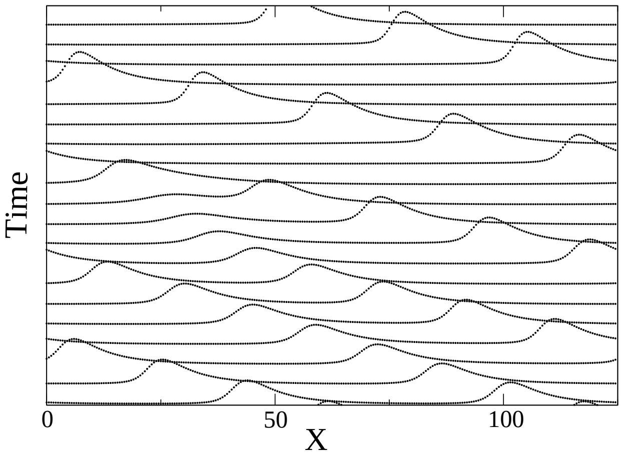

Figure 2.7: Space-time diagram of $|A|$ showing the annihilation of one 'hump' by another leading to the formation of a single-wavelength modulated pattern from a two-wavelength pattern. s=1, h=1, α=0.02, δ=1.5, a=0.04

The coefficients Λ and Π in (2.57) must be solved numerically by determining the value of p from (2.53) for given values of the parameters. For the values of the parameters tested, it was found that the secondary bifurcation encountered first as the control parameter a is increased from 0 can be either forward or backward (cf. stability island including a=0 in Fig. 2.5(a)). The bifurcation which occurs as a is decreased from the region of stability of the plane waves was, in all cases, supercritical. A bifurcation diagram for the modulated waves is given in Figure 2.6(a) for a system size of L=125. The particular structure of the cascade of bifurcations is a consequence of the finite system size, where each branch corresponds to a discrete number of wavelengths of the modulation. The bifurcation to modulated waves near onset of the traveling waves (for small a) is examined in detail in Figures 2.6(c),(d) where the amplitude equation is compared to numerical simulation. As δ is decreased for fixed values of the other parameters, the bifurcation switches from forward to backward.

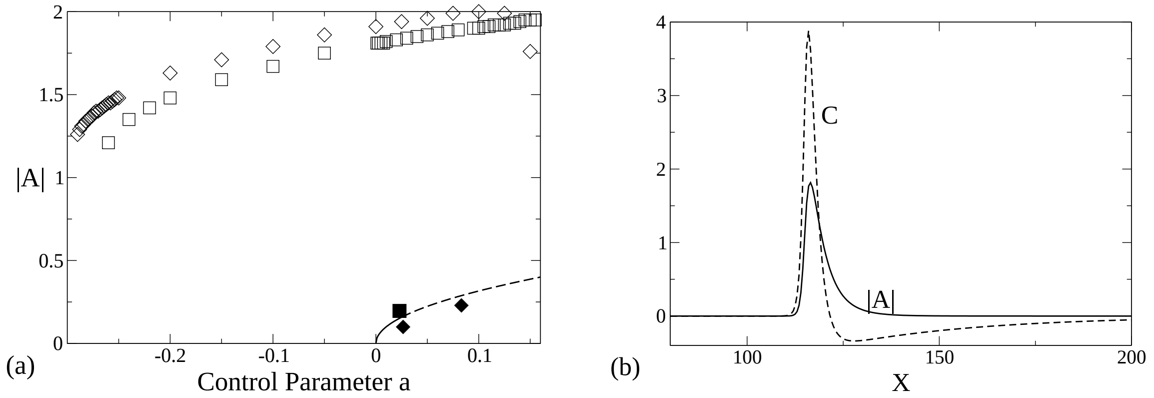

Figure 2.8: (a) Bifurcation diagram of pulses; the subcritical branch extends over the conductive state. The solid symbols indicate where the modes of the corresponding branches become linearly unstable. (b) Profile of the pulse solution with h=1, s=1, $\alpha = 0.02$, $\delta = 0.5$, a=-0.1. The solid line is the amplitude $|A|$ and the dashed line the C-field profile.

Figure 2.6(d) confirms the validity of the amplitude equation.

The dynamics of the modulated wave pattern is not trivial. The destruction or creation of a modulation wavelength during the transient dynamics before the stable pattern is achieved occurs due to particle-like interactions of the 'humps' of the modulations as seen in Figure 2.7. The bifurcation diagram in Figure 2.6(a) indicates the existence of multiple branches for a single value of the control parameter. If the initial bifurcation is to a lower branch (say with 3 wavelengths), two of the three 'humps' will collide after an initial periodically modulated state. The remaining two may again collide to form a single-wavelength modulation which is then stable.

As δ is decreased further, the subcritical branch of modulated waves, created in a saddle-node bifurcation as the control parameter is increased, extends further towards the onset of the traveling waves, eventually becoming bistable with the basic, conductive state (Fig. 2.8(a)). As in the supercritical case, the modulated-wave branches arise from an instability of the plane-waves to finite wavenumber modulations. Modulation wavenumbers p which lie in the interval $p_l < p < p_u$, where the bounds depend on the value of the control parameter a, will linearly destabilize the plane-waves. For a finite system of length L, there will exist modulated-wave branches for all n such that $p = \frac{2n\pi}{L}$ lies in this interval. As n is decreased, the solutions increasingly take on the characteristics of localized objects (Fig. 2.8(b)). In fact, the distance between them can become arbitrarily large. Consequently, this distance can be much larger than the maximal wavelength $\frac{2\pi}{p_l}$ of modulations that linearly destabilize the traveling waves in a given system. Thus, these solutions do not bifurcate directly from the plane-wave branch but rather most likely arise in a tertiary bifurcation off a modulated-wave solution. For example, Figure 2.9 shows a series of modulated-wave branches for a system (L=250) where a single modulation ($n = 1$) does not linearly destabilize the waves. Still, the single-pulse solution exists (dash-dot branch).

2.5 Conclusion

Systems similar to (2.7),(2.8) have been derived in various contexts, including a model of traveling interfacial waves in two-layer Couette flow [8], where $\alpha = 0$ due to conservation of the additional zero-mode, given by the position of the interface. This system was shown to exhibit a phase-instability leading to a phase-slip [7] in agreement with experiment [1]. A small-amplitude model for traveling waves in thermal, binary-mixture convection consists of complex Ginzburg-Landau equations for counterpropagating waves coupled to a slowly decaying mode representing large-scale variations of the concentration field [4]. In this system, the traveling waves arise in a backward

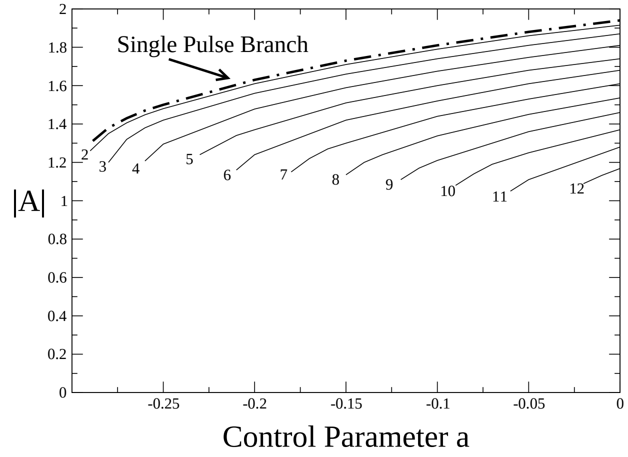

Figure 2.9: Bifurcation Diagram with h=1.0, s=1.0, α=0.02, δ=0.5, q=0 and L=250. Each branch represents a modulated-wave solution with the number of modulations given. As this number n decreases, the modulated-waves become more like localized traveling pulses.

bifurcation. Localized pulse solutions arising from instabilities of this system were identified and many of their properties characterized [17].

In this chapter we have shown that the advected mode can cause the phase-instability to occur at finite wavelength and can introduce an additional amplitude-instability. The latter is identified as the origin of pulse-solutions seen in earlier works. They arise when the secondary bifurcation to modulated waves is sufficiently subcritical to lead to bistability between the modulated wave and the basic state. A similar bifurcation may explain the appearance of localized “worms” in electroconvection in nematic liquid crystals, seen again before the primary instability to supercritical traveling waves. Indeed, a model of traveling waves coupled to a slowly decaying field has been invoked to describe the worm dynamics, attaining qualitative agreement [14].

Finally, it would be worthwhile to consider the effect of dispersion in (2.7) on the dynamics discussed in this chapter. In some cases dispersion has been shown to have a significant effect on the linear-stability properties of waves coupled to a additional mode. A model similar to (2.7, 2.8) used by Bartelet and Charru [1], with $\alpha = 0$ and added dispersion, seems to explain qualitatively the linear-stability properties of waves observed in experiment. The inclusion of dispersion also allows for a determination of the effect of the additional mode on the Benjamin-Feir instability. In some cases this effect is important as, for example, in the 4-species Oregonator model [5] of the BZ reaction where the Benjamin- Feir instability can be preceded by a finite-wavenumber instability.

Chapter 3

Modulated Rotating Convection

3.1 Overview of Rotating Convection

Pattern formation in thermal convection of a rotating fluid layer has been the subject of much experimental and theoretical work in recent years. The effect of the Coriolis force on the dynamics of thermal instabilities makes this system relevant for both astrophysical and geophysical fluid dynamics, while the appearance of spatio-temporally chaotic dynamics near onset make it an attractive candidate for detailed analytical and numerical investigations of the origin and behavior of chaotic complex patterns.

Küppers and Lortz [19] determined that for rotation rates Ω greater than a critical value Ω_{cr}, steady convective roll patterns are unstable to another set of rolls oriented at an angle β relative to the first. These results were confirmed and extended by Clever and Busse [20], who also determined the dependence of Ω_{cr} and β on the Prandtl number of the fluid. In an infinite system, these dynamics are persistent due to isotropy. Busse and Heikes [21] used this fact, and the closeness of β to $\frac{\pi}{3}$, to derive three coupled amplitude equations, in which rolls switch cyclicly as they approach a heteroclinic orbit. In real systems, small amplitude noise perturbs this orbit, leading to nearly periodic switching of rolls. In sufficiently large systems the switching becomes incoherent in space and causes the development of patches of rolls with different orientations. The ensuing dynamics are chaotic [22, 23].

In recent experiments on rotating convection [24], Thompson, Bajaj and Ahlers investigated the effect of a temporal modulation of the rotation rate on the Küppers-Lortz (KL) state. They find that for sufficiently large modulation concentric roll patterns (targets) as well as multi-armed spirals can be stabilized and replace the chaotic KL state. Focusing on the target pattern, they find that the rolls in these patterns drift radially inward and they measure the dependence of the drift velocity on modulation amplitude and frequency, mean rotation rate, and heating. They point out that the modulation sets up an oscillatory azimuthal mean flow, which tends to align rolls along that direction. Since the alignment singles out a specific orientation, it breaks the isotropy of the system. Motivated by these findings we therefore investigate here the effect of anisotropy on roll patterns in systems exhibiting KL chaos.

Within the framework of a suitably extended Swift-Hohenberg-model (SH) we first study the stability of straight rolls in systems with broken chiral symmetry (modeling the Coriolis force due to rotation) and with weak anisotropy. We then use these analytical results to interpret simulation of this SH-model in a cylindrical geometry in which we obtain target and spiral patterns as seen in experiment.

3.2 The stability of rolls with anisotropy

We study the effect of weak anisotropy on the Küppers-Lortz state in the following modified Swift-Hohenberg model,

$$\partial_t \psi = \mu\psi + \alpha^2(\hat{n}\cdot\nabla)^2\psi - (\nabla^2+1)^2\psi - \psi^3 + \gamma\hat{k}\cdot[\nabla\times[(\nabla\psi)^2\nabla\psi]], \tag{3.1}$$

where $\hat{n}$ is a director indicating the preferred orientation, and α gives the strength of this anisotropy. We retain the up-down (Boussinesq) symmetry ($\psi \to -\psi$) by including only odd terms in ψ, and include a nonlinear gradient term that breaks the chiral symmetry. The rotation rate is therefore measured by γ. Similar models have been systematically derived from the fluid equations, with [25] and without [26, 27] mean flow effects, and have enjoyed widespread use, e.g. [28, 29, 30, 31]. We mean (3.1) to be a model equation and are concerned with the *qualitative* effect of anisotropy on the Küppers-Lortz instability.

Focusing on the weakly nonlinear regime and assuming the anisotropy to be weak, we take $\mu = \epsilon^2\mu_2$ and $\alpha = \epsilon\alpha_2$ with $\epsilon \ll 1$. To leading order in ϵ the system is therefore isotropic. To study the effect of the anisotropy on the KL-instability we consider the weakly nonlinear competition of two sets of rolls with relative angle β with the ansatz,

$$\psi = \epsilon(A(\tau)e^{i(\cos(\theta)x+\sin(\theta)y)} + B(\tau)e^{i(\cos(\theta+\beta)x+\sin(\theta+\beta)y)} + c.c.) + h.o.t. \tag{3.2}$$

Thus here we do not analyze all side-band instabilities. To leading order the system is isotropic and θ is a free parameter. The complex amplitudes A and B evolve on the slow timescale $\tau = \epsilon t$. For concreteness we take $\hat{n} = \hat{e}_y$. At order ϵ^3, a solvability condition yields

$$\begin{aligned} \partial_\tau A &= \mu_2 A - \alpha^2 \sin^2(\theta) A - 3|A|^2 A - (6 + 4\gamma \sin\beta\cos\beta)|B|^2 A, && (3.3) \\ \partial_\tau B &= \mu_2 B - \alpha^2 \sin^2(\theta + \beta) B - 3|B|^2 B - (6 - 4\gamma \sin\beta\cos\beta)|A|^2 B. && (3.4) \end{aligned}$$

We examine the stability of rolls of orientation θ with respect to a set of rolls oriented β to the first set of rolls. With $\alpha = 0$ (isotropic case), the absolute orientation of the rolls θ is irrelevant, and we find they become first unstable to rolls with orientation

$$\beta_{KL} = 45^o \tag{3.5}$$

for

$$\gamma \geq \gamma_{KL} = \frac{3}{2}. \tag{3.6}$$

Introducing $\alpha \neq 0$ leads to a dependence of both β_{KL} and γ_{KL} on the absolute orientation of the rolls θ. The growth rates of the perturbations are given by

$$\begin{aligned} \sigma_A &= -2(\mu_2 - \alpha^2 \sin^2\theta), && (3.7) \\ \sigma_B &= \mu_2(-1 + \frac{4}{3}\gamma \sin\beta\cos\beta) - \alpha(\sin^2\theta + \beta + [\frac{4}{3}\gamma \sin\beta\cos\beta - 2]\sin^2\theta). && (3.8) \end{aligned}$$

As can be seen from (3.7), the anisotropy has shifted the onset of rolls with orientation θ to

$$\mu_2(\hat{\theta}) = \alpha_2^2 \sin^2\hat{\theta}. \tag{3.9}$$

Thus rolls with orientation θ exist for $\mu_2 > \mu_{2cr}(\theta)$. For fixed μ this implies a neutral curve $\alpha(\theta)$ as shown by the dashed line in Figure 3.1. Rolls of orientation θ first

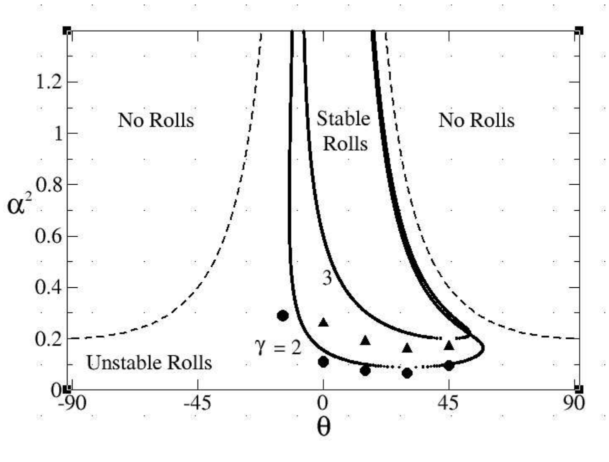

Figure 3.1: Linear stability diagram of rolls with orientation θ in (3.3, 3.4) with respect to rolls at a relative orientation of β_{KL}. Here $\mu = 0.2$. Numerical results are given by the solid symbols: triangles for $\gamma = 3$ and circles for $\gamma = 2$.

become unstable to rolls of different orientation at

$$\sigma_B \quad = \quad \frac{\partial \sigma_B}{\partial \beta} = 0. \tag{3.10}$$

Equation (3.10) is solved here numerically for the linear stability limits although it has been shown in [32] that the stability boundary can be found analytically. Results are given in Figure 3.1 [1] for various values of γ (solid lines). To test these stability results we perform numerical simulations using a pseudospectral code with periodic boundary conditions, employing an integrating factor Runge-Kutta time-stepping method. We perturb straight rolls of orientation θ by small-amplitude rolls of orientation $\theta + \beta$, where β is chosen as the angle corresponding to the maximal growth rate according to (3.10). To verify that no additional instabilities are present,

---

[1] The linear stability curve published in [33] is incorrect as pointed out by the authors in [32]. The corrected stability curves are given in this figure.

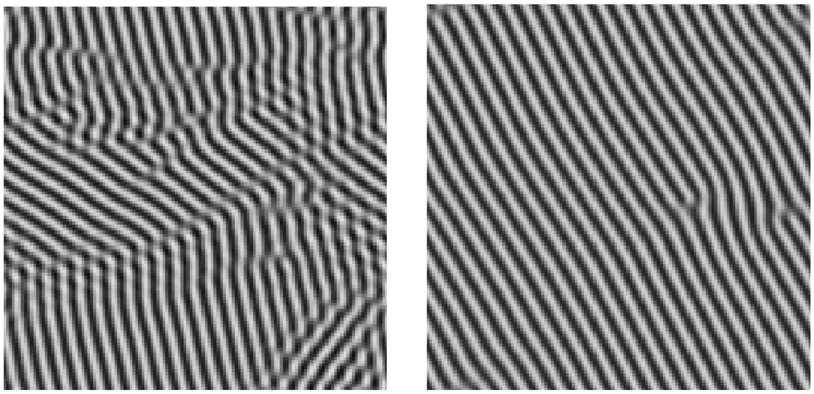

Figure 3.2: Stabilization of rolls in the regime of domain chaos arising from the Küppers-Lortz instability. a) A typical patch-work pattern of domain chaos, where the angle between patches $\beta_{KL} = 45$, and $\gamma = 2.0, \mu = 0.2, \alpha = 0.0$). b) For the same values of the parameters with $\alpha^2 = 0.15$, rolls are stabilized.

we also perturb the rolls with small-amplitude noise. As can be seen from the solid symbols in Figure 3.1, numerical simulations agree well with the weakly nonlinear analysis for rotation rates γ that are not too far above $\gamma_{KL}(\alpha) \sim 1.5$, for which only weak anisotropy is needed for stability. For larger rotations rates γ, the weakly nonlinear theory overestimates the amount of anisotropy α needed to stabilize rolls. For $\alpha = O(1)$, the anisotropy affects the linear growth rate of rolls already in (3.1) and will introduce a significant dependence of the critical wavenumber on the orientation θ. Numerical results for larger α reveal that large amplitude rolls (with $\theta = 0$) tend to grow and invade regions of rolls of other orientations front-wise. In fact, for $\alpha \to \infty$ only rolls with $\theta = 0$ exist.

Thus, weak anisotropy can stabilize periodic rolls arising in rotating convection in the Küppers-Lortz unstable regime. Specifically, there is a finite band of angles θ with respect to the anisotropic director $\hat{n}$ such that rolls with this angle are stable to homogeneous perturbations of all possible orientations.

3.3 Modulated rotating convection: spirals and targets

We now turn to the specific problem of rotating convection with periodically modulated rotation. A thin layer of fluid of height d is heated from below and bounded above and below by a rigid plate, which is rotated with an angular velocity $\Omega = \Omega_o(1 + \delta \cos \omega t)$. For $\delta = 0$ we recover the well-studied case of rotating convection [19]-[25], [28, 29, 34]. For $\delta \ll 1$ but nonzero, a nontrivial base flow is induced by the periodic motion of the rigid plates. This flow advects perturbations leading to thermal instabilities in such a way as to affect their growth rate. Indeed, far from the axis of rotation, the onset of the thermal instability is dependent on the orientation of periodic-roll perturbations with respect to the base flow in a manner analogous to the linear operator in (3.1) as discussed below, (cf. [35]). Closer to the axis of rotation, the curvature of the base flow becomes significant and a straight-roll approximation is not a good one.

The dynamics can be described by the Boussinesq fluid equations in a frame rotating at the mean angular velocity Ω_0 [19]-[23]. Due to the temporal modulation of the angular velocity, the rigid boundary conditions at top and bottom imply that the azimuthal velocity component oscillates in time with the plates,

$$u_\theta = \Re(\delta \Omega_0 r e^{i\omega t}). \tag{3.11}$$

This condition induces an azimuthal shear flow, the strength of which grows with distance from the axis of rotation. If we assume the flow is restricted to a finite

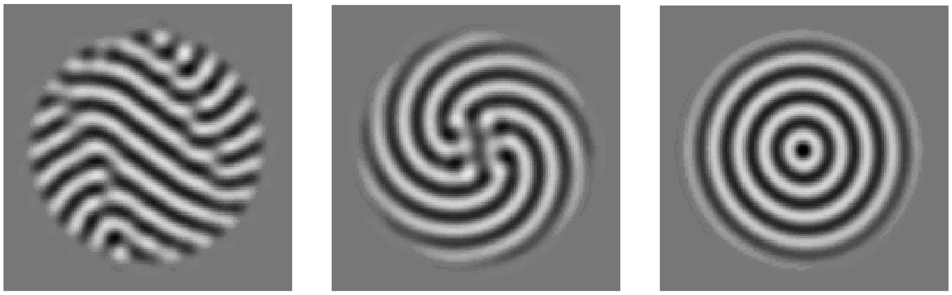

Figure 3.3: Representative patterns: a) KL-state with $\delta = 0.0$ b) 6-armed spiral for $\delta = 0.0005$ Equation (3.15) predicts six arms in this case. c) Target pattern for $\delta = 0.001$. For all three $\gamma = 2.0$, $\mu = 0.2$ and the system size $L = 72$.

geometry, Coriolis forces acting on this flow can be balanced by the radial pressure gradient as with the centrifugal force.

Far from the axis of rotation the non-dimensionalized flow takes the form,

$$\hat{u}_\theta = \delta \ \mathrm{Pr} \ \tau \, r Re\left(\frac{\sinh kz - \sinh k(z-1)}{2\sinh k} e^{iPr\,\omega t}\right), \tag{3.12}$$

where the plates are located at $z = 0, 1$, $k = \sqrt{\frac{\omega}{2}}(1+i)$ and

$$\hat{u}_\theta = u_\theta \frac{d}{\kappa}, \quad Pr = \frac{\nu}{\kappa}, \quad \tau = \frac{2\Omega_0 d^2}{\nu}, \tag{3.13}$$

where the modulation frequency ω has been nondimensionalized with respect to the viscous diffusion time. Note that (3.12) satisfies the continuity equation, $\nabla \cdot \mathbf{u} = 0$.

Thermal instabilities arising from the imposed temperature gradient are advected by (3.12) and hence parametrically forced with frequency $Pr\,\omega$. To model the change in their growth rates within the SH equation (3.1), we consider the region away from the center of rotation where curvature effects can be neglected. There, to a good approximation, the analysis of section II should apply locally with the anisotropy director $\hat{n}$ being given by the local orientation of the oscillating base flow, $\hat{n} = \hat{e}_\theta$. This is based on the observation that near onset the dynamics of the instability is slow compared with the period of the oscillating shear-flow for any finite rotation rate, which allows an averaging over the oscillations. Since the forcing is invariant under the transformation $\delta \to -\delta$, $t \to t + \frac{\pi}{Pr\,\omega}$, the base flow affects the growth-rate of thermal instabilities through mean-squared contributions (proportional to δ^2). Based on (3.12) we therefore choose

$$\alpha^2 = \delta^2 r^2, \qquad \hat{n} = \hat{e}_\theta. \tag{3.14}$$

We note that the scaling of the anisotropy (3.14) as linear in the distance from the axis of rotation is only correct far from the axis itself. However, we retain this simplified form and hope to extract qualitatively correct results. In fact, simulations with other polynomial dependencies have revealed that only the monotonicity of the function is important in determining qualitative features of the patterns.

To model the circular container of the experiments we use a circular ramp in the control parameter μ, maintaining the region surrounding the circle at a sub-critical value, thereby suppressing the convection amplitude. In full Navier-Stokes simulations this procedure has been used successfully in comparison with experiment (Pesch/Ahlers/Schatz). Simulations reveal a wide variety of spiral patterns as well as targets. For small δ, where we expect the weakly-nonlinear theory for periodic rolls to be valid sufficiently far from the core of the spiral, we are able to predict the number of spiral-arms with reasonable accuracy. Such an analysis can be understood from Figure 3.1. For a fixed 'rotation-rate' γ, the strength of anisotropy α increases with distance from the core of the spiral. There is thus a region in the vicinity of the core where no rolls are stable, and rolls of a given orientation θ^* are selected at a distance r^* as determined by condition (3.10). The projection of the local wavevector of the spiral onto the perimeter of the critical circle with radius r^* is given by $q \sin \theta^*$. The number of arms of the spiral is then given by the circumference ($2\pi r^*$) divided by the wavelength associated with the projected wavevector,

$$N = r^* q \sin \theta^*. \tag{3.15}$$

Spirals or targets can be generated for the same parameter values given different initial conditions. In general, an initial straight roll pattern will result in a target for sufficiently large δ, whereas disordered initial conditions generically yield spirals, even for strong anisotropy.

Interestingly, the orientation-selection mechanism given by (3.15) predicts the possibility of a large region surrounding the core, within which no rolls are stable in the context of the weakly nonlinear theory. If the anisotropy is sufficiently weak, one should see a disordered region of domain chaos, bounded by a stable spiral, given a large enough system. Such a pattern is shown in Figure 3.4.

3.4 Conclusion

Spirals and targets arising in Rayleigh-Bénard convection have been the subject of much theory and experimental work, [25, 22, 29, 36, 37, 38]. Target patterns in low-

Prandtl number convection are a consequence of horizontal, thermal gradients at the sidewalls of a cylindrical container, which tend to align rolls parallel to the walls [38]. Even with sidewall forcing, the targets become unstable to straight rolls relatively close to threshold. In rotating convection, the target patterns arising from such sidewall forcing undergo a mean drift [29] due to the breaking of reflection symmetry by the applied rotation. However, in the case of rotating convection with a modulated rotation rate, the chiral patterns are not a consequence of the system geometry, but rather are induced by an isotropy-breaking shear flow, which acts azimuthally. We have shown that these patterns are stable in regimes where one would see spatio-temporal chaos in the absence of modulation. Our analysis indicates that the shear flow acts to stabilize rolls within a band of stable orientations w.r.t. the azimuthal flow itself. This leads naturally to a chiral pattern.

The qualitative agreement between the types of patterns observed in experiment [24] and those studied here make the selection mechanism described in section III plausible. Spirals and targets arise through the interaction of the destabilizing process responsible for the KL instability and the stabilizing effect of the azimuthal mean flow (MF). Quantitative comparison of the dependence of the pattern behavior on the reduced Rayleigh number, rotation rate, and amplitude and frequency of the modulation with experiment is, however, not possible within the framework of (3.1). However, the qualitative genericity of the appearance of spirals patterns under modulated rotation with disordered initial conditions (KL state) seems to hold both under experimental conditions and here. Targets, on the other hand, must be generated with care but then persist as stable patterns over a wide range of parameter values.

The target patterns observed in [24] travel inwards radially, collapsing periodically

Figure 3.4: A stable spiral with a chaotic core. The system size is $L = 144$ with $\gamma = 2.0$, $\mu = 0.2$ and $\delta^2 = 0.0001$. Note that equation (3.15) predicts 14 arms. The core dynamics occur on a fast timescale w.r.t. the slow, solid-body rotation of the outer spiral.

at the center. The origin of this drift has not been identified yet. One possibility is that the time-periodic component of the Coriolis force acting on the time-periodic azimuthal flow generates a radial flow with a steady component, which would advect the axisymmetric roll pattern [39, 40]. Another possibility is that the drift is due to a mismatch between the wavenumber selected by the umbilicus [41] and that selected by the container side-wall [42, 43]. The competing selected wavenumbers set up a wavenumber gradient that induces a drift of the pattern [44, 45]. It should be possible to distinguish between these two mechanisms by comparing the dynamics in systems of different aspect ratio. For larger systems, the wavenumber gradient induced by the incompatibility of the selected wavenumbers would be weakened, while the effective strength of the radial flow would naturally be stronger due to the greater Coriolis force at larger radii. Experiments in such larger systems would also be of interest in view of the prediction that in such systems the core of the spirals would exhibit chaotic dynamics of the Küppers-Lortz type.

In our simulations of (3.1) no radial drift of the concentric rolls was found. This is not unexpected, since in the absence of the chiral-symmetry breaking term proportional to γ eq.(3.1) is variational and persistent dynamics are ruled out. To obtain drift the variational character of the system has to be broken to a sufficient degree. This may require much larger rotation rates γ or the introduction of additional non-variational terms. We have not pursued this further since simulations of extensions of (3.1) with possibly also modified boundary conditions would not allow any quantitative comparison with experiments and would therefore be of limited use in identifying the dominant mechanism responsible for the drift.

Chapter 4

Slip at a Liquid-Solid Interface

4.1 Evidence of slip

In the modeling of the flow of fluids past a solid interface one assumes that, at the interface, the component of the fluid velocity tangential to the solid matches the velocity of the solid itself. This is the *no slip* condition, and it successfully describes the behavior of simple fluids at the macroscopic scale.

Increasingly, however, both experiments [46, 47, 48, 49, 50] and molecular dynamics (MD) simulations [51, 52, 53, 54] indicate that slip does occur at the microscopic scale. Pit, Hervet and Léger [46] measured the slip of hexadecane over sapphire and concluded that molecular-scale roughness of the solid surface inhibited slip although slip lengths up to 400nm were found. Zhu and Granick [47] investigated the flow of Newtonian fluids over molecularly smooth surfaces and found that there is a critical flow rate above which slip occurred. The degree of slip was furthermore correlated with the wettability of the interface. Craig, Neto and Williams [48] found that the slip of aqueous solutions of sucrose on mica depended both on the viscosity of the fluid and the shear rate at the interface. Bonnacurso, Kappl and Butt [49] found slip for water on hydrophilic surfaces with a slip length of 8-9nm, while Bonaccurso, Butt and Craig [50] found that large-scale roughness of a completely wetting surface can actually *increase* slip.

Thomson and Robbins [51] showed in MD simluations that the amount of slip was correlated with the degree of ordering of the fluid particles at the solid interface. The investigation of the effect of various densities and interfacial energies in simulations by Thompson and Troian [52] revealed a universal relationship between the shear rate at the interface and the slip length. Cieplak, Koplik and Banavar [54] concluded that the ordering of the fluid near the interface was the determining factor in predicting slip.

Most of the available data support the notion that slip will be understood only by considering the molecular interaction between the fluid and the solid at the interface. The organization of the initial fluid layer seems crucial to the question of slip and it has been hypothesized that the mechanical properties of this layer are truly different from the bulk properties of the fluid [49], i.e. a new phase.

The present study approaches the question of slip at a fluid-solid interface from a dynamical-systems' perspective. We propose the use of a well-known equation from solid-state physics, the Frenkel-Kontorova (FK) equation, as a model of coherent motion in the initial fluid layer at the interface. Parameters in the FK equation can be meaningfully related to properties of the fluid and solid. A close look at slip dynamics in MD simulations will then motivate some modification of the FK model, the dynamics of which agrees remarkably well with the MD. The modified FK model indeed describes the dynamics of a phase which is solid-like on short time scales, but diffusive (fluid-like) on longer time scales.

4.2 The Frenkel-Kontorova Equation

We consider a chain of coupled molecules with an equilibrium interparticle spacing of a. The chain sits a fixed distance d from the solid and is subject to a periodic potential with spatial period λ. Particle i has an energy given by the Hamiltonian

$$H = \sum_i \Big\{ \frac{m}{2}\left(\frac{dx_i}{dt}\right)^2 + h\big[1 - \cos\big(\frac{2\pi x_i}{\lambda}\big)\big] + \frac{k}{2}(x_{i+1} - x_i - a)^2 \Big\}. \tag{4.1}$$

From the Hamiltonian follows the equation of motion for the i^{th} particle

$$m\ddot{x}_i = -\frac{2\pi h}{\lambda}\sin\big(\frac{2\pi x_i}{\lambda}\big) + k(x_{i+1} - 2x_i + x_{i-1}) + \eta_{ff}(V - \dot{x}_i) - \eta_{fs}\dot{x}_i \tag{4.2}$$

where local dissipation of energy is modeled heuristically via a momentum transfer between liquid particles, proportional to the horizontal component of the velocity difference $V - \dot{x}_i$ and a liquid to solid energy loss, here taken to be proportional to the liquid particle velocity. The quantity V is thus taken to be a measure of the mean velocity of the liquid particles just above the initial layer near the interface.

It is instructive to consider the limit of large shear rate for which the last two terms in 4.2 will balance, yielding

$$\dot{x}_i = \frac{\eta_{ff} V}{\eta_{ff} + \eta_{fs}}. \tag{4.3}$$

Equation 4.3 is valid for all i, indicating that the slip velocity of the liquid particles adjacent to the substrate is simply proportional to the mean horizontal component of the velocity of those liquid particles near the wall in the bulk. The *slip length*, which is defined as the fictional distance below the interface at which the liquid velocity would equal zero if extrapolated linearly, is defined as the the slip velocity divided by the shear rate $L_s = \frac{v_{slip}}{V - v_{slip}} d$. For large shear rates in 4.2 this is just

$$L_s = \frac{\eta_{ff}}{\eta_{fs}} d. \tag{4.4}$$

In general, the shear stress at the interface can be written $\sigma_{fs} = f_{\text{eff}} v_{slip}$ where f_{eff} is the effective friction between the liquid and solid [46]. The slip length $L_s = \frac{v_{slip}}{\dot{\gamma}}$ where $\dot{\gamma}$ is the shear rate, which itself can be written $\dot{\gamma} = \frac{\sigma_{fs}}{\eta_{\text{bulk}}}$, where η_{bulk} is the bulk viscosity of the liquid. Finally this yields

$$L_s = \frac{\eta_{\text{bulk}}}{f_{\text{eff}}} \tag{4.5}$$

Thus, comparison of 4.4 and 4.5 reveals that at least for large shear rates the modified FK model yields a consistent and accurate estimate of the slip length. Furthermore the parameters η_{ff} and $\frac{\eta_{fs}}{d}$ can be considered the bulk visocity of the liquid and the effective liquid-solid friction respectively. Note, as mentioned earlier, that slip increases with increasing liquid viscosity and shear-rate at the interface in experiment, effects which are trivially captured in 4.2 as the forcing is just $\eta_{ff}(V - \dot{x}_i)$.

We consider two possible non-dimensionalizations of 4.2, which differ in the definition of the relevant time scale. In the first case we normalize time by the frequency of oscillation of a liquid particle trapped in a local minimum of the substrate potential. This yields

$$\ddot{x}_i = -\sin(x_i) + \tilde{k}\triangle^\dagger\triangle x_i + \tilde{\eta}_{ff}(V - \dot{x}_i) - \tilde{\eta}_{fs}\dot{x}_i \tag{4.6}$$

where the length and time scales are $\frac{\lambda}{2\pi}$ and $\frac{\lambda}{2\pi}\sqrt{\frac{m}{h}}$, the nondimensional position x has been written without overbar, and the discrete diffusion operator $\triangle^\dagger\triangle$ has been introduced. The non-dimensional liquid-liquid coupling strength and frictional parameters are

$$\tilde{k} = \frac{\lambda^2}{4\pi^2 h}k, \tag{4.7}$$

$$\tilde{\eta}_{ij} = \frac{\lambda}{2\pi\sqrt{mh}}\eta_{ij}. \tag{4.8}$$

In the second case we normalize time by the frequency of oscillation of a liquid particle about its equilibrium, inter-particle spacing, giving

$$\ddot{x}_i = -\tilde{h}\sin(x_i) + \triangle^\dagger\triangle x_i + \tilde{\eta}_{ff}(V - \dot{x}_i) - \tilde{\eta}_{fs}\dot{x}_i \tag{4.9}$$

where the length and time scales are $\frac{\lambda}{2\pi}$ and $\sqrt{\frac{m}{k}}$ and the non-dimensional amplitude of the substrate potential and frictional parameters are

$$\tilde{h} = \frac{4\pi^2}{\lambda^2 k}h, \tag{4.10}$$

$$\tilde{\eta}_{ij} = \frac{\eta_{ij}}{\sqrt{mk}}. \tag{4.11}$$

In what follows, the forcing and damping terms in 4.6 and 4.9 will be written f

and $\eta \dot{x}_i$ where

$$\begin{aligned} f &= \tilde{\eta}_{ff} V, \quad (4.12) \\ \eta &= \tilde{\eta}_{ff} + \tilde{\eta}_{fs}. \quad (4.13) \end{aligned}$$

Other non-dimensionalizations are possible, including scaling by a viscous diffusion time , but we will restrict our analysis to 4.6 and 4.9, thereby retaining the damping coefficients explicitly. Worthy of note is the conspicuous absence of the inter-particle spacing a from 4.1. In fact, the value of the non-dimensional parameter $\xi = \frac{a}{\lambda}$ plays a crucial role in determining the dynamical state of the system defined by 4.2. The commensurability parameter ξ measures the relative liquid-liquid to solid-solid inter-particle spacings and strongly influences the degree of slip in the chain, as we shall see.

Equation 4.2 is the forced, damped Frenkel-Kontorova (FK) equation. The FK equation itself, which is obtained by setting η_{ff} and η_{fs} to zero in 4.2, was first introduced in the theory of dislocations in metals [55]. It has been evoked to describe the motion of dislocations in crystals, the propagation of charge-density waves, the theory of Josephson junctions and the molecular basis for solid friction as well as many other important applications in solid-state physics [55, 56]. The universality of the FK model resides in the fact that it is the simplest possible model of a chain of coupled particles subject to a periodic potential.

In the limit that the inter-particle spacing goes to zero in the FK model, the discrete operator can be expanded in the small parameter a. Retaining only the leading order term yields the sine-Gordon (sG) equation

$$m\ddot{u} = -\frac{2\pi h}{\lambda} \sin\big(\frac{2\pi u}{\lambda}\big) + c^2 u'' \tag{4.14}$$

where $c^2 = \frac{ka^2}{2}$ and thus the equation is valid only for $k \to \infty$. The variable $u(x)$ represents a displacement, which depends now continuously on the spatial variable x. The equation 4.14 can be non-dimensionalized with $U = \frac{2\pi}{\lambda}u$, $X = \frac{2\pi}{\lambda}\sqrt{\frac{h}{c^2}}x$ and $T = \frac{2\pi}{\lambda}\sqrt{\frac{h}{m}}t$, to yield

$$\ddot{U} - U'' + \sin U = 0 \tag{4.15}$$

The sG equation, together with other nonlinear equations such as the Korteweg de-Vries (KdV) and nonlinear Schrödinger (NLS) equations is exactly integrable and thus solvable by the inverse scattering method [57, 58]. Solutions of 4.14 include small-amplitude phonon modes (radiation) as well as localized kinks and antikinks in which the phase winds $\pm 2\pi$ respectively. Time-varying kinks called 'breathers' are also solutions of 4.14. The connection between kinks in the integrable sG limit and dislocations or defects in the FK model is well-established [55] although key differences make the two qualitatively distinct. In particular, kink solutions of 4.14 represent Goldstone modes due to the translational invariance of the sG equation. As such no energy is required to drive defects in the continuum approximation. In contrast, the FK equation is invariant only under discrete translations, the physical consequence of which is a pinning force that must be overcome to drive defect motion. Nonetheless, perturbations of the continuum description can prove fruitful in elucidating properties of kinks in discrete lattices.

4.3 Slip dynamics in the FK model

Analysis of the equilibrium states of 4.2 already provides a major theoretical challenge, which has been taken up by many researchers (see [56] for a review). Using the non-dimensional equation 4.6, determination of the equilibrium configuration of particles is equivalent to solving

$$\sin x_i = k(x_{i+1} - 2x_i + x_{i-1}) + f \tag{4.16}$$

where all overbars have been dropped. It should be noted in light of the motivation for this work, that the equilibrium arrangement of liquid molecules at a solid interface is not well understood even for water on a metal surface (e.g. [59]). A quantitative description of these states requires a detailed understanding of the relevant forces, which may well differ considerably depending on the solid and liquid properties. Given these forces, the equilibrium configuration is just the minimal energy state, whose determination in the FK model is equivalent to solving 4.16 [1].

The liquid-liquid equilibrium interparticle spacing a is once again absent in 4.16. It plays an indirect role in defining the average density of particles, e.g. if the system length consists of 100 periods of the underlying substrate then the solution of 4.16 will clearly be different for 100 or 157 particles and is thus depedent on a in this way.

Let us first consider solutions of 4.16 with $f = 0$, which we will refer to as unforced *ground states*. The nature of the ground states depends crucially on the commensurability ξ, also referred to as the average spacing or winding number [56]. Ground states are called *commensurate* for rational values of ξ and are otherwise called *in-*

---

[1] Solutions to the equation 4.16 will, of course, give saddle-point energy states as well.

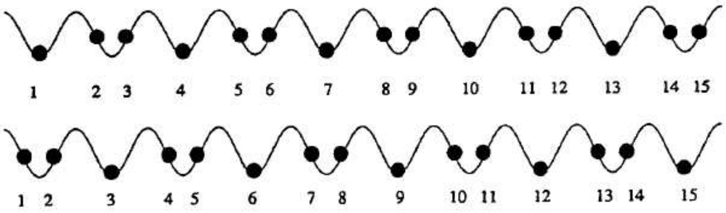

Figure 4.1: Ground state of chain for which $\xi = \frac{2}{3}$. The chain is invariant under the discrete translation of one period of the underlying substrate. Taken from [56].

commensurate. All commensurate ground states are periodic with period Λ such that Λ is the smallest integer for which $\frac{\Lambda}{\xi}$ is also an integer. Figure 4.1 shows a $\xi = \frac{2}{3}$ ground state for which $\Lambda = 2$ ($\frac{\Lambda}{\xi} = 3$). It is worth noting that $\frac{1}{\xi} = \frac{\lambda}{a} = \frac{p}{q}$ where p is the average number of particles over q periods of the substrate. In a one-dimensional system this is proportional to the density of particles. For a fixed system size L with q periods of the substrate of wavelength λ and p particles, the commensurability can be rewritten

$$\xi = \frac{1}{1 + \frac{(p-q)\lambda}{L}} \tag{4.17}$$

where the quantity $\delta = \frac{(p-q)}{q}$ is known as the *mismatch*. The quantity $|\frac{\delta\lambda}{L}|$ is the *density of defects*.

The ground state shown in Figure 4.1 is clearly invariant under discrete translations of one period of the periodic potential. The consequence of this discrete symmetry is the existence of a pinning potential which must be overcome to shift the chain one unit. The pinning potential is related to the adiabatic trajectory connecting the two minima in the energy landscape given by the second two terms of the Hamiltonian 4.1. The adiabatic trajectory refers to the trajectory along which the system relaxes to its new energy state at each point, i.e. momentum may be neglected. If the trajectory passes through a less energetically preferred state, then some work must be done to shift the chain. Commensurate chains always exhibit such a pinning potential known as the Peierls-Nabarro potential E_{PN}. We then see that given a nonzero f, there may or may not exist a solution to 4.16. Namely, for $f > \frac{E_{PN}}{\lambda}$ the chain is unpinned and no static solutions exist.

In contrast to commensurate chains, ground states of incommensurate chains may or may not be pinned. For $k = 0$ all the particles fall into the wells of the periodic substrate regardless of the value of ξ. As the coupling strength increases, Aubry has proven [60] that there is a transition at a critical value $k_{cr}(\xi)$ for which the pinning potential goes to zero. Furthermore he proved that this occurs first for the value of ξ that is "most irrational": $\frac{\sqrt{5}+1}{2}$, the golden mean. The transition to the de-pinned state is related to the emergence of a zero-mode of the linearized operator in 4.16 about the ground state [61], effectively making the system translationally invariant. Thus for some incommensurate systems E_{PN} must still be overcome to unpin the chain, while for others the particles will move freely even for an infinitesimal value of the forcing f. It should be noted that we consider a periodic system in which the most incommensurate chain will still be periodic with period equal to the system size itself.

Once the particles have begun to move along the substrate under the force f we will find it useful to define the *slip velocity*

$$v_{slip} = \lim_{T \to \infty} \frac{1}{T} \int_0^T dt \frac{1}{N} \sum_{i=1}^{N} \dot{x}_i, \tag{4.18}$$

which is merely the long-time average of the ensemble average of particle velocities.

In practice 4.18 is calculated numerically with a finite T taken sufficiently large for convergence.

Technically, characterizing the slip of the liquid particles in the context of 4.2 reduces to the following two problems:

1. Determine the critical value of the forcing $f_{cr}(\xi, k, \eta)$ at which slip first occurs.
2. For $f > f_{cr}$, determine the slip velocity $v_{slip}(\xi, k, \eta, f - f_{cr})$.

We will look in depth at points 1 and 2 for the strongly damped (order 1, not overdamped), driven FK model. This is particularly important since recent studies have revealed quite complex dynamics in the weakly damped, driven FK model (η small) [62, 63, 64, 65]. Strunz and Elmer [62] show that there is a parametric resonance instability of the uniformly sliding chain if the damping is weaker than the amplitude of the substrate potential. In addition, the weak damping leads to bistability between flowing and static states. For weak enough damping, inertia is sufficient to maintain the motion of the chain despite the existence of a stable ground state. This bistability leads naturally to domains and fronts. For very weak damping ($\eta \ll 1$) [63] the dynamics is chaotic. It may be that weakly-damped dynamics is relevant for the motion of liquid particle near a solid interface. One can make an argument for at least order one damping given the relatively high temperature of a liquid. For the sake of simplicity, we will not analyze the weakly damped dynamics in the present study.

The connection between 4.2 and slip at a liquid-solid interface has been motivated heuristically, but results from the FK model should be carefully scrutinized before conclusions about real liquids are drawn. The FK equation is used here as a dynamical description of the tangential projection of liquid motion at a solid boundary. Important omissions from a theory based solely on the FK equation include:

1. The second degree of freedom tangential to the interface (surfaces are 2-D).

2. The explicit dependence on the degree of freedom perpendicular to the interface.

With regards to 1, Braun and Kivshar [66] have addressed quasi-two-dimensional motion in a model of transversely coupled FK chains in the continuum limit ($k \to \infty$) and derive an effective Hamiltonian governing the transverse dynamics of kinks (defects). This type of coupling may introduce some new dynamical effects. However, in the context of slip, we expect that the relevant dynamics will be aligned with the direction of forcing and that a 1-D approximation to the anisotropic system is acceptable. Transverse particle diffusion should not qualitatively affect the results presented here.

With regards to 2, the momentum transfer term in 4.2, $\eta_{ff}(V - \dot{x}_i)$, is a discretized shear rate at the interface and as such attempts to capture the velocity gradient perpendicular to the interface. Nonetheless, particle motion perpendicular to the interface may change the slip behavior qualitatively and cannot be explicitly captured in 4.2. Only comparison with MD simulations can reveal to what extent the perpendicular motion of the liquid particles is important. In fact, we shall see that careful observation of the vertical flux in MD simulations will allow us to modify the FK model to precisely address this second point.

The most interesting, and luckily most robust, prediction of this work is the existence of two slip regimes: one defect-driven and the other, a bulk-slip regime. The bottom line of all the results to follow is that as the forcing of the liquid particles at the interface (e.g. shear rate) increases from zero, slip will generically occur first due to localized dislocations, followed by a second transition to bulk slip. [2]

In the following sections we will present an overview of the determination of $f_{cr}(\xi, k, \eta)$ and $v_{slip}(\xi, k, \eta, f - f_{cr})$ in the damped, driven FK model, filling in blanks where results have not been presented in the literature. We will then discuss the results of MD simulations and compare them to those of a newly proposed, modified FK model.

4.4 Commensurate chains with integer values of ξ

The dynamics of those chains for which ξ is an integer is equivalent to that of a single particle. In this case the coupling term, in the absence of noise, is identically equal to zero

$$\ddot{x}_i = -\sin x_i + f - \eta \dot{x}_i. \tag{4.19}$$

It should be noted that if the particles are inhomogeneously spaced initially, then the dynamics will exhibit a coupling-dependent transient. However, for sufficiently long times, 4.19 will be an asymptotically correct description of the particle motion.

The dynamics of 4.19 are very simple. For $f < 1$ there are two equilibria given by $x_{eq} = \sin^{-1} f$; if x_s and x_u denote the stable and unstable equilibria respectively, then $x_u = \pi - x_s$ for $0 \leq x_s \leq \pi/2$. Note that 4.19 is also the equation of motion for a forced pendulum, in which case x_s is the pendulum hanging down and x_u is the position at which the pendulum can be balanced on end. As f approaches 1, the two

---

[2] As a note, the large degree of shear needed to reach the bifurcation to bulk slip may be physically unrealizable. We thus expect the defect-driven regime to be the dominant paradigm of liquid slip in the regime where the present study is valid.

equilibria coalesce in a saddle-node bifurcation (SN) at $x_s = x_u = \frac{\pi}{2}$, at which point the energy barrier to particle motion vanishes. An equation of motion for the particle near the SN ($|f-1| \ll 1$) is easily derived, yielding

$$\dot{x} = \frac{f-1}{\eta} + \frac{1}{2\eta}x^2. \tag{4.20}$$

Equation 4.20 is simply the normal form equation for a SN and clearly shows the existence of two equilibria for $f-1 < 0$. We can make use of the fact that the motion is periodic (SN on a circle) by transforming the position x into a phase with $x(t) = \tan\left(\frac{\theta(t)}{2}\right)$ [3]. Plugging this into 4.20 gives

$$\dot{\theta} = \omega + b\cos\theta \tag{4.21}$$

with $\omega = \frac{2f-1}{\eta}$, $b = \frac{2f-3}{\eta}$ and $-\pi < \theta < \pi$. This formulation takes advantage of the fact that for $f-1 \ll 1$ the particle spends most of its time near the SN point. Once it escapes ($x \to \infty$ as $\theta \to \pi$), it travels to the next 'hill' where it once again hangs around the SN point and so on. Thus the time it takes for the particle to traverse one period of the substrate can be approximated as

$$T_{SN} = \int_{-\pi}^{\pi} \frac{d\theta}{\omega + b\cos\theta}, \tag{4.22}$$

and the non-dimensional slip velocity is given by $v_{slip} = \frac{2\pi}{T_{SN}}$. The solution of 4.22 is

---

[3] Interestingly, this bifurcation (SN on a circle) is also ubiquitous in single-neuron dynamics where the excursion to infinity is interpreted as an action potential. The resulting phase equation 4.21 is known as the θ-equation for 'class 1' excitable neurons [67].

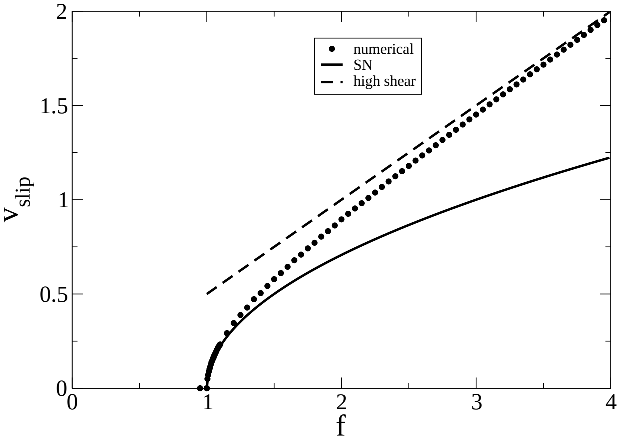

Figure 4.2: Chains for which ξ is an integer (here 20) exhibit a SN bifurcation at a critical shear rate. Here $\eta_{ff} = \eta_{fs} = 1$, $h = 1$, $\lambda = 2\pi$ and $k = 1$. Equation 4.2 was solved with a 4th-order Runge-Kutta scheme and long-time averages were taken.

$\frac{2\pi}{\sqrt{\omega^2 - b^2}}$, which gives

$$v_{slip} = \frac{\sqrt{2}}{\eta}\sqrt{f - 1}. \tag{4.23}$$

Finally, in dimensional variables

$$v_{slip} = \frac{2\pi}{\lambda}\sqrt{\frac{2}{h}}\frac{\sqrt{\frac{\lambda\eta_{ff}V}{2\pi h} - 1}}{(\eta_{ff} + \eta_{fs})}. \tag{4.24}$$

Thus, for integer values of ξ, the particles are trapped below a critical value of the forcing (shear rate) beyond which the slip velocity increases like the forcing to the 1/2 power. For large shear rates, 4.3 once again applies; see figure 4.2.

4.5 Commensurate chains with ξ near an integer value

If we consider a chain with a value of ξ very close to an integer value (e.g. $\frac{100}{101}$) we see that the ground state of the system corresponds almost everywhere to that of the respective chain with exactly the integer value. Only at a few points will the addition (absence) of particles cause a contraction (expansion) of the chain. In the case $\xi = \frac{100}{101}$, there is one extra particle per one hundred periods of the potential, referred to as a *dislocation* or *defect*.

In fact, we will see that a single defect in the undamped, unforced FK model corresponds to a kink (soliton) in the integrable limit (sG), and that the correspondence is exact for $k \to \infty$. Kink solutions [58] to 4.15 have the form

$$U_k(X,T) = 4\tan^{-1}\left\{\mathrm{e}^{-\sigma\frac{(X-\bar{V}T)}{\sqrt{1-\bar{V}^2}}}\right\} \tag{4.25}$$

which in dimensional form (from 4.14) is

$$u_k(x,t) = \frac{2\lambda}{\pi}\tan^{-1}\left\{\mathrm{e}^{-\frac{2\pi\sigma\sqrt{h}}{c\lambda}\frac{(x-\bar{v}t)}{\sqrt{1-\frac{m\bar{v}^2}{c^2}}}}\right\}. \tag{4.26}$$

The velocity of the kink $\bar{V}$ should not be confused with the velocity in 4.2 and is distinguished here by the overbar.

Depending on the sign of $\sigma = \pm 1$, the kink 4.25 is a front solution twisting through $\pm 2\pi$. The velocity $\bar{v}$ is a free parameter indicating that there is no selected velocity.

In the case of the weakly forced, weakly damped sG equation

$$\ddot{U} - U^{''} + \sin U = f - \eta \dot{U} \tag{4.27}$$

where for $f, \eta \ll 1$, a perturbation analysis yields a soliton solution which to leading order is equal to the unperturbed soliton 4.26. At next order the velocity is uniquely determined [57]. The steady-state value is

$$\bar{V} = \frac{1}{\sqrt{1 + \left(\frac{4\eta}{\pi f}\right)^2}}, \tag{4.28}$$

which in dimensional form is

$$\bar{v} = \frac{a\sqrt{\frac{k}{2m}}}{\sqrt{1 + \left(\frac{4(\eta_{ff}+\eta_{fs})}{\pi \eta_{ff} V}\right)^2 \frac{h}{m}}}. \tag{4.29}$$

Let us now turn our attention once again to the FK model and consider the quantity v_{slip} defined by 4.18 as a function of the parameter ξ. As we see in figure 4.3, the slip is identically zero for the cases where ξ is an integer (we are just at the SN bifurcation in a system of 100 periods of the underlying potential, i.e. $\xi = 100/p$ where p is the number of particles). The slip increases monotonically as ξ deviates from integer values. Specifically, for a fixed value of k, the slip velocity increases initially linearly as a function of $1/\xi$. In this regime, the density of defects is low (see 4.17) and the slip velocity is therefore simply proportional to this density. As the density of defects increases, they begin to interact with one another and the slip

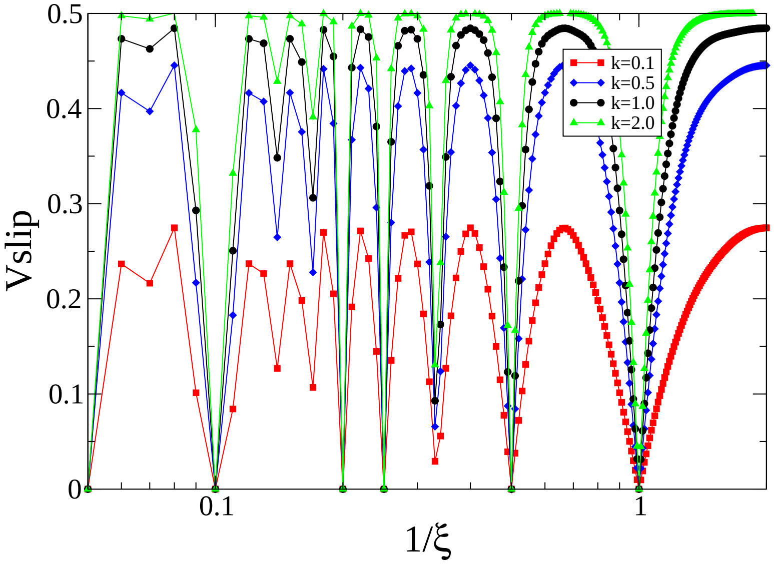

Figure 4.3: Slip velocity vs. $\frac{1}{\xi}$. The number of periods of the substrate is 100 and the number of particles in the chain increases from left to right. Parameter values are as in figure 4.20 except for the forcing V which is fixed at 1. All curves go to zero monotonically as $\xi \to 0$. Lines are meant as guides to the eye only.

velocity deviates from a linear dependence. Finally, for ξ sufficiently far from an integer value, individual defects are not discernible and the dynamics is described by a dynamic hull-function, discussed below. Also, for a fixed value of ξ, the slip velocity increases as the coupling k increases.

Note that here, given $\eta_{ff} = \eta_{fs} = V = 1$, the maximum possible slip velocity is $\frac{1}{2}$. For larger values of $1/\xi$ ($\xi \to 0$) all curves approach zero monotonically. In fact, as ξ decreases for a fixed system size, the number of particles increases. The case $\xi \to 0$ is then the limit in which the interparticle spacing goes to zero, i.e. the continuum limit. A simple bifurcation anaylsis of the forced, damped sine-Gordon equation shows that the SN bifurcation at $f = 1$ is once again recovered, i.e. the slip goes to zero for $f \leq 1$.

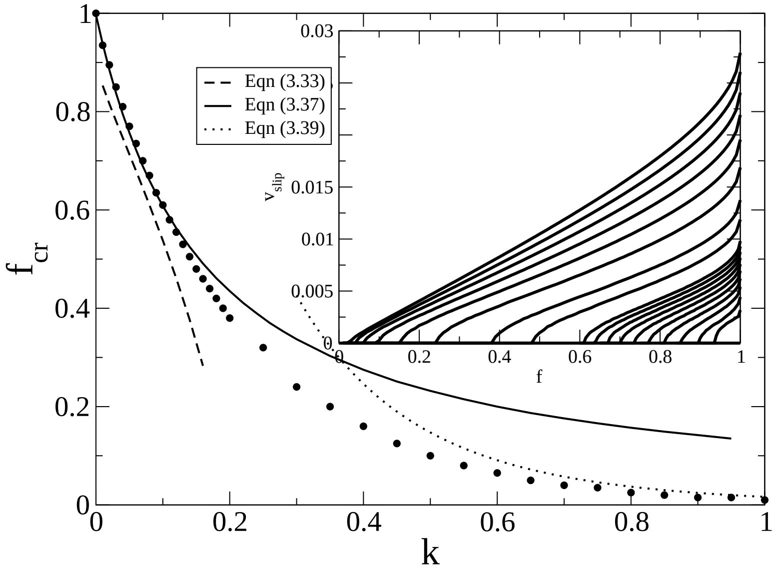

Figure 4.4: Inset: Slip velocity vs. force for a single defect for various values of the coupling $k = 0.01 - 0.1$ in increments of 0.01 then $k = 0.15, 0.2, 0.3, 0.4, 0.5, 0.6, 0.7, 0.8$. Slip increases for increasing k. Main: Depinning force vs. coupling k for a single defect.

The inset of 4.5 shows the region near an integer value of ξ. Equation 4.29 predicts the velocity of a kink should increase as $k^{\frac{1}{2}}$. If we normalize curves for different k's by this factor there is good collapse, as seen in the main panel of figure 4.5. Note that 4.29 is for *weakly* driven, *weakly* damped kinks in the *continuum* limit. Despite this, it captures the correct scaling for coupling strength even for *strongly* driven, *strongly* damped kinks in the *discrete* system. For values of ξ not too far from one we expect the defects to be far apart from one another (dilute limit) and thus not interact strongly. Then the average slip should be approximately proportional to the number of defects. The curves in figure 4.5 are linear near $\xi = 1$, in agreement with the notion that the defects interact weakly.

Figure 4.3 shows the average velocity of the chain for a fixed value of the forcing.

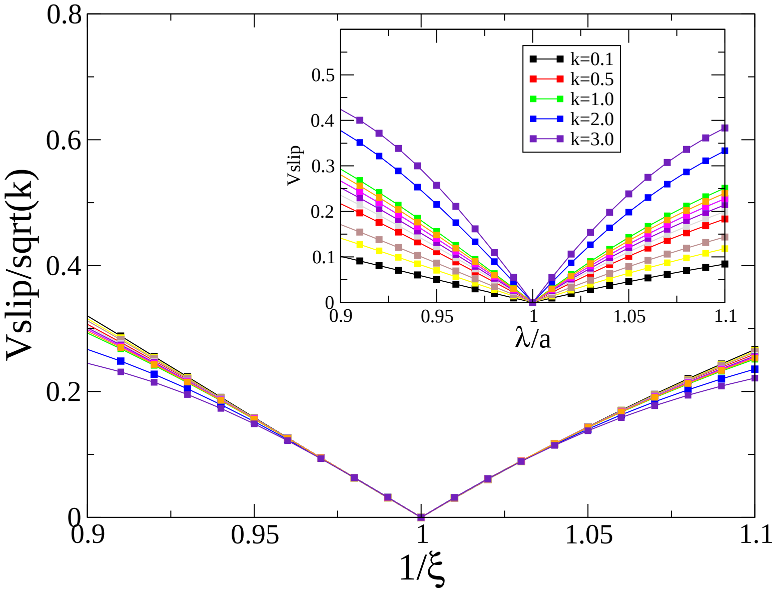

Figure 4.5: Inset: ξ near 1 from figure 4.3. Main: Curves rescaled by the predicted soliton dependence on coupling given by 4.26.

We have seen that for integer values of ξ there is a SN bifurcation to slip at a critical value of the forcing, below which there is no motion. We may ask, given that noninteger values of ξ lead to slip already below this SN bifurcation, whether chains with defects also exhibit a bifurcation to motion, or if any force is sufficient to move the defect. The answer is already given by the discrete translational symmetry of the defect. It is invariant under translations of one period and therefore feels a pinning force. We can determine this pinning force explicitly in the limits of weak and strong coupling (c.f. figure 4.4).

For $k \ll 1$ we solve for the stable and unstable configurations of the ground-state of a single, forced kink evolving according to 4.2, by assuming that deformations of the chain are localized near the kink position. Once we have solved for the ground state (x_i's) we can determine the energy of the kink from the Hamiltonian 4.1. Schematic

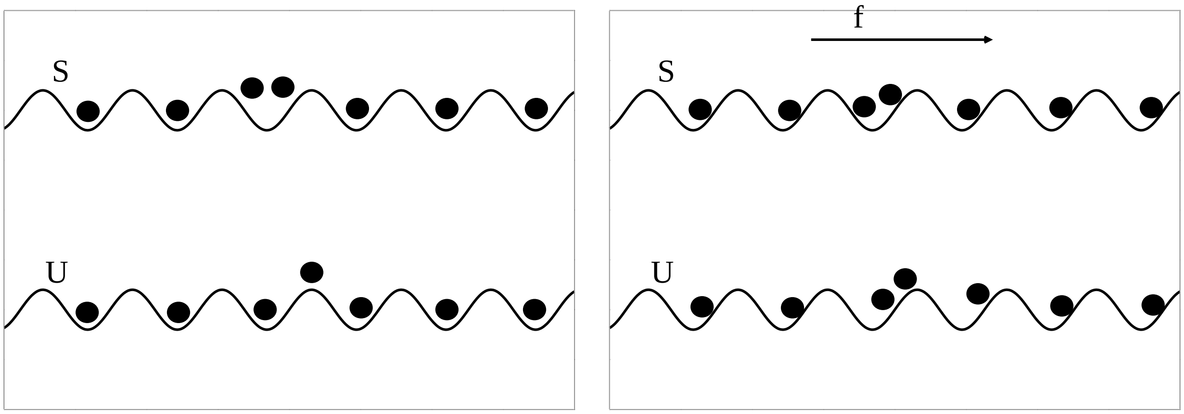

Figure 4.6: Schematic stable and unstable configurations for weakly-coupled kinks. Left: Unforced. Right: forced.

ground states are shown in figure 4.6. For f sufficiently far from 1 (f must be at least order k from the SN bifurcation to bulk slip) this yields

$$\begin{aligned} E_s &= N(1-\sqrt{1-f^2}) + 2k\pi^2 + \mathcal{O}(k^2) \qquad (4.30) \\ E_u &= N(1-\sqrt{1-f^2}) + 2\sqrt{1-f^2} + k\pi^2 + 4k\psi\Big(\psi - \frac{2f}{\sqrt{1-f^2}}\Big) \\ &\quad + \mathcal{O}(k^2) \qquad (4.31) \end{aligned}$$

where N is the number of particles in the chain and $\psi = \sin^{-1} f$. Taking the difference between these two energies gives the Peierls-Nabarro potential

$$E_{PN}(f) = 2\sqrt{1-f^2} - k\pi^2 + 4k\psi\Big(\psi - \frac{2f}{\sqrt{1-f^2}}\Big) + \mathcal{O}(k^2). \qquad (4.32)$$

In the limit $f \to 0$ one recovers the classical result [55]

$$E_{PN}(0) = 2 - k\pi^2 + \mathcal{O}(k^2) \qquad (4.33)$$

From the energy 4.32 we can calculate the critical forcing at which the defect will first move

$$f_{cr} = \frac{E_{PN}(f_{cr})}{\lambda}. \tag{4.34}$$

Unfortunately, while 4.32 gives the asymptotically correct energy for small k, it breaks down near $f = 1$. Figure 4.4 shows the predicted f_{cr} using 4.32.

We can alleviate this problem by considering next-order corrections to the ground-state positions of the particles. In this case we expand f near 1 ($f = 1 - \epsilon\bar{f}$), which leads to different zeroth order terms. This gives

$$\begin{aligned}
E_s &= N(1-\sqrt{1-f^2}) + 2\pi^2 k + 2\sqrt{2(1-f)} \\
&\quad -\sqrt{2(1-f)}\left(\sqrt{1+\frac{2\pi kf}{1-f}} + \sqrt{1-\frac{2\pi kf}{1-f}}\right) + \mathcal{O}(k^{3/2}) \qquad (4.35)\\
E_u &= N(1-\sqrt{1-f^2}) + k(\pi^2+4\psi^2) + 2\sqrt{1-f^2} \\
&\quad +\sqrt{2(1-f)}\left(1+\sqrt{1-\frac{4kf\psi}{1-f}} - \sqrt{1+\frac{kf(\pi+2\psi)}{1-f}}\right. \\
&\quad \left. -\sqrt{1-\frac{kf(\pi-2\psi)}{1-f}}\right) + \mathcal{O}(k^{3/2}). \qquad (4.36)
\end{aligned}$$

The Peierls-Nabarro potential is then

$$\begin{aligned}
E_{PN} &= 2\sqrt{1-f^2} - k(\pi^2-4\psi^2) - \sqrt{2(1-f)} + \sqrt{2(1-f)}\left(\sqrt{1-\frac{4kf\psi}{1-f}}\right. \\
&\quad -\sqrt{1+\frac{kf(\pi+2\psi)}{1-f}} - \sqrt{1-\frac{kf(\pi-2\psi)}{1-f}} \\
&\quad \left. +\sqrt{1+\frac{2kf\pi}{1-f}} + \sqrt{1-\frac{2kf\pi}{1-f}}\right) + \mathcal{O}(k^{3/2}). \qquad (4.37)
\end{aligned}$$

If we expand $\psi = \sin f^{-1}$ for $f \sim 1$ this can be reduced to

$$E_{PN} \sim 2\sqrt{1-f^2} - 2\sqrt{2(1-f)}\left(1 - \sqrt{1 - \frac{2\pi k f}{1-f}}\right). \tag{4.38}$$

Equation 4.38 is plotted in figure 4.4 and shows good agreement with numerical data for k sufficiently small.

For $k \gg 1$ one can introduce the continuum limit defect solution 4.14 as a quasi-particle into 4.2. This couples an additional 2 degrees of freedom to the Hamiltonian 4.1 for the position and velocity of the defect bringing the total to $2N+2$ [68]. In this formulation the Peierls-Nabarro potential is found to be

$$E_{PN} \sim 32\pi^2 k e^{-\pi^2\sqrt{k}}. \tag{4.39}$$

Comparison of 4.39, a classical result, with numerical data in 4.4 shows good agreement for large enough k, as expected.

4.6 Non-integer values of ξ

For values of ξ not too far from an integer value the chain of particles in the FK model can be thought of as an integer chain with a fixed density of defects. As ξ deviates further from an integer value this picture breaks down. Expansions and compressions of the chain are no longer localized and the we expect the dynamics to have a more homogeneous nature. A fruitful approach to calculating the steady-state velocity of a forced chain in this regime is to examine the total energy of the system [63].

As a reminder, we are dealing with the nondimensionalized FK equation of the form

$$\ddot{x}_i = -\sin x_i + k\triangle^\dagger\triangle x_i - \eta\dot{x}_i + f. \tag{4.40}$$

We multipy 4.40 by the velocity $\dot{x}_i$ of particle i, and integrate over time and over all N particles

$$\begin{aligned} < \frac{1}{2}\frac{d}{dt}(\dot{x}_i^2) > &= < \frac{d}{dt}\cos x_i > + k < \dot{x}_i\triangle^\dagger\triangle x_i > + \eta < \dot{x}_i^2 > + f < \dot{x}_i >, & (4.41) \\ < (\cdot) > &= \lim_{T\to\infty}\frac{1}{T}\int_0^T dt\frac{1}{N}\sum_{j=1}^{N}(\cdot). & (4.42) \end{aligned}$$

Equation 4.41 holds generally. We further assume that the motion of the chain is periodic, with period $\bar{T}$, the time it takes to traverse a single period of the underlying potential. In this case, both the inertial term and the energy related to the substrate potential vanish. The energy related to the coupling vanishes due to the fact that a sum over all particles yields zero for periodic boundary conditions. The remaining terms balance, giving

$$fv = \eta < \dot{x}_i^2 > \tag{4.43}$$

which expresses that the rate of work done to drive the chain at a mean velocity v exactly balances the rate of energy loss. Note that v has the same definition as v_{slip} in 4.18.

Consistent with the notion that the chain of particles exhibits periodic motion, we introduce the ansatz

$$x_i = \Psi + a \cdot i + v \cdot t + h(\Psi + a \cdot i + v \cdot t) \equiv \phi + h(\phi) \tag{4.44}$$

where a is the inter-particle spacing, v is the velocity and Ψ is an arbitrary phase. The *hull* function [69] $h(\phi)$, (not to be confused with the amplitude of force h due to the substrate), is periodic with the period of the substrate potential and expresses the oscillatory deviation from purely rectilinear motion of the particles. Plugging 4.44 into 4.40 yields

$$v^2\ddot{h} = -\sin(\phi + h) + k\Big[h(\phi + a) - 2h(\phi) + h(\phi - a)\Big] - v\eta(1 + \dot{h}) + f, \tag{4.45}$$

where the overdot is a derivative with respect to the phase ϕ. Note that 4.45 can be viewed as an eigenvalue problem for the velocity v, and in general must be solved numerically. However, analytical solutions can be obtained in several meaningful limits. Strunz and Elmer [63] solved for h in the limit of small-amplitude substrate potential. We consider here the limit that the inter-particle coupling is strong, which facilitates analysis considerably. We define a smallness parameter ϵ and take

$$k = \frac{1}{\epsilon}\bar{k} \tag{4.46}$$

$$h = \epsilon h_0 + \mathcal{O}(\epsilon^2) \tag{4.47}$$

which when plugged into 4.45 yields, to leading order

$$0 = -\sin\phi + k\Big[h_0(\phi + a) - 2h_0(\phi) + h_0(\phi - a)\Big] - v\eta + f. \tag{4.48}$$

We see that the velocity, which is unkown, should also be expanded in ϵ (f is given).

It turns out we only need the zeroth order result $v = \frac{f}{\eta}$, which gives

$$h_0(\phi + a) - 2h_0(\phi) + h_0(\phi - a) = \frac{1}{\bar{k}} \sin\phi. \tag{4.49}$$

Assuming an ansatz for h of the form

$$h_0 = \bar{h}e^{i\phi} + c.c. \tag{4.50}$$

yields as a solution

$$h_0 = \frac{1}{4k(\cos a - 1)} \sin\phi. \tag{4.51}$$

We note that 4.51 holds for all particles and thus enables us to perform the average in 4.43 exactly since from 4.44

$$\begin{aligned} \dot{x}_i &= v(1 + \dot{h}(\phi)), && (4.52)\\ < \dot{x}_i^2 > &= \frac{v^2}{2\pi} \int_0^{2\pi} d\phi (1 + \dot{h_0})^2. && (4.53) \end{aligned}$$

Finally, we find the slip velocity to be

$$v_{slip} = \frac{f}{\eta\Big(1 + \frac{1}{8k^2[\cos a - 1]^2}\Big)}. \tag{4.54}$$

Figure 4.7 shows good agreement between 4.54 and numerical data even for relatively weak inter-particle coupling ($k = 0.5$). The hull-function approach breaks down for near-integer values of ξ, as expected.

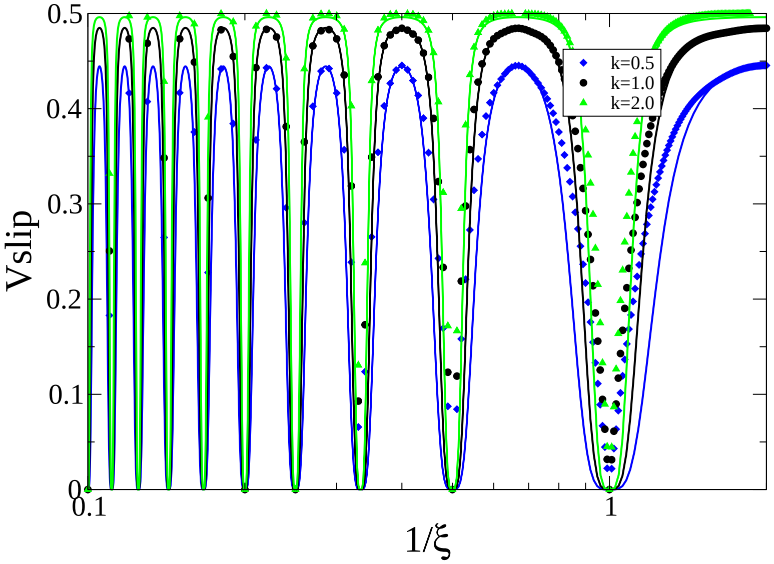

Figure 4.7: A comparison of the predicted slip velocity given by 4.54 (curves) and numerical data (symbols).

4.7 The FK model and Liquid Slip

The FK model has been broadly evoked to describe dislocations in solids and solid-solid friction. It is less clear what relevance such a model may have for a liquid-solid interaction. In particular, the high degree of order implicit in the model is reasonable for solids. Particles have well-defined neighbors and thermal fluctuations are extremely unlikely to overcome the force of attraction between the particles. Thus diffusion is assumed negligible.

The same can, in general, not be said of a liquid. Thermally-driven diffusion is the hallmark of liquid particle motion and the underpinning of our statistical-mechanical description of liquid velocity distributions. In this section we will describe how liquid particle motion at a solid interface can at least be qualitatively understood within the FK framework. The surprise at the success of a theory for the dynamics of *solid-solid* interactions in the context of liquids will be lessened by a close look at liquid-particle motion at the interface in molecular dynamics simulations. Simulations reveal, as hinted at elsewhere [54], that the liquid layer nearest the interface is highly ordered compared to liquid in the bulk.

Liquid particles near the interface feel a corrugated, external potential. At the kinetic level of description, the equilibrium velocity distribution of the liquid particles will be altered by a Boltzmann prefactor which depends on the distance from the interface. In this sense it is obvious that particles near the interface may potentially exhibit significantly different velocity distributions from those in the bulk. This is precisely what makes a kinetic theory of liquid motion at an interface extremely challenging, although there have been recent attempts [70].

Our molecular-dynamics simulations reveal that the liquid is, in fact, highly ordered near the interface relative to the liquid in the bulk. The degree of the ordering depends crucially on the ratio of the strength of the liquid-liquid and liquid-solid potentials ($\frac{k}{h}$ in equation 4.2) and the relative magnitude of the thermal fluctuations (e.g. $\frac{k_B T}{h}$) (note that k_B is the Boltzmann constant, not the liquid-liquid coupling k!). We expect the theory proposed here to break down for $\frac{k}{h} \to \infty$ and $\frac{k_B T}{h} \to \infty$ which could be considered the non-wetting and large-fluctuation limits, respectively.

For not too large fluctuations and order one or larger wettability, the liquid particles nearest the interface act on short timescales essentially as a solid. This is due to the fact that the relatively strong attraction to the substrate leads to long residence-times of the particles at the interface. Nonetheless, thermal fluctuations lead to a constant flux of particles both towards and away from the interface on longer time scales. This injection and ejection of particles is equivalent to the creation and anihilation of defects in the chain. It is easily discerned in simulations that *defects cause slip.* Recourse to defect motion in the FK model provides a trivial explanation for this: the effective Peierls-Nabarro potential E_{PN} for defects is always less than that of the ground state. Defects simply require less work to move.

The value of ξ, too, plays an important role in simulations. Given an integer value of ξ, the liquid layer adjacent to the interface will find it energetically preferential to sit neatly in the potential wells of the substrate. Particle diffusion will create defects which may be sufficiently driven to induce slip. In the non-integer case the liquid particles feel a reduced E_{PN}. Particle diffusion may actually provide the liquid layer with a lower energy state for some time, making slip less likely.

In the final sections we will describe results from molecular dynamics simulations and show how these can be understood via a modified form of the FK equation.

4.8 Molecular Dynamics Simulations

Molecular Dynamics (MD) simulations have been, and continue to be, a powerful tool for examining the dynamics of micro- or nanoscale flows in liquid dynamics. For the question of slip at a solid interface they have proven invaluable given the paucity of theory [51, 52, 53, 54, 71]. For the present study in particular, MD provides a means of comparison to test the validity of predictions arising from analysis of slip in the FK model. In this sense we consider MD to be our 'experimental' data. All MD simulations were carried out by Shreyas Mandre, to whom I am indebted for the enlightening data. Much of the related discussion in this section is taken from his notes.

The details of the MD simulations can be found elsewhere ([72]) including a novel means of controlling temperature in the system. Here we limit ourselves to a brief description of the method.

The system consists of a two-dimensional Couette geometry with N liquid particles and N_w wall particles (taken in simulations to be 150 and 60 respectively unless otherwise noted, see figure 4.8). The system evolves according to Newton's second law

$$m_i \frac{dx_i}{dt} = -\nabla_{x_i} V + f_i \tag{4.55}$$

where x_i denotes the position of the i^{th} particle. The potential energy V has the form

$$\begin{aligned} V &= \sum_{i=1}^{N} \sum_{j=i+1}^{N} V_{ll}(|x_i - x_j|) + \sum_{i=N+1}^{N+N_w} \sum_{j=i+1}^{N+N_w} V_{ww}(|x_i - x_j|) \\ &\quad + \sum_{i=1}^{N} \sum_{j=N+1}^{N+N_w} V_{lw}(|x_i - x_j|), \end{aligned} \tag{4.56}$$

where the sums represent liquid-liquid, wall-wall, and liquid-wall interactions respectively. All interactions are modeled via the Lenard-Jones potential

$$V_{pq}(r) = 4\epsilon_{pq}\Big[\big(\frac{\sigma_{pq}}{r}\big)^{12} - \big(\frac{\sigma_{pq}}{r}\big)^{6}\Big]. \tag{4.57}$$

The parameters ϵ_{pq} and σ_{pq} are chosen appropriately such that the liquid and wall particles act as a liquid and a solid, respectively. The values ϵ_{ll},σ_{ll} and m_l are then normalized to 1. The solid particles are arranged in a three-layer, hexagonal array with a horizontal extent of 10 particle widths at the top and bottom walls. Boundary conditions are periodic. The wall particles are subjected to a constant driving force in the horizontal direction (inducing a Couette flow in the bulk liquid). It should be noted that the wall particles themselves are allowed to evolve freely according to 4.55 and are therefore not necessarily moving at a constant velocity.

It is worth considering the potential energy of a layer of liquid particles near the substrate, as this is the paradigm of interest. We can easily derive an approximate contribution to the potential energy from the horizontal arrangement of the wall particles using 4.56. We assume that the particles sit at a distance d above the wall and that they deviate but little from their equilibrium positions. The potential energy of a single liquid particle due to the wall (assuming an infinite wall) is

$$\begin{aligned} V_{lw}^{horiz.}(x) &= V_{lw}(\sqrt{d^2+x^2}) \\ &+ \sum_{j=1}^{\infty}\Big[V_{lw}(\sqrt{d^2+(j\lambda-x)^2})+V_{lw}(\sqrt{d^2+(j\lambda+x)^2})\Big] \end{aligned} \quad (4.58)$$

where x is the spatial variable parallel to the wall and λ is the inter-particle spacing of the wall particles. Noting that $V_{ls}^{horiz.}(-x) = V_{ls}^{horiz.}(x)$, we represent 4.58 as a cosine series

$$V_{lw}^{horiz.} = \sum_{n=0}^{\infty} A_n \cos\big(\frac{2\pi x n}{\lambda}\big). \quad (4.59)$$

We see that the value of h in 4.1 is just

$$h = \frac{2}{\lambda}\int_0^{\lambda} dx \cos\big(\frac{2\pi x}{\lambda}\big) V_{lw}^{horiz.}(x), \quad (4.60)$$

and we have truncated the series after the first harmonic. The integral 4.60 must be performed numerically and may depend in a complicated way on σ_{lw}. However, it is clear that $h \propto \epsilon_{lw}$.

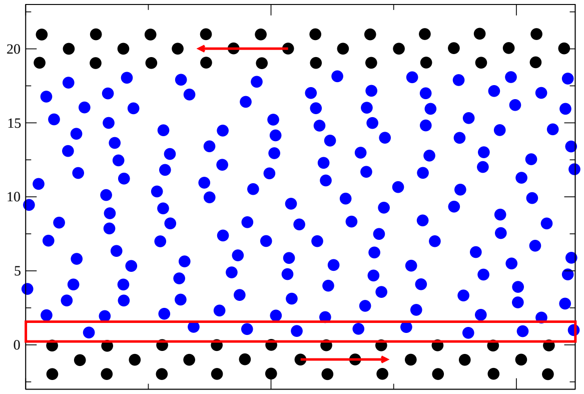

Figure 4.8: Snapshot of the MD simulation. Liquid particles are blue, solid particles black. The red arrows indicate the direction of the force on the solid particles. The red box indicates the area which is considered to be the 'first' layer. It is approximately one and one half particle diameters in thickness.

Let us turn to the contribution to the potential energy from the other liquid particles within the layer. By setting $V_{ll}(r_o) = 0$, we solve for the equilibrium inter-particle spacing $r_o = 2^{\frac{1}{6}}\sigma_{ll}$. Retaining only nearest-neigbor interactions, we assume particles deviate only slightly from their equilibrium positions. We can then expand $V_{ll}(x)$ in a Taylor series where $x = r_o + \hat{x}$ and $\hat{x} \ll 1$, yielding

$$V_{ll} \sim \frac{72}{2^{\frac{4}{3}}}\frac{\epsilon_{ll}}{\sigma_{ll}^2}(x_{i+1} - x_i)^2, \tag{4.61}$$

which reveals that $k = \frac{72}{2^{\frac{4}{3}}}\frac{\epsilon_{ll}}{\sigma_{ll}^2}$ in 4.1.

The preceeding calculations show that the parameters h and k in the FK model can be meaningfully related to the parameters of the Lennard-Jones potential in the MD simulations. It is less obvious how one would calculate the effective momentum transfer between liquid particles and energy loss to the wall particles. Nonetheless, qualitative agreement between results from the FK model and MD simulations indi-

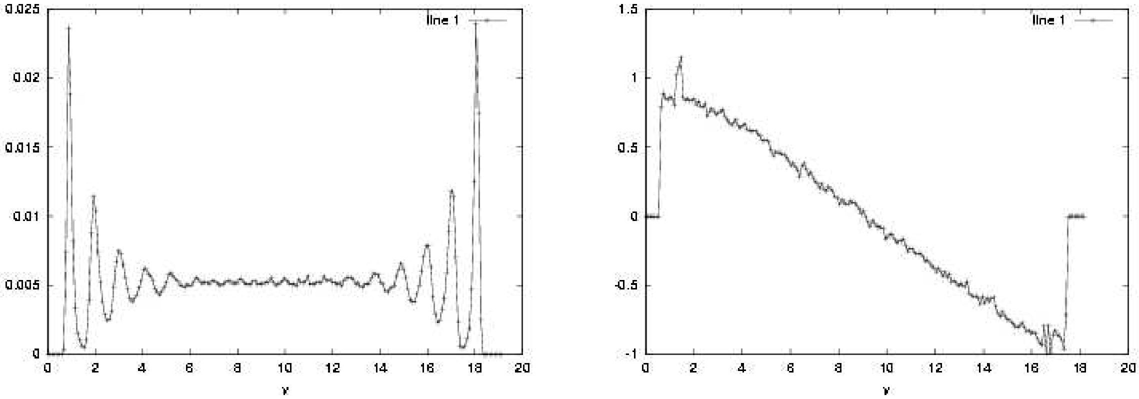

Figure 4.9: Typical density and velocity profiles for the Couette flow geometry in the MD simulations. Endpoints in the velocity profile should be ignored: there were too few sample points to provide good averages very close to the wall.

cate that dissipation at the wall can be effectively modeled as in 4.2. In what follows we will compare the motion of liquid particles in MD near the wall to that of particles in the FK model 4.2. Special care is given to examining the effect of transport of particles *perpendicular* to the wall, as this has potentially profound consequences for the validity of 4.2 as a model of liquid slip.

To verify the validity of results obtained in our MD simulations we compare equilibrium density profiles both parallel and perpendicular to the wall in the absence of forcing and velocity profiles for non-zero forcing to published results. Figure 4.9 (left) shows a typical density profile perpendicular to the wall for MD simulations of liquids in a Couette geometry [51, 54]. Characteristic are the peaks and troughs in the density near the wall, decaying in amplitude towards the bulk where the density is essentially homogeneous. The spacing of the peaks corresponds to about one and a half particle widths. The density profile parallel to the wall in figure 4.10 shows the high degree of order imposed on the liquid particles by the wall. Figure 4.9 (right)

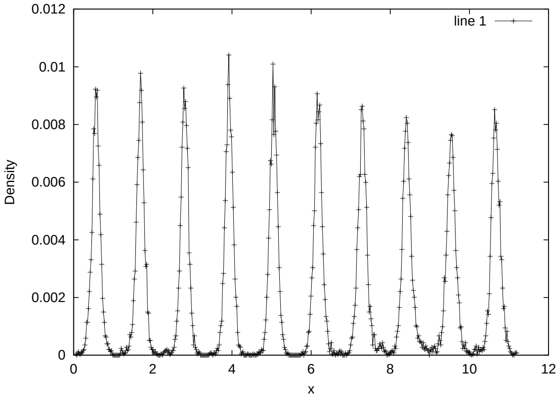

Figure 4.10: Typical average liquid density profile along the interface.

shows that velocity profiles of the liquid particles for non-zero forcing are indeed linear, as one expects in Couette flow. As observed elsewhere, slip occurs for large enough forcing, as exhibited by the non-zero relative velocity of liquid particles at the wall. Note that the information provided by figure 4.9 is averaged in time, which is necessary to achieve smooth velocity profiles.

Measuring the time-averaged slip velocity at the wall for different forcing amplitudes (or shear rates at the interface) allows one to formulate constitutive relationships between the two [52]. This can be done for various values of the Lennard-Jones parameters until a fairly complete picture of the parameter dependence is obtained. Yet, even if such a constitutive relationship were pinned down it would not elucidate the physical mechanism underlying the slip. Our central hypothesis is that such understanding can be gained by examining the *dynamics* of the liquid particles. This can be done without too much difficulty in the MD simulations.

The most straightforward approach towards characterizing the dynamics of the liquid particles is to observe their motion with one's own eyes. Figure 4.8 shows a typical snapshot of the system for $\frac{\epsilon_{lw}}{\epsilon ll} = \frac{\sigma_{lw}}{\sigma_{ll}} = 1$. In this case, in which the liquid-liquid and solid-solid inter-particle spacings are identical the liquid particles nearest the wall spend much of their time in the potential wells of the wall, although they vibrate due to the non-zero temperature.

Consider a frame of reference moving with the wall. Thus, if there is no slip, the liquid molecules adjacent to the wall would have zero velocity. We will assume that a force is applied in the right-hand direction and so, relative to the molecules at the wall, molecules in the bulk move to the left. By downstream we refer to motion in the direction of the forcing, that is, to the right.

The effect of the motion of the liquid particles above the layer adjecent to the wall is striking. From the point of view of a particular molecule, occasionally a molecule will pass overhead with a horizontal velocity to the left, exerting a force sufficient to dislodge the bound molecule. One of two events generically occurs in this case. The dislodged molecule either migrates upwards away from the wall or it proceeds (to the left) to the next potential well, thereby dislodging the liquid molecule residing there.

In the former case a potential well is left vacant. The downstream liquid particle (in the sense of the forcing) feels a strong upstream force due to the sudden absence of the repulsive force of its neighbor. It therefore jumps over the potential hump to occupy the vacant well. This hole clearly propagates downstream as particles jump one at a time to fill the vacancy. The propagation ends when a liquid molecule from above migrates into the potential well, thus restoring the wall layer to an integer value of ξ (defect-free state). Hole propagation can clearly be seen in the lower left hand panel in figure 4.11, initiated by the dissapearance of the fourth particle from the right, leading to the leftward motion of molecules 3, 2, and 1 respectively.

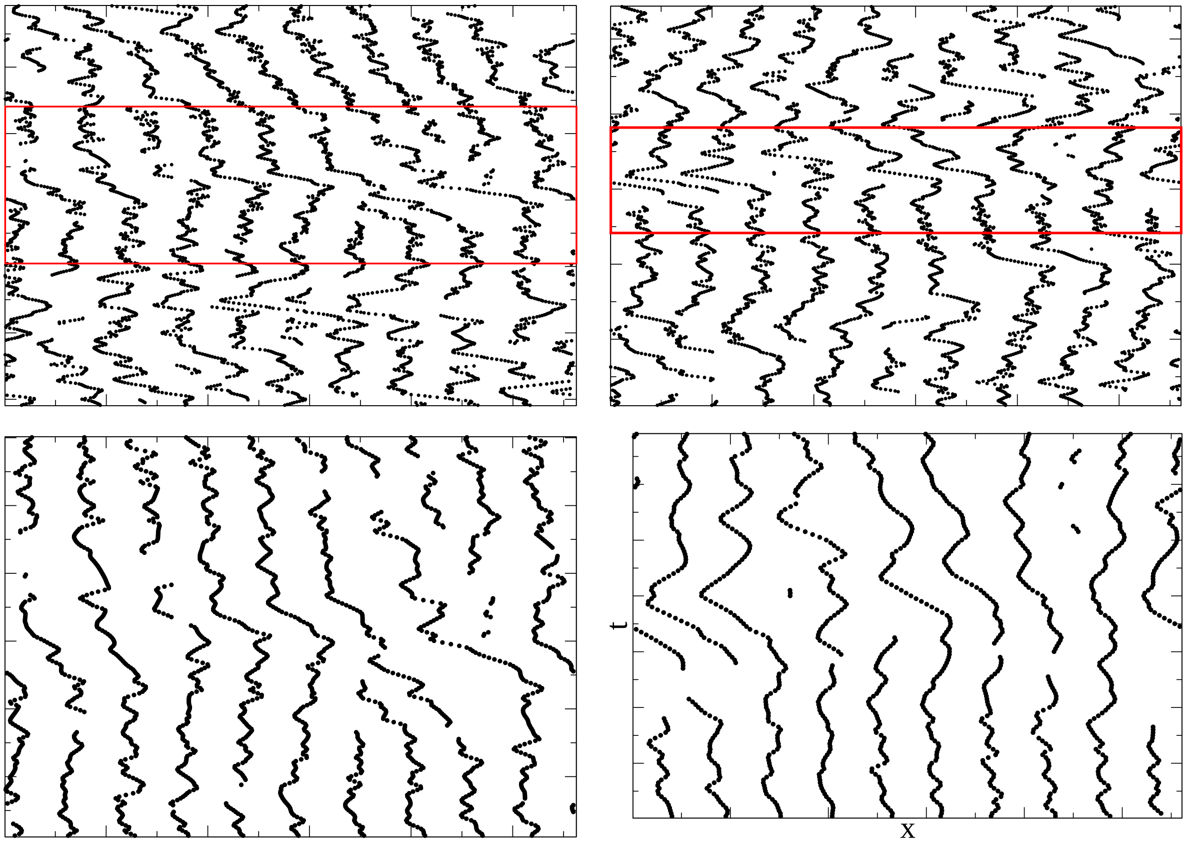

Figure 4.11: Typical particle trajectories for the layer of liquid at the interface. Bottom figures are blow-ups of the red boxes in the upper panels. Slip is indicated by leftward motion.

In the latter case the dislodging events also occur consecutively until an excess particle migrates upwards and the integer value of ξ is restored. In this case the propagation is upstream. Observation indicates that this scenario is less prevalent than the propagation of holes. Note that upstream propagation of an excess particle or downstream propagation of a hole both result in a net upstream transport of particles. This is precisely what is meant by liquid slip. We have already seen in much detail the effect of an excess particle or missing particle in a chain of particles in the FK model. This type of defect motion seems to be an appropriate description of the actual dynamical states arising in the MD simulations, which lead to net slip on the average.

Important for the degree of slip in the scenario described above is the rate at which particles leave and migrate to the interface. Indeed, it is this particle transport perpendicular to the wall that both leads to the creation and anihilation of defects. Figure 4.12 shows the rate of particle transport as a function of distance from the wall. This function looks strikingly similar to the density profile perpendicular to the wall, and in fact the particle transport dips down to very low values near the first trough. This means that the spike in particle density near the wall (the first layer) is comprised of particles which spend a considerable amount of time near the wall. Occasionally particles leave or enter the first layer, but on short enough time scales the particles can be reasonably modeled as a coherent chain.

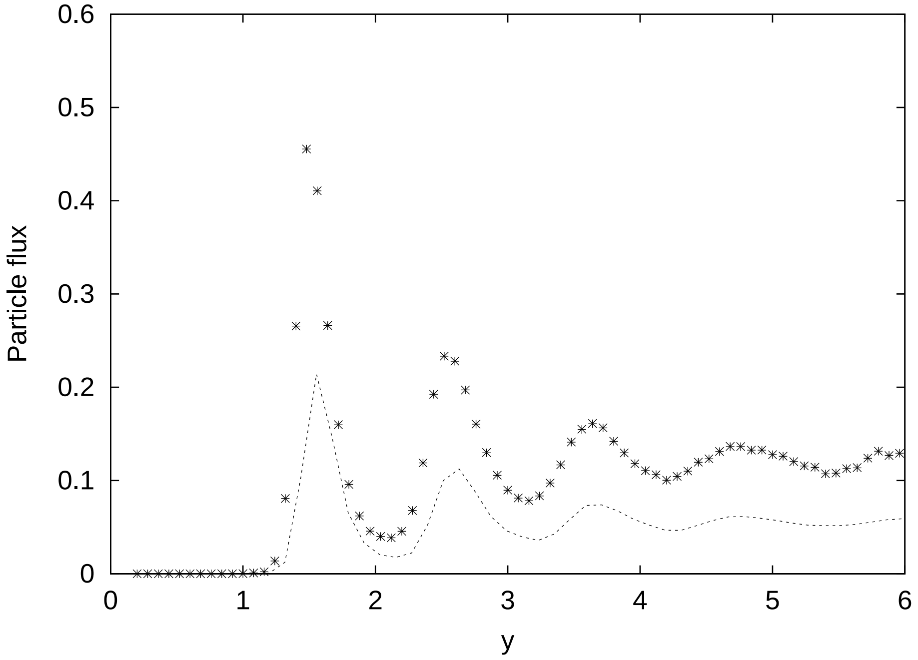

Figure 4.12: Typical liquid density (line of x's) and mass flux (dotted line) normal to the interface.

4.9 The variable-density Frenkel-Kontorova Model

We have dwelt much on the dynamics of the FK model in sections 4.2 through 4.7. In the last section we introduced some results from MD simulations and gave an anecdotal account of particle dynamics to motivate the usefulness of a FK-like model. We noted that the vertical flux of liquid particles was important for determining the rates of creation and anihilation of defects. In this section we propose a modified version of the FK model in which the number of particles may change in time. This occurs stochastically according to probabilities for seeding in or removing existing particles. As we shall see, the most realistic choice is of probabilities which depend themselves on the *current number of particles* [4] (nature hates a vacuum). We present a simple theory for calculating the slip velocity in this model. We conclude by comparing these results to those obtained in MD.

The variable-density Frenkel-Kontorova model (vdFK) is given by 4.2 with a rule for determing how the number of particles $N = N(x,t)$ should change in time and space. We choose a probabilistic algorithm. A new particle is added or a particle is taken away in a time unit dt with probability p_+dt and p_-dt respectively. In addition, these probabilities have the form

$$p_+ = p + \alpha[s - a]_+ \tag{4.62}$$

$$p_- = p + \alpha[a - s]_+ \tag{4.63}$$

where a and s are the number of particles added and subtracted and $[(\cdot)]_+$ is the

---

[4] Thanks to Shreyas for immediately noticing this.

positive rectifying function which is positive for positive argument and zero otherwise. The term proportional to α reflects the fact that the system prefers the defect-free state $a = s$. We might also have chosen a 'soft' dependence on the number of defects such as

$$p_+ = pe^{-\beta[s-a]_+} + (1 - e^{-\beta[s-a]_+}) \tag{4.64}$$

$$p_- = pe^{-\beta[a-s]_+} + (1 - e^{-\beta[a-s]_+}) \tag{4.65}$$

which varies continuously between p and 1 as a function of the number of defects.

The probability of having d defects as a function of time can be expressed as $p(d(t)) = p(|a(t) - s(t)| = d)$. The resulting probability density function *pdf* given 4.62 and 4.63 is discussed in the appendix C. In what follows we assume the form of the *pdf* is known. The *pdf* itself can be generated numerically from MD simulations.

We furthermore need to decide where the liquid particles should be seeded in and which ones should be removed. If an event occurs at time t_o then a particle is chosen at random from the $N(t_o)$ particles with probability $\frac{1}{N(t_o)}$. If a particle is to be added, it is placed, for simplicity, exactly between the selected particle i and particle $i+1$. Otherwise the selected particle is removed.

We summarize the model in non-dimensional form for clarity

$$\begin{aligned} \ddot{x}_i &= -\sin x_i + k\triangle^\dagger\triangle x_i - \eta\dot{x}_i + f, \\ N &= N(t), \end{aligned} \tag{4.66}$$

and emphasize that the vdFK model is non-deterministic due to the fluctuations in

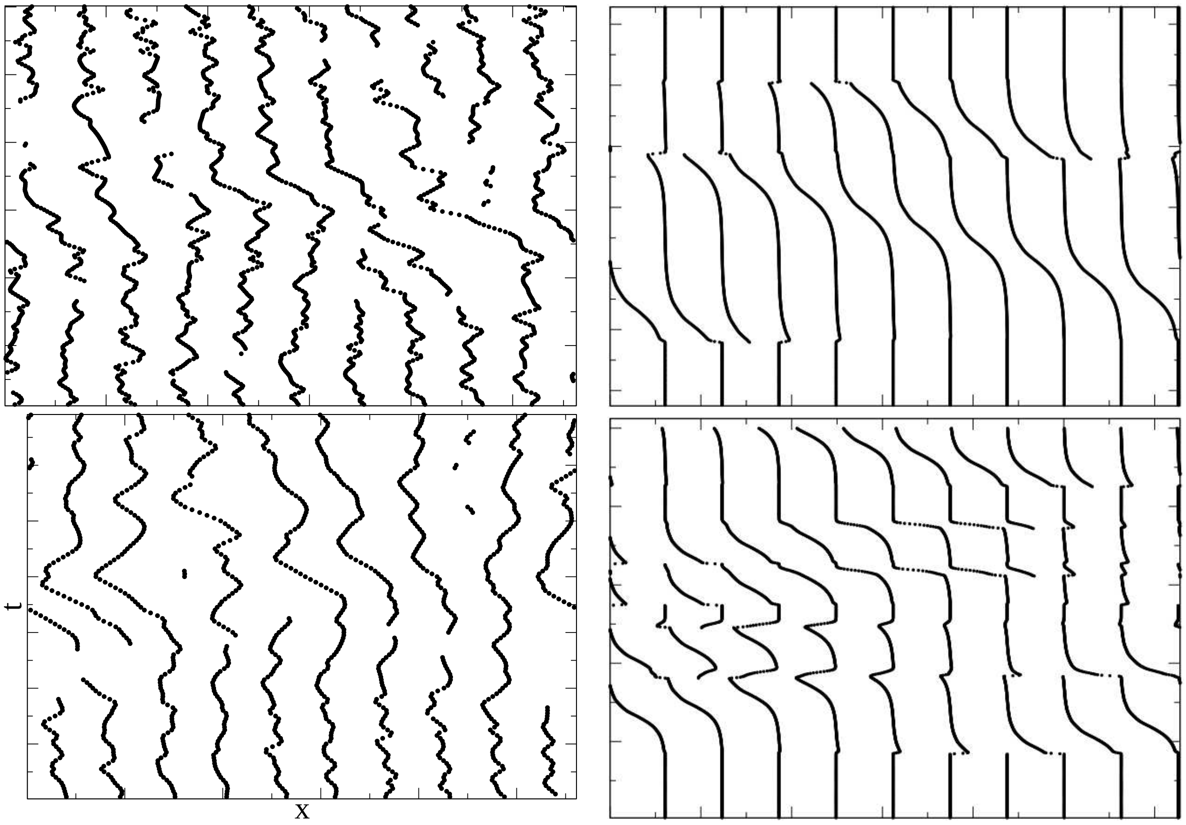

Figure 4.13: A qualitative comparison of liquid particle dynamics at the solid interface in the MD simulations (left) and in the vdFK equation (right).

the density of particles. Nonetheless, given the results already obtained in previous sections concerning the properties of defects in the FK model, we will be able to predict the slip velocity in the vdFK model for certain parameter values.

We first consider the case of an initially integer-commensurate value of ξ. We note that for $p_+ = p_- = 0$ the system exhibits no slip for $f \leq 1$ and that a SN bifurcation to bulk slip occurs at $f = 1$. In the case of n weakly interacting defects we have determined that for $f < f_{cr}$ no slip occurs, while for $f_{cr} = \frac{E_{PN}(f_{cr})}{\lambda}$ a SN bifurcation to defect motion occurs. Furthermore, the defect velocity is given by $v_d(f, \eta)$ and the total slip velocity is just $< v >= n \cdot v_d$.

A simple approximation of the slip velocity in 4.66 for weakly interacting defects would then be

$$< v >= \lim_{T \to \infty} \frac{v_d(f - f_{cr}, \eta)}{T} \int_0^T dtd(t), \tag{4.67}$$

which is just the velocity of a single defect times the average number of defects. We note that the velocity of holes is in general different than that of extra particles, but given the symmetry $p_+(a, s) = p_-(s, a)$, it is clear there should be as many holes on average as extra particles. Thus we can take $v_d(f, \eta) = \frac{v_{hole} + v_{particle}}{2}$ in 4.67. Once v_d is known, 4.67 can be calculated numerically for any simulation. However, if the *pdf* governing the evolution of $N(t)$ is known, 4.67 can, in theory, be calculated explicitly. We define the expected slip velocity

$$E(< v >) = \lim_{T \to \infty} \frac{v_d(f - f_{cr}, \eta)}{T} \int_0^T dtE(d(t)) \tag{4.68}$$

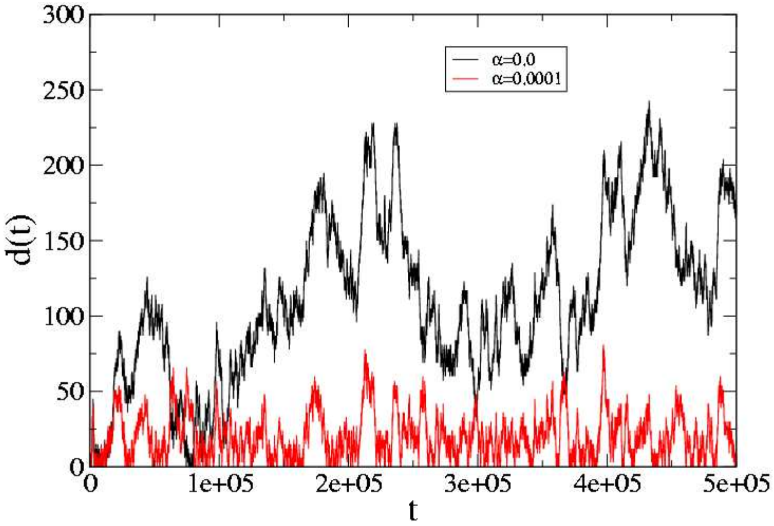

Figure 4.14: Number of defects as a function of time for both zero and non-zero α.

where

$$E(d(t)) = \sum_{d=0}^{\infty} d \cdot p(d(t)). \tag{4.69}$$

Equations 4.67 and 4.68 makes use of the steady-state velocity of moving defects in the FK model. When an extra particle is initially introduced, or one taken away, there will be a *transient* response before the steady state value is reached. For large enough particle fluxes, such steady state values may never be reached, i.e. before a defect reaches its steady state velocity, it is perturbed or anihilated. In this case equations 4.67 and 4.68 will break down and we must develop a theory of transients.

Dynamics in the vdFK equation

Here we take a closer look at the dynamics that arise in the vdFK model. We remark first on the importance of the parameter α which determines how strongly the system is attracted to the defect-free state. Figure 4.14 shows a sample time series of the number of ‘defects’ $d(t)$ for $p = 0.1$ and two different values of α. For $\alpha = 0.0001$ the value of $d(t)$ is already drastically reduced. This is important for two reasons. Firstly, it is what one sees in MD simulations and what one expects in a real liquid; the interfacial liquid particles will always tend to their ‘ground’ state, the most energetically preferred state. The particles constitute a driven system and thus defects arise, but the system will continually seek to anneal itself. Secondly, in the context of the vdFK model, large deviations in $d(t)$ and therefore ξ would result in jumps between qualitatively different types of behavior. If ξ varies only slightly, e.g. deviates but little from an integer commensurate value, then the ensuing dynamics can be described straightforwardly, e.g. as given by 4.67.

Consider figure 4.15. Left-hand figures show the velocity averaged over all particles in the vdFK model and the number of particles as a function of time. The forcing is $f = 0.0, 0.6, 1.2$ and increases from top to bottom, while the right hand figures show individual events in greater detail.

With zero forcing (uppermost figures) the response of the system to the addition or subtraction of a particle is complex. The effect on the average velocity of the system can be discerned as a localized spike of either positive or negative amplitude. A close-up view of such a spike in the velocity is shown on the right although much more complex responses can be seen as well.

The change in velocity due to the introduction of defects in the driven system (central panels) is much more straightforward. For nonzero values of $d(t)$, the velocity rapidly approaches a fixed value (although oscillations are, of course, present, as the righthand figure shows). Furthermore, the more defects present, the larger the velocity. In fact, it seems the effect of a defect is to cause a step of fixed amplitude in

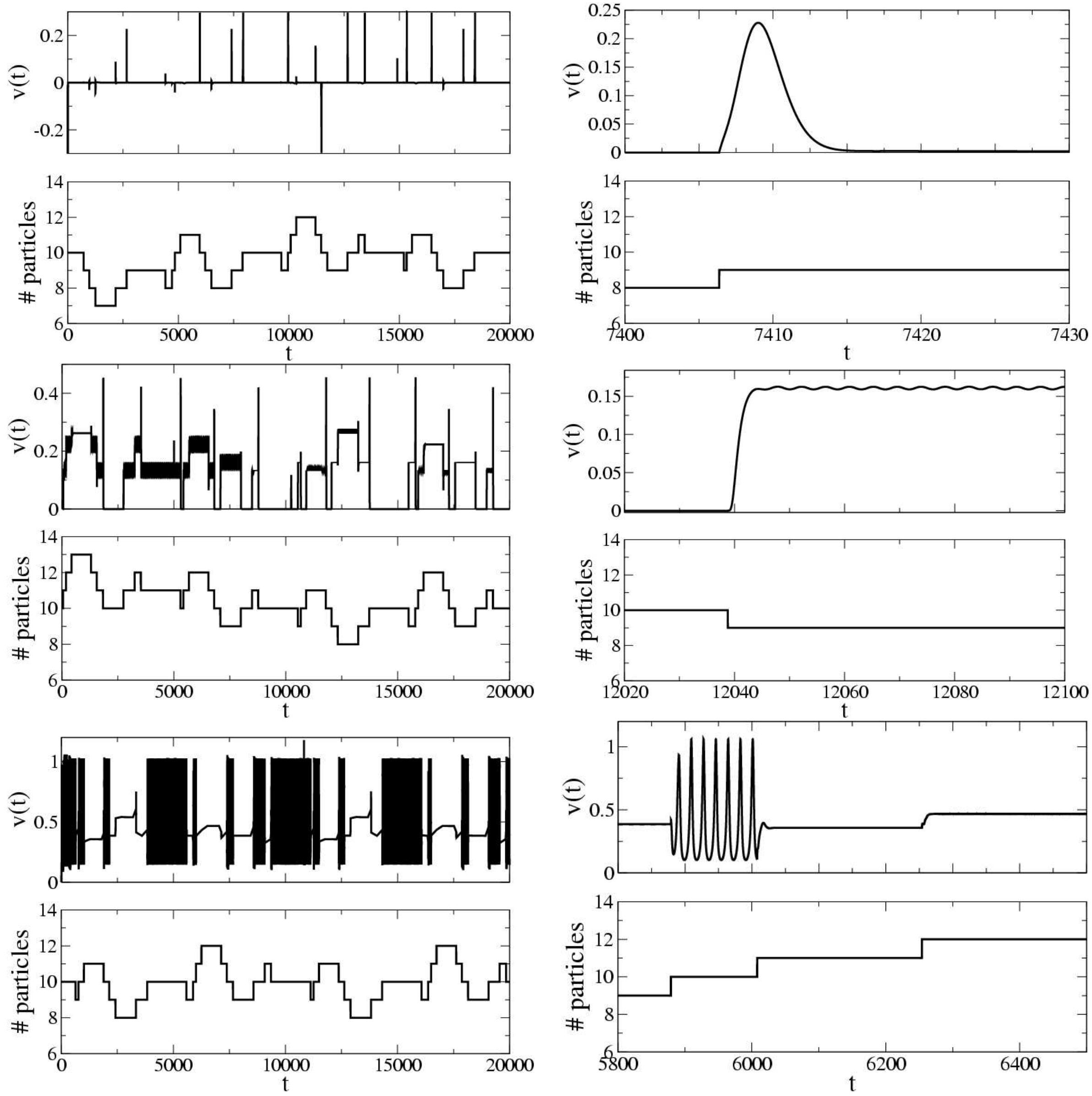

Figure 4.15: Velocity averaged over all particles and number of particles as a function of time in a small system. Here the system consists of 10 periods of the substrate with an initial condition of 10 particles, i.e. $\xi = 1$. This system size was chosen to compare with MD simulations. The forcing increases from top to bottom, $f = 0.0, 0.6, 1.2$ respectively. Other parameter values are $p = 0.001$, $\alpha = 0.0001$, $\eta = 2$ and $k = 1$.

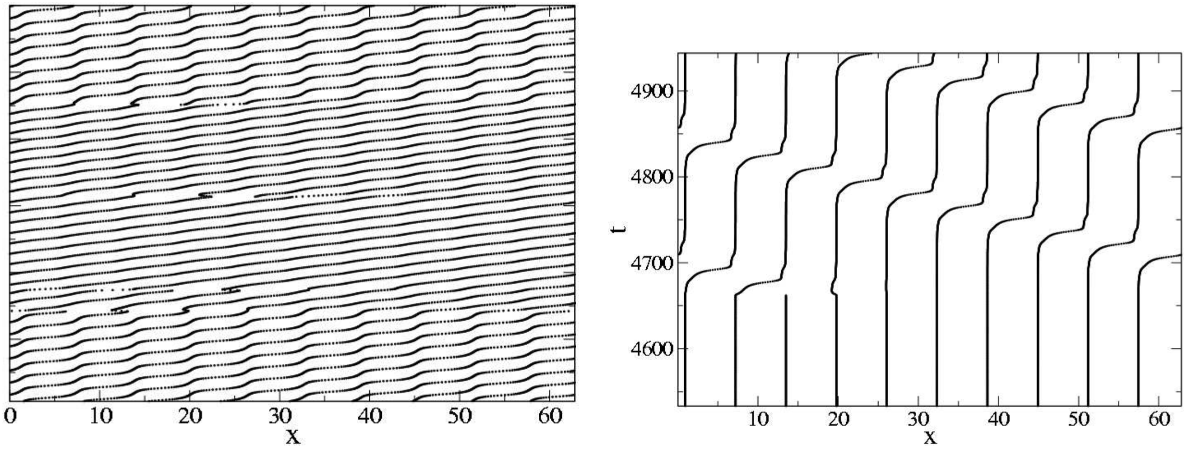

Figure 4.16: Left: The addition of a defect ($x = 18$) reduces the effective potential barrier and the resultant motion is smoother. Parameters are $f = 1.2$, $\eta = 2.0$, $k = 1.0$, $p = 0.001$ and $\alpha = 0.001$. Right: Close-up of defect motion. The defect motion can be discerned as a wave traveling from right to left after the addition of an excess particle. Parameters are $f = 0.8$, $\eta = 2.0$, $k = 0.1$, $p = 0.001$ and $\alpha = 0.001$.

the velocity. This is precisely the meaning of 4.67 and we expect it to be an accurate measure of slip in this regime.

For $f = 1.2$, i.e. beyond the SN bifurcation to bulk slip, two very distinct regimes can be seen, depending of the value of $d(t)$. For $d(t) = 0$ the chain of particles slides over the substrate as expected, resulting in a mean slip velocity with large oscillations (the oscillations have the largest amplitude nearest the SN, of course). Introduction of a defect pushes the system far from the critical slowing regime near the SN bifurcation and the motion is nearly free of oscillation (see lefthand panel of figure 4.16).

Space-time diagrams of the particle trajectories are compared to the corresponding averaged velocities in figure 4.17. The probability $p = 0.0001, 0.001, 0.01$ increases from top to bottom. The topmost panel clearly shows how slip is initiated if a particle is removed (particle removed at $x \sim 6$ and $t \sim 600$). The neighboring particles feel a sudden change in force and no longer sit in an equilibrium state. The upstream particle is pulled into the vacant well and the hole thus propagates upstream. Removal of a second particle ($x \sim 45$ and $t \sim 850$) increases the slip additively through the same mechanism.

The central panel illustrates the effect of introducing an extra particle, both in the case where this restores the defect-free state of the system $d(t) \to 0$ and in the case where a defect is created. Note at $t = 700$, $x \sim 5$ and $t = 850$, $x \sim 38$ the introduction of a particle halts the propagation of defects and leads to zero slip, while at $t = 950$, $x \sim 22$ a defect is introduced and motion once again begins. Dynamics in the lower panel appear quite disordered due to the high flux of particles. Nonetheless, the stereotypical events described above can still be clearly discerned as the building blocks of the resultant slip.

Figure 4.18 shows both slip velocties and particle trajectories for the case of weak inter-particle coupling ($k = 0.1$). The dynamics are qualitatively similar to the case described above, although of note are the large oscillations in the velocity of propagating defects. This comes as no surprise. The Peierls-Nabarro potential increases with decreasing inter-particle coupling strength. In figure 4.18 we are just past the SN bifurcation to defect motion (not to be confused with the SN bifurcation to bulk motion), which naturally leads to large oscillations in the propagation velocity.

Finally, in figure 4.19 we see that the prediction from 4.67 (red lines) captures the degree of slip well. One consequence of this is that for large enough inter-particle coupling (e.g. $k = 1$ here) the slip velocity increases almost linearly in the forcing (see figure 4.4, inset). This leads to a constant slip length as seen in the righthand panel of figure 4.19. Past the SN bifurcation point to bulk slip the curves all converge.

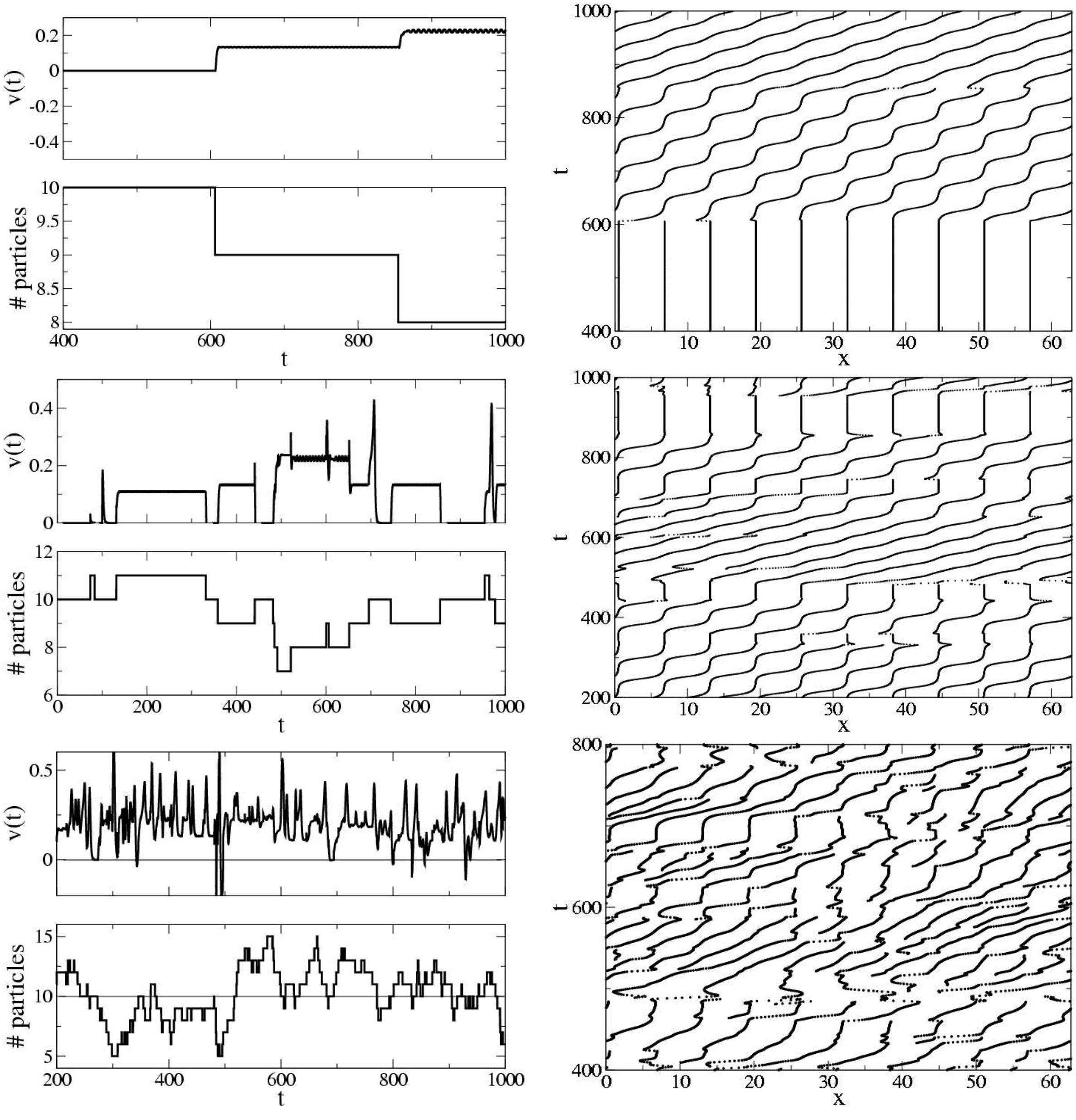

Figure 4.17: Velocity averaged over all particles and number of particles as a function of time (left) and corresponding space-time diagram (right) for three values of the particle flux, i.e. $p = 0.0001, 0.001, 0.01$ from top to bottom respectively. Other parameter values are as in figure 4.15 with $f = 0.5$. See text for a discussion.

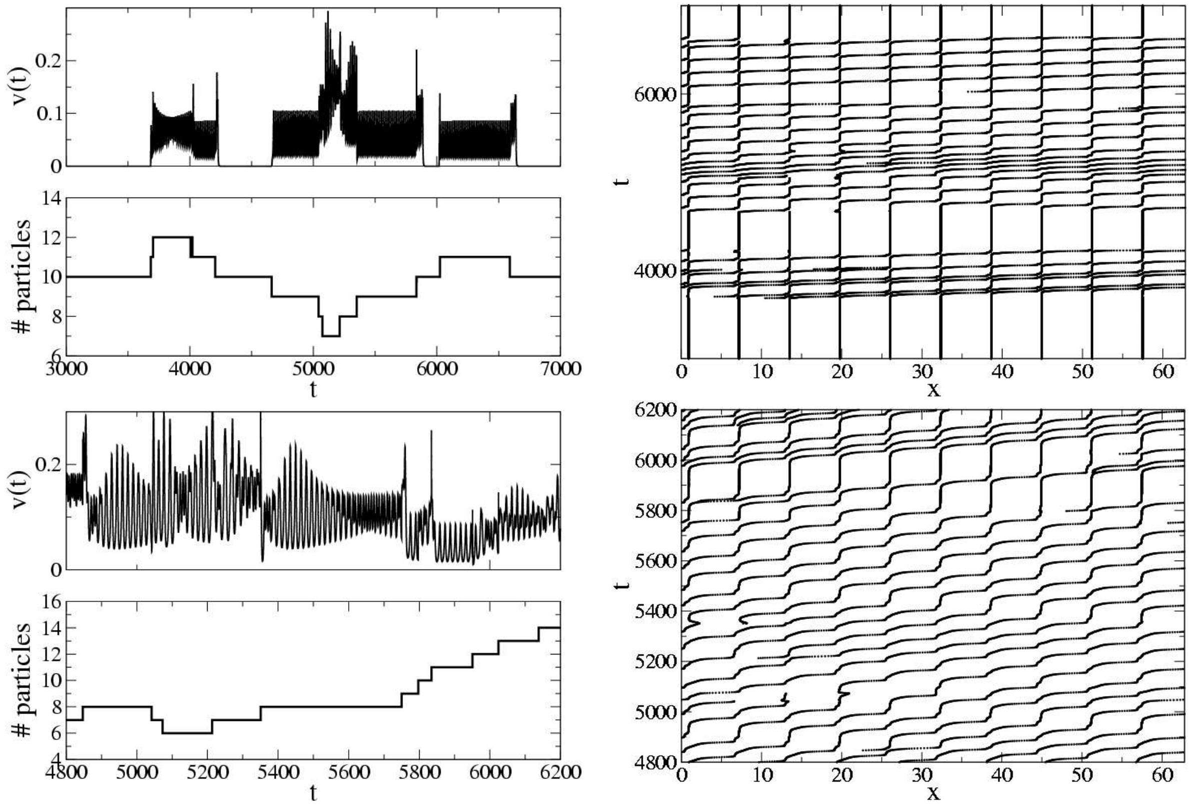

Figure 4.18: Case of weakly coupled particles, i.e. $\frac{k}{h}$ small. Left: Velocity averaged over all particles and number of particles as a function of time. Right: Space-time diagram of particle trajectories. Parameters are $f = 0.8$,$\eta = 2.0$,$\alpha = 0.001$,$k = 0.1$ and $p = 0.001$ (top), $p = 0.002$ (bottom).

However, for large enough flux the bifurcation itself is smeared out. The agreement between theory and simulation of the vdFK equation appears to be slightly less robust for weak coupling, perhaps due to the interaction of oscillatory modes generated by the defect motion near the SN bifurcation to defect-slip.

Figure 4.19 shows slip lengths of a fraction of a particle diameter, which is rather small. Reducing the effective friction between the liquid particles and the wall considerably increases slip length. Consider figure 4.20 where $\eta_{fs} = 0.1$, one tenth the

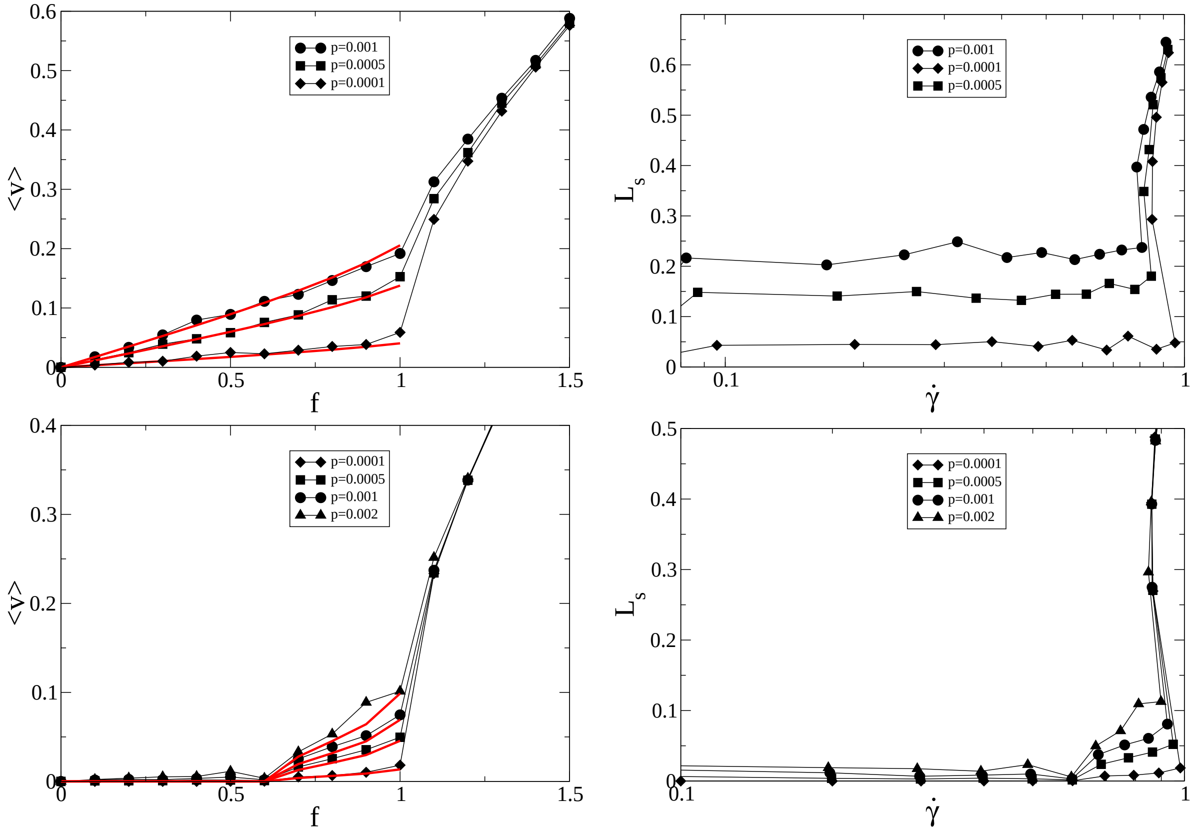

Figure 4.19: Slip velocity and slip length as a function of forcing for various values of p (see legend of each figure) with $\alpha = 0.001$ and $\eta = 2$. The equilibrium value of ξ is here 1. Top panels are for $k = 1$, bottom panels for $k = 0.1$. Red lines are the prediction from 4.67, symbols are numerical data and black lines are meant only as guides to the eye. Slip length is shown on lin-log scale to facilitate comparison with published data.

previous value. This leads to roughly a ten-fold increase in the slip length. Larger slip lengths can be obtained by further reducing the effective friction. Also note that 4.67 captures the degree of slip well (see red lines in figure 4.20) with the exception of $p = 0.01$, for which the particle flux is too high to consider the defects independent.

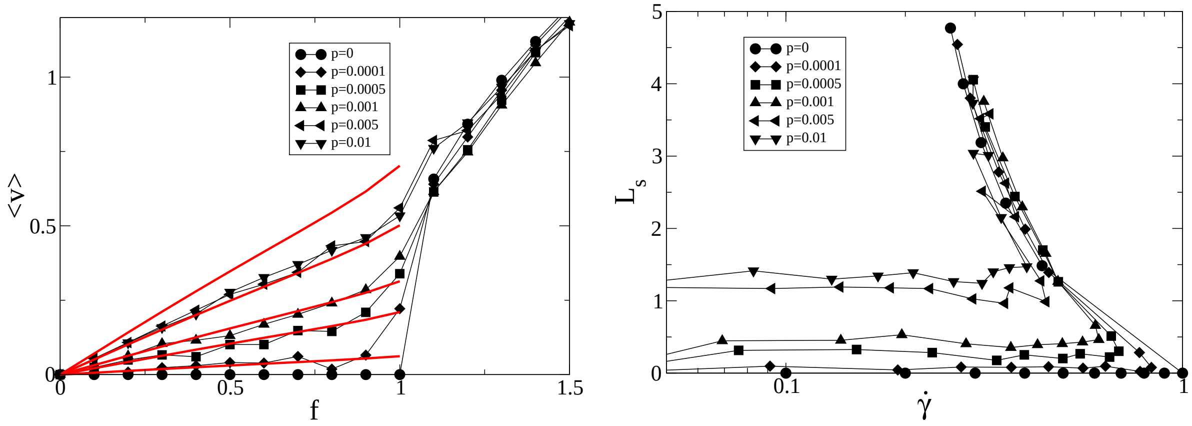

Figure 4.20: Slip velocity and slip length as a function of forcing for various values of p (see legend of each figure) with $\alpha = 0.001$ (except for $p = 0.005, 0.01$ for which $\alpha = 0.002$). Also $\eta = 1.1$, $\xi = 1$ and $k = 1$. Red lines are the prediction from 4.67, symbols are numerical data and black lines are meant only as a guide to the eye.

4.10 Conclusion

The vdFK model would seem to be a very fruitful approach in understanding the molecular-scale liquid dynamics at a solid interface. Considerable comparison with experimental and MD data should be undertaken to validate the theory and determine where it is a correct picture and where not.

Chapter 5

A Novel Interaction of Shaeffer Collateral and Temporo-Ammonic Inputs in a Model of a CA1 Pyramidal Cell

5.1 The SC and TA pathways

The *hippocampus* forms part of the primitive cortex of the brain and is involved in the formation of certain types of memory, expecially spatially-related memory [73]. The architecture of the hippocampus, as well as the diversity of cell types and their electrophysiological properties, have been intensively studied both in vitro and in vivo, especially in the rat [74].

According to the classical picture of hippocampal organization, the hippocampus

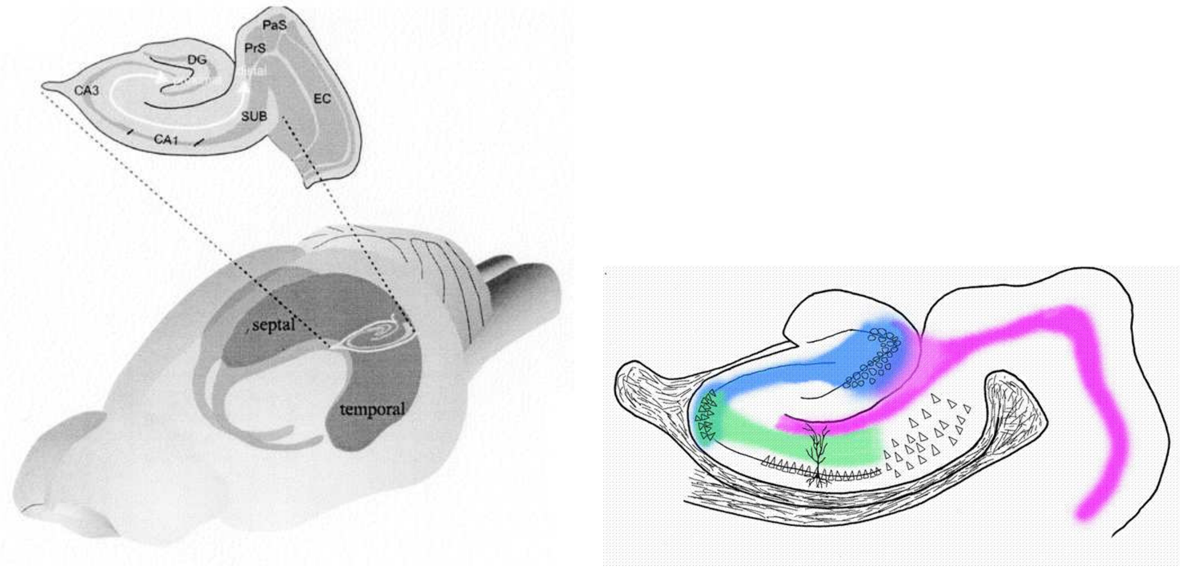

Figure 5.1: The rat hippocampus. The 'tri-synaptic' loop is highlighted on the right, including the two main excitatory inputs to CA1 pyramidal cells: the Temporo-Ammonic (TA) pathway (pink) and the Schaeffer Collaterals (SC) (green)

communicates with the cerebral cortex via the so-called 'trisynaptic circuit' (see figure 5.1). Input from the entorhinal cortex enters the hippocampus via the *perforant pathway*, which consists of two distinct sets of axons, one emanating from layer II and the other from layer III. Layer III axons (Temporo-Ammonic pathway (TA)) project directly to distal CA1 pyramidal cell dendrites in stratum lacunosum moleculare (SLM). The axons from layer II enter the dentate gyrus where they synapse onto dentate granule cells. Mossy fibers from the granule cells project to the CA3 region of the hippocampus, where a high degree of collateralization implies a highly nonlinear feedback process. CA3 pyramidal cell axons, called the Schaeffer Collaterals (SC), synapse onto apical dendrites of CA1 pyramidal cells in stratum radiatum (SR). Finally, CA1 pyramidal cells project back to the deeper layers of the entorhinal cortex, finishing the ‘loop’. The very small degree of collateralization in the CA1 region implies that the input-output relationship of CA1 pyramidal cells may to some extent be understood at a single-cell level. This neglects the very complex network of hippocampal interneurons [75].

The classical notion of the trisynaptic circuit is an oversimplification and many other projections to, from and within the hippocampus are known to exist [74]. Nonetheless, it is accurate to consider the SC and TA pathways to be the main excitatory inputs to CA1 pyramidal cells. Dynamical differences between the TA and SC pathways have very recently been investigated *in vivo* in guinea pigs [76] through extracellular recordings. The results show that the two pathways are selectively activated and thus dynamically distinct.

In this chapter we study the dynamical interaction of excitatory inputs from TA and SC pathways at the level of a single CA1 pyramidal cell through extensive simulations using NEURON. Our main result is a novel mechanism of coincidence detection involving the forward propagation of dendritic sodium-spikes (Na-spikes). Na-spikes generated in the apical tuft via the TA input, which generically do not cause somatic APs, may be ‘gated’ through to the soma if the main apical dendrite is sufficiently depolarized by SC input. The inputs must consequently also be sufficiently synchronous.

5.2 A model of a CA1 Pyramidal cell in NEURON

Three different pyramidal cell morphologies were used in simulations. [1] All three correspond to CA1 pyramidal cells of the rat hippocampus, reconstructed with the neurolucida microscope and converted into NEURON format. The three cells are referred to as ri04, ri05 and ri06 and are shown in figures 5.2, 5.3 and 5.4 respectively. Morphology can strongly affect the electrophysiological properties of neurons, including backpropagation of somatic APs and forward propagation of dendritic spikes [77]. We thus test three cells in order to determine to what extent our results are robust to morphological perturbations. The NEURON code for cell ri06, with the exception of the synapses, is the same as that used in [78].

The morphological data is in the form of a set of cartesian coordinates and associated diameters. NEURON then resconstructs the cell by joining together cylinders with given diameters (note the varying line thickness in figure 5.2, which reflects the recorded diameter, for example). The CA1 pyramidal-cell morphology can be subdivided naturally into distinct sections, both according to the nature of the inputs received as well as the electrophysiological properties of the neuron itself. In the present study, we distinguish between the following regions: soma, axon, basal dendrites, apical dendrites, and apical tuft. In addition, we also distinguish between the main apical dendrite and the oblique apical dendrites, which differ in the density of synaptic connections.

Table 5.1 shows the values of some passive cell properties. These values hold for all cell sections and all three cells unless otherwise noted. The variables are

---

[1] Morphological data for all three cells were obtained from the lab of Nelson Spruston.

C_m $(\mu F/cm^2)$	C_{my} $(\mu F/cm^2)$	R_m $(\Omega \cdot cm^2)$	R_a $(\Omega \cdot cm)$	V_{leak} (mV)
0.75	0.04	40000	200	-66

Table 5.1: Passive cell properties.

membrane capacitance (C_m), capacitance at the myelinated internodes of the axon (C_{my}), membrane resistance (R_m), axial resistance (R_a) and a leak reversal-potential (V_{leak}). The membrane capacitance also varies as a function of distance from the soma. The presence of spines in the more distal portion of the apical dendrites is modeled as an increased capacitance (by a factor of two) for all apical dendrites at a distance greater than $300\mu m$.

The ability of the cell to generate action potentials, as well as the active properties of the dendrites, depend on the presence of voltage-dependent ionic channels. The model used in this work includes four distinct currents: an inactivating sodium current, a delayed-rectifying potassium current and two additional A-type potassium currents, which activate at relatively low potentials. The A-currents activate and inactivate rapidly. NEURON models the ionic currents by solving the voltage-dependent differential equations for the fraction of open channels for each ionic species. The contribution, for example, of the sodium current at a given point in the cell is

$$I_{Na} = g_{\text{eff}}(V - E_{Na^+}) \tag{5.1}$$

$$g_{\text{eff}} = g_{Na} m^3 h \tag{5.2}$$

where the kinetic variables m and h, representing activation and inactivation respectively, are modeled via first-order equations with voltage-dependent time-constants and asymptotic values.

soma/basal	Na^+	K^+_{dr}	A-type K^+ (prox.)
g $(1/\Omega \cdot cm^2)$	0.048	0.040	0.048
E (mV)	55	-90	-90
axon			
g_{node}	30.0	0.040	0.0096
$g_{\text{internode}}$	0.048	0.040	0.0096
E	55	-90	-90
apical			
g	≥ 0.048	0.040	≥ 0.048
E	55	-90	-90

Table 5.2: Active cell properties by section. The parameters g_{node} and $g_{\text{internode}}$ are the conductances at and between the nodes of Ranvier respectively.

The values of the maximal conductances for each type of channel vary across the cell. Table 5.2 shows a characterization of the ionic channels broken down by section. Note, in particular, that the sodium and A-type potassium conductances vary spatially in the apical dendrites. Gradients in channel densities have been verified in experiment and used in simulations elsewhere previously [79]. Specifically, the sodium conductance varies as a function of the distance x from the soma as

$$\begin{aligned} g_{Na}(x) &= g_{Na}(1 + \alpha_{Na} \cdot x) \qquad x < x^*_{Na}, \\ g_{Na}(x) &= g_{Na}(1 + \alpha_{Na} \cdot x^*_{Na}) \quad x > x^*_{Na}, \qquad (5.3) \\ & \qquad (5.4) \end{aligned}$$

where α takes the value of 0 or 0.001, the latter being what we refer to as the 'strongly back-propagating' case. Unless noted otherwise, the default value of α will be 0. The value of x^*_{Na} is $500\mu m$. The potassium conductances vary as

$$\begin{aligned} g_K(x) &= g_K(1+\beta_p \cdot x) \qquad x < \tilde{x}, \\ g_K(x) &= g_K(1+\beta_d \cdot x) \qquad \tilde{x} < x < x^*_K, \\ g_K(x) &= g_K(1+\beta_d \cdot x^*_K) \quad x > x^*_K, \end{aligned} \tag{5.5}$$

where $\beta_p = \beta_d = 0.01$ (but can, in general, be different from one another) are the slopes of the conductance gradient for the proximal and distal potassium currents respectively. The values of $\tilde{x}$ and x^*_K are $100\mu m$ and $500\mu m$ respectively. These values correspond to those used in [79].

In addition to the passive and active properties described above, we place both excitatory (AMPA) and inhibitory (GABA) synapses on the cell. Experimental measurement of the density of synapses in CA1 pyramidal cells provides the estimates shown in table 5.3 [80]. Total numbers of synapses are around 30,000 of each type for each cell. Note that sub-sections of the apical dendrites labeled lower, mid- and upper correspond roughly to the first $150\mu m$, next $150\mu m$ and remaining distance (around $150\mu m$) to the apical tuft respectively. Both excitatory and inhibitory synapses are modeled as double-exponential synapses (point-process Exp2Syn with NetCon in NEURON). Synaptic properties are given in table 5.4. Note that the maximum synaptic conductance is 100 pico-Siemens (pS) in each case. Empirical data indicate that activation of a synapse recruits between 10 and 100 channels, each of which contribute around 10 pS conductance change with an average around 35. Thus our choice is at the lower end of synaptic strength. As such, the activation of 100 synapses in this work may be equivalent to the activation of anywhere between 10

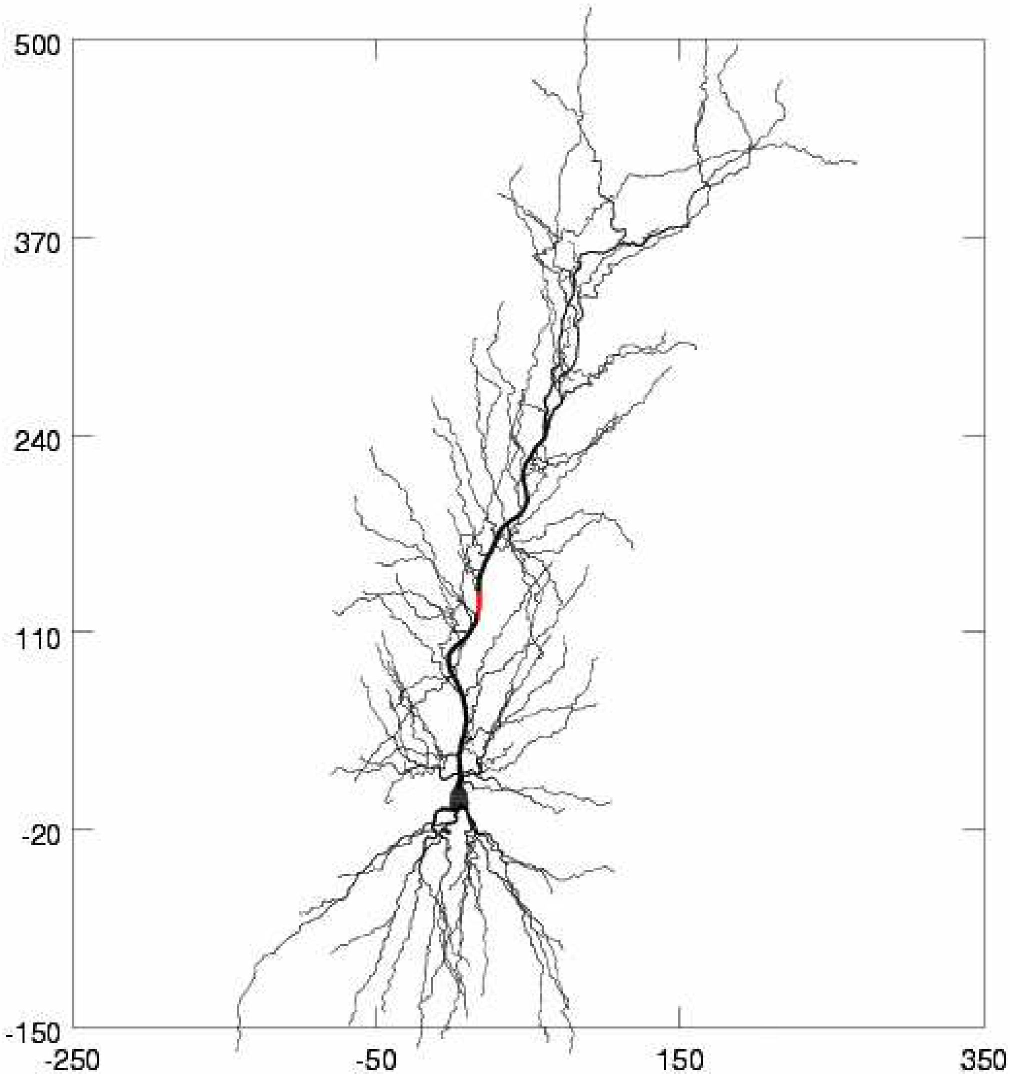

Figure 5.2: Pyramidal cell ri04. Axes indicate distance in microns from the soma.

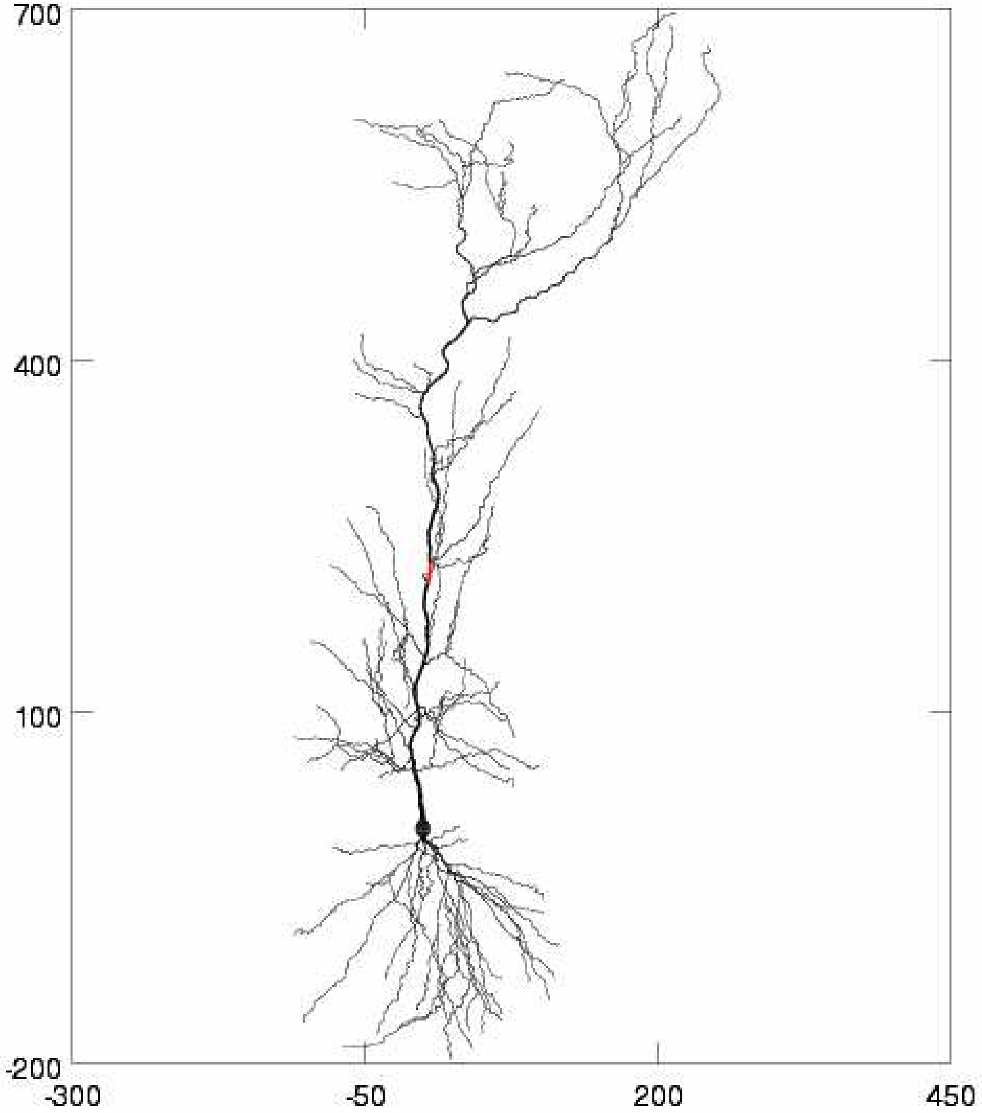

Figure 5.3: Pyramidal cell ri05. Axes indicate distance in microns from the soma.

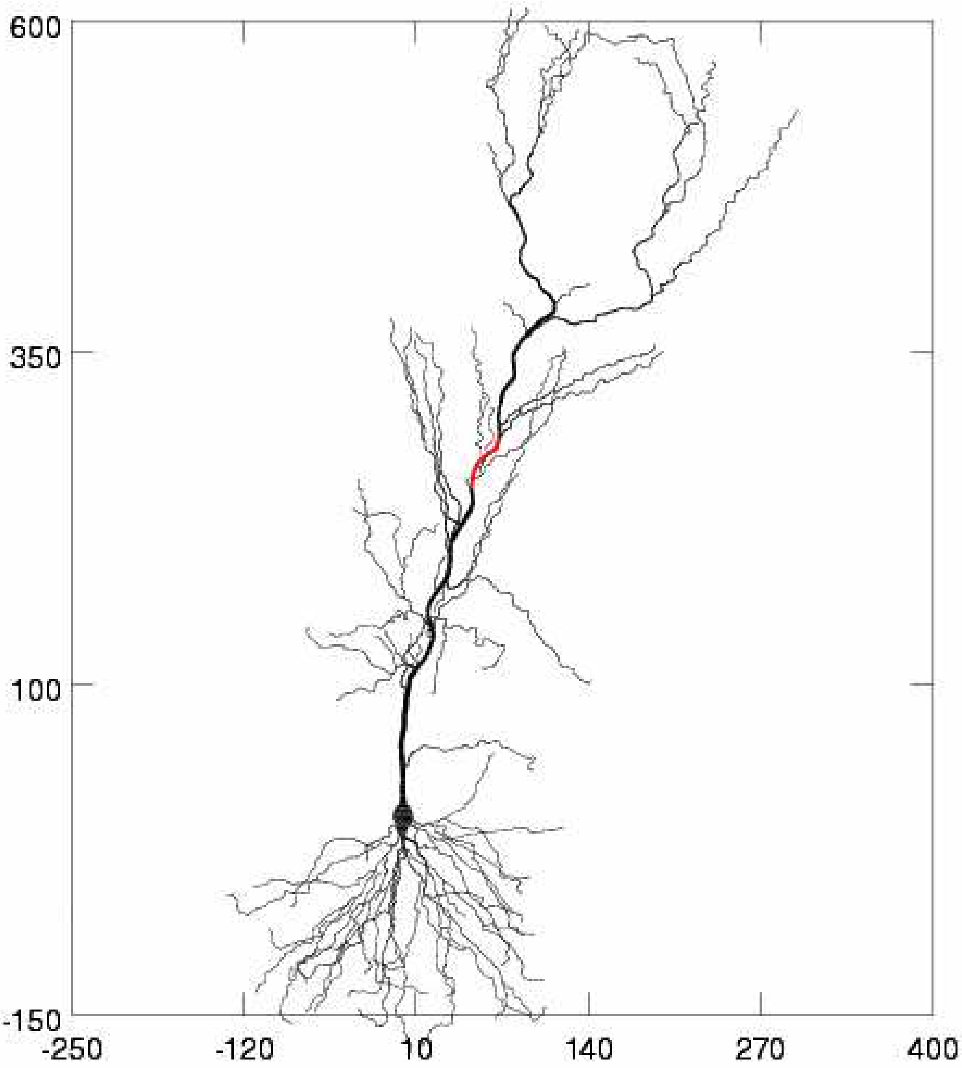

Figure 5.4: Pyramidal cell ri06. Axes indicate distance in microns from the soma.

	AMPA	GABA	ri04		ri05		ri06	
soma	0.0	150	0	2381	0	2362	0	3935
basal	2.5	2.2	8782	7721	8836	7773	10287	9048
apical (lower main)	0.05	15	1	1691	2	1537	4	1590
apical (mid main)	0.5	8.0	60	1068	66	1092	65	1128
apical (upper main)	7.0	5.0	961	686	1633	1165	1246	889
apical (obliques)	3.0	2.0						
lower			5613	3737	4676	3116	2712	1354
mid			7390	4921	5627	3748	7598	3795
upper			3237	2155	1883	1254	3595	1793
apical (tuft)	1.5	3.0	2204	4413	3934	7887	3004	6015

Table 5.3: Synaptic densities. The first two columns give approximate densities in units of synapses/μm from experimental measurement. The remaining columns give the number of synapses for each model cell, excitatory followed by inhibitory for each one.

	AMPA	GABA
τ_{rise}(ms)	0.2	1.0
τ_{fall}(ms)	2.0	18.0
E_{rev}	0.0	-100
g_{syn} (pS)	100	100

Table 5.4: Synaptic properties.

and 100 synapses in a real CA1 pyramidal cell.

Experimental techniques, in which a large number of afferent axons are stimulated with an electrode, can be mimicked in simulations by activating certain populations of synapses. Thus, controlled in-vitro protocols in which various stimuli are applied via different pathways, are easily investigated in simulation. In addition, in-vivo conditions in which pyramidal cells are subject to a seemingly stochastic background noise due to a large number of uncorrelated inputs, are also easily reproduced. In both cases, diagnostics can be taken at any time and at any location in the cell (and without experimentally related uncertainty), an obvious advantage.

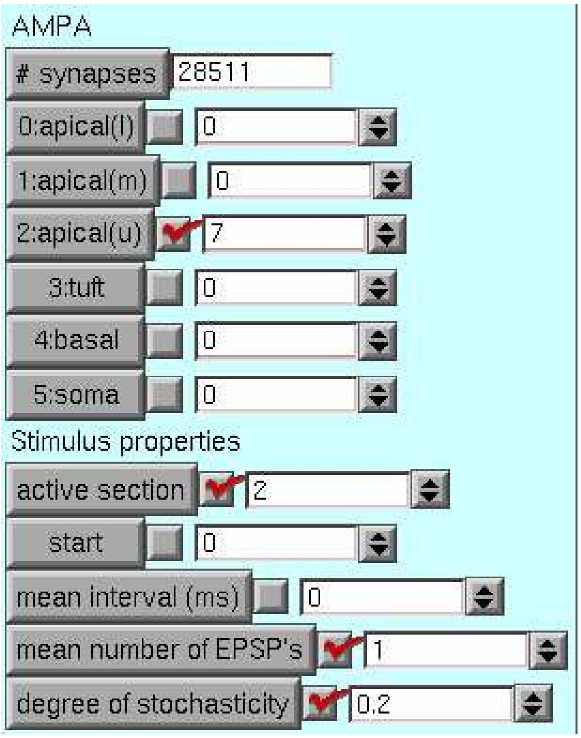

AMPA
synapses 28511
0:apical(l) ☐ 0
1:apical(m) ☐ 0
2:apical(u) ☑ 7
3:tuft ☐ 0
4:basal ☐ 0
5:soma ☐ 0
Stimulus properties
active section ☑ 2
start ☐ 0
mean interval (ms) ☐ 0
mean number of EPSP's ☑ 1
degree of stochasticity ☑ 0.2

Figure 5.5: Part of the graphical user interface (gui) controlling the stimulus properties.

Figure 5.5 shows part of the graphical user interface (gui) designed to facilitate the control of the synaptic stimulus (here for AMPA). The cell is divided into 5 sections for which the percentage of active synapses can be chosen. In figure 5.5, seven percent of the synapses located in the upper apical dendrites (including oblique apical dendrites) are active. Once a section is activated, the stimulus properties can be set, including the start time of stimulus, average inter-spike-interval (ISI), average number of spikes and ‘degree of stochasticity’. This last parameter interpolates between a periodic and a Poisson train of EPSCs as it varies from 0 to 1.

5.3 Response to single inputs

In order to investigate the response of our model pyramidal cells to paired SC and TA inputs, we must first characterize their dynamics in response to single inputs. CA1 pyramidal cells have a very extensive dendritic arbor, penetrating into stratum oriens and the alveus (basal dendrites) as well as all the way through stratum radiatum (SR) and into stratum lacunosum moleculare (SLM). Distal inputs from the SLM may be as far away from the cell body as $700\mu m$. Passive attenuation will make such an input much less effective in eliciting an action potential than an identical input nearer the soma. However, active dendritic properties including the generation of dendritic spikes, may complicate this picture and lead to the cell acting as a highly non-linear integrator.

Figure 5.6 shows the average peak depolarization (100 trials) at three points in the cell $ri04$ for four different stimuli. The stimuli are to the lower-apical, mid-apical, upper-apical and apical tuft, left to right, top to bottom respectively. The three 'recording electrodes' are indicated by black circles (soma), red squares (main-apical dendrite $\sim 250\mu m$) and blue diamonds (apical tuft $\sim 700\mu m$). The standard deviation of the 100 trials is given by error bars.

It is clear that the likelihood of generating an action potential (AP) decreases as the locus of the stimulation moves further and further from the soma. Consider, for example, that activation of a mere 2% of the synapses in the lower apical region (about 112 synapses from 5.3) is sufficient to very reliably elicit APs, while stimulation of the mid-apical region requires 3% (240 synapses) and this increases to 11% for upper-apical stimulation (over 400 synapses). Finally, stimulation of the tuft never causes

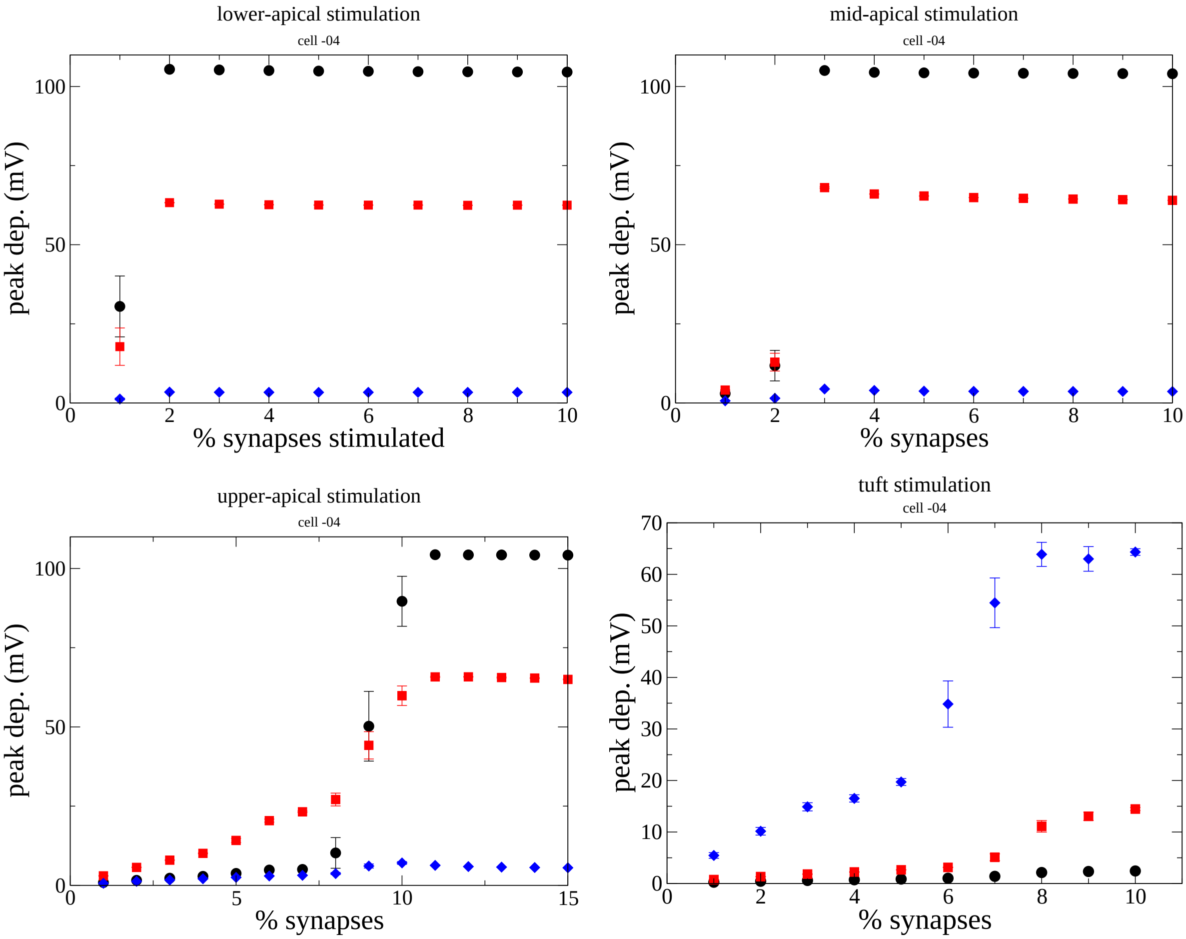

Figure 5.6: Response properties of the cell ri04. Voltages were recorded from the soma (black circles), the main apical dendrite (red squares) and the apical tuft (blue diamonds).

an AP. Note that the large depolarization in the main-apical dendrite (red squares) whenever APs occur is the signature of reliable backpropagation of the AP. That is, whenever an AP occurs in the axon, it not only travels down the axon itself, but also propagates backwards into the dendritic arbor via the activation of Na channels in the membrane of the dendrites. This process is ubiquitous in pyramidal cells of both the hippocampus and the cerebral cortex [81].

Interestingly, while for sufficiently small stimuli in the tuft (lower right-hand panel) the resulting local integration of EPSPs appears to be more or less linear as a function of stimulus intensity (and thus passive), larger stimuli ($> 5\%$) readily elicit variable-amplitude, nonlinear events. Thus dendritic Na-spikes occur locally in the tuft but fail to initiate an AP at the soma. In fact, the attenuation of the dendritic spikes is so great that their influence is hardly felt at the soma (see black circles in same panel).

It was shown in [78] that the experimentally observed dichotomy in the efficacy of backpropagation in CA1 pyramidal cells can be explained by a slight gradient in the density of Na channels in the apical dendrites. Those neurons which exhibit this positive gradient in the channel density are referred to as strong-backpropagating (SBP) neurons. Figure 5.7 shows data analogous to that in figure 5.6 for the SBP case. Note the two principal differences. Firstly, whenever an AP occurs, the back-propagation consistently reaches the apical tuft resulting in a large depolarization (blue diamonds). Secondly, Na-spikes generated locally in the tuft now sometimes do elicit somatic APs (lower right-hand panel).

Figures 5.8 through 5.11 show analogous data for the other two cells, both for the standard and SBP cases. Note the qualitative similarity for all three cells despite

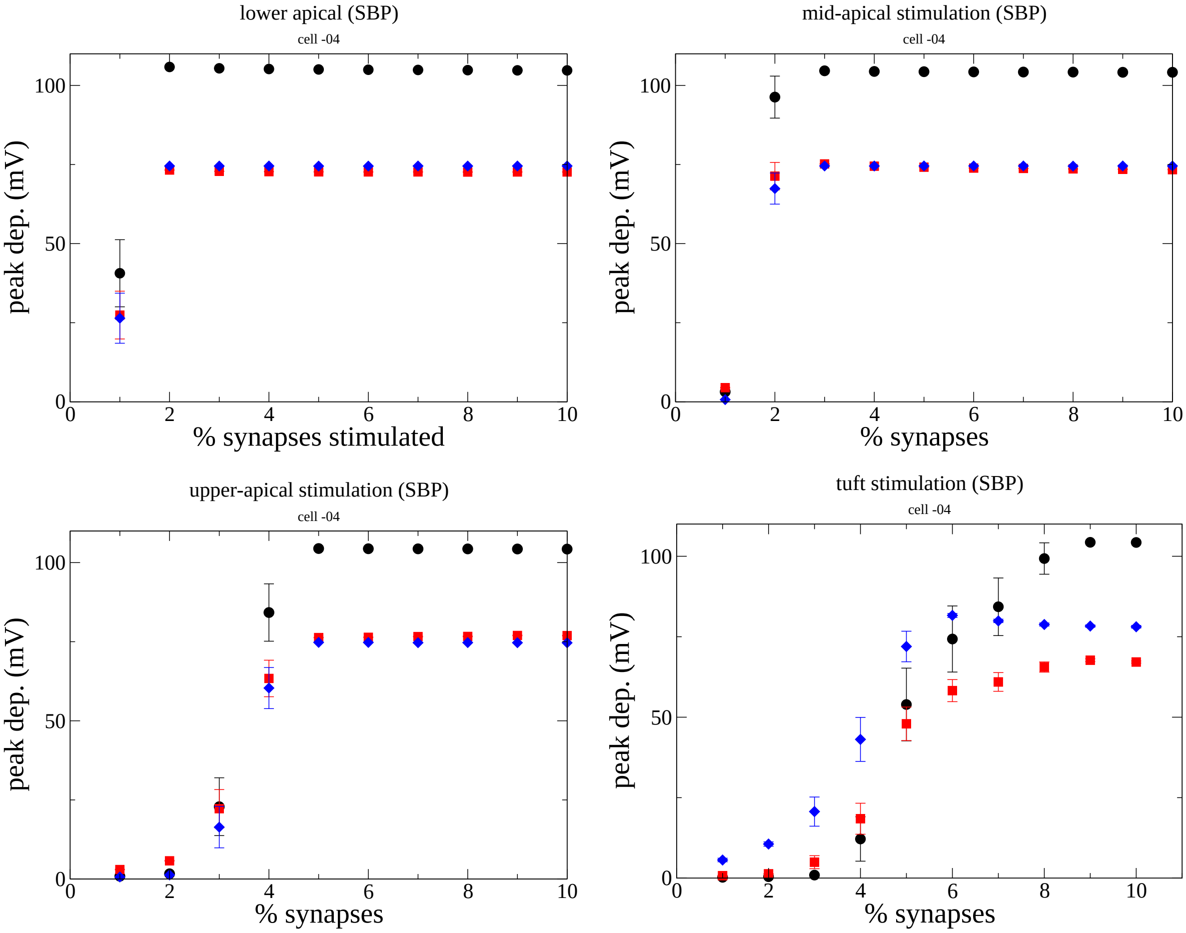

Figure 5.7: Response properties of the cell ri04 for the strongly back-propagating case.

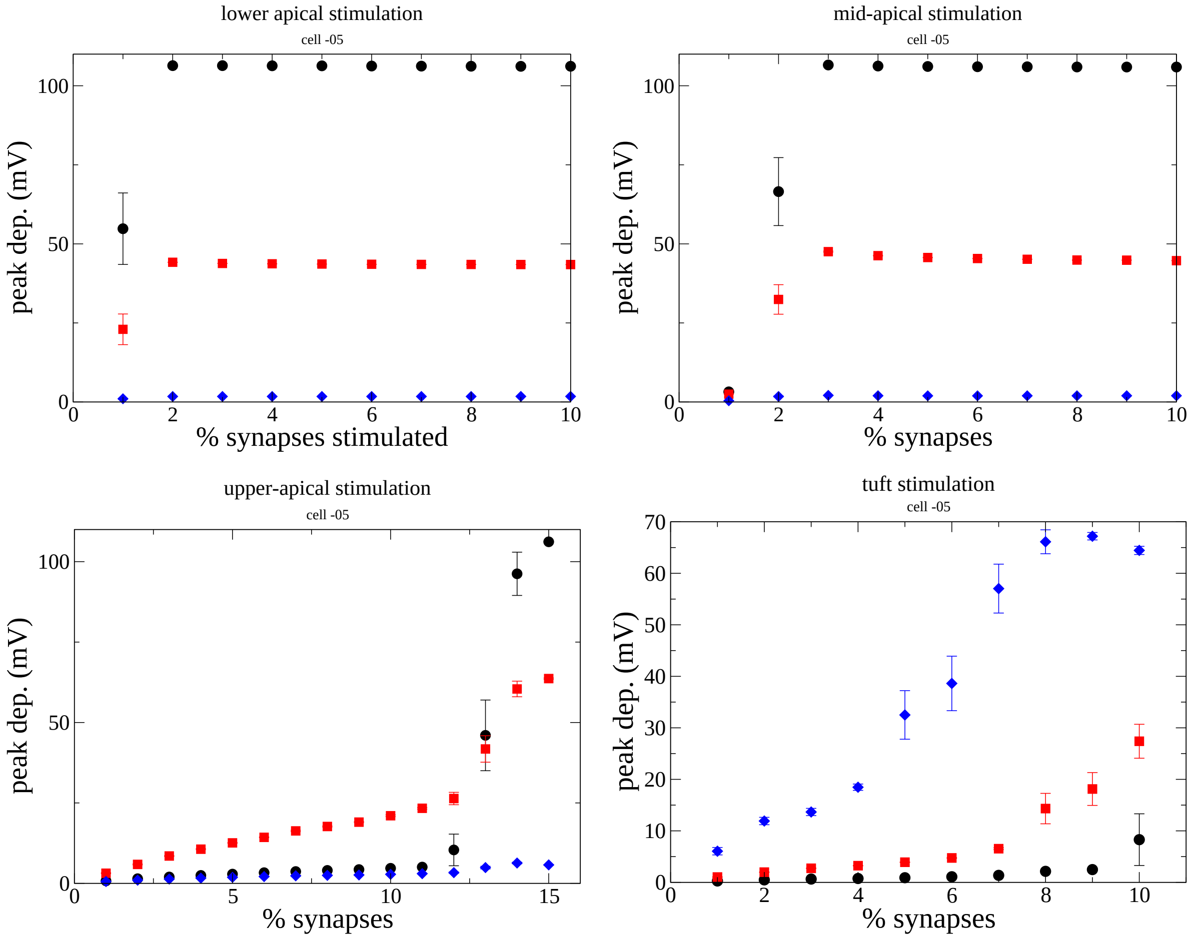

Figure 5.8: Response properties of the cell ri05.

the quite different morphologies. The above discussion is, in short, valid for all three cells and we can be relatively secure that results obtained from any one of these three cells will be more generally true. At the very least we can state that the reliable generation of Na-spikes in the apical tuft, which seldom if ever elicit a somatic AP (in the non-SBP case), is robust to morphological perturbations. It appears to be a property common to all three cells.

A passive model of a spatially extended neuron, in which sodium channels are

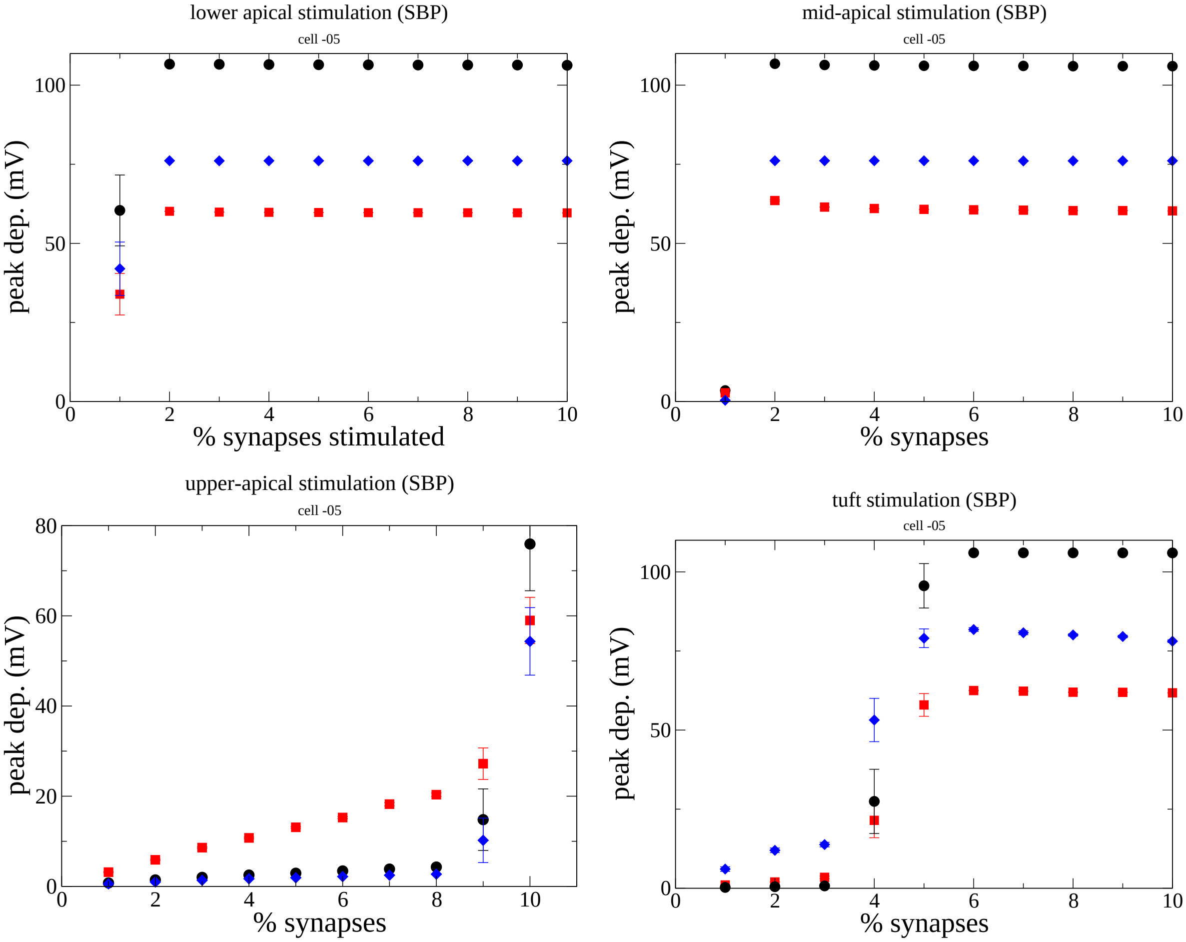

Figure 5.9: Response properties of the cell ri05 for the strongly back-propagating case.

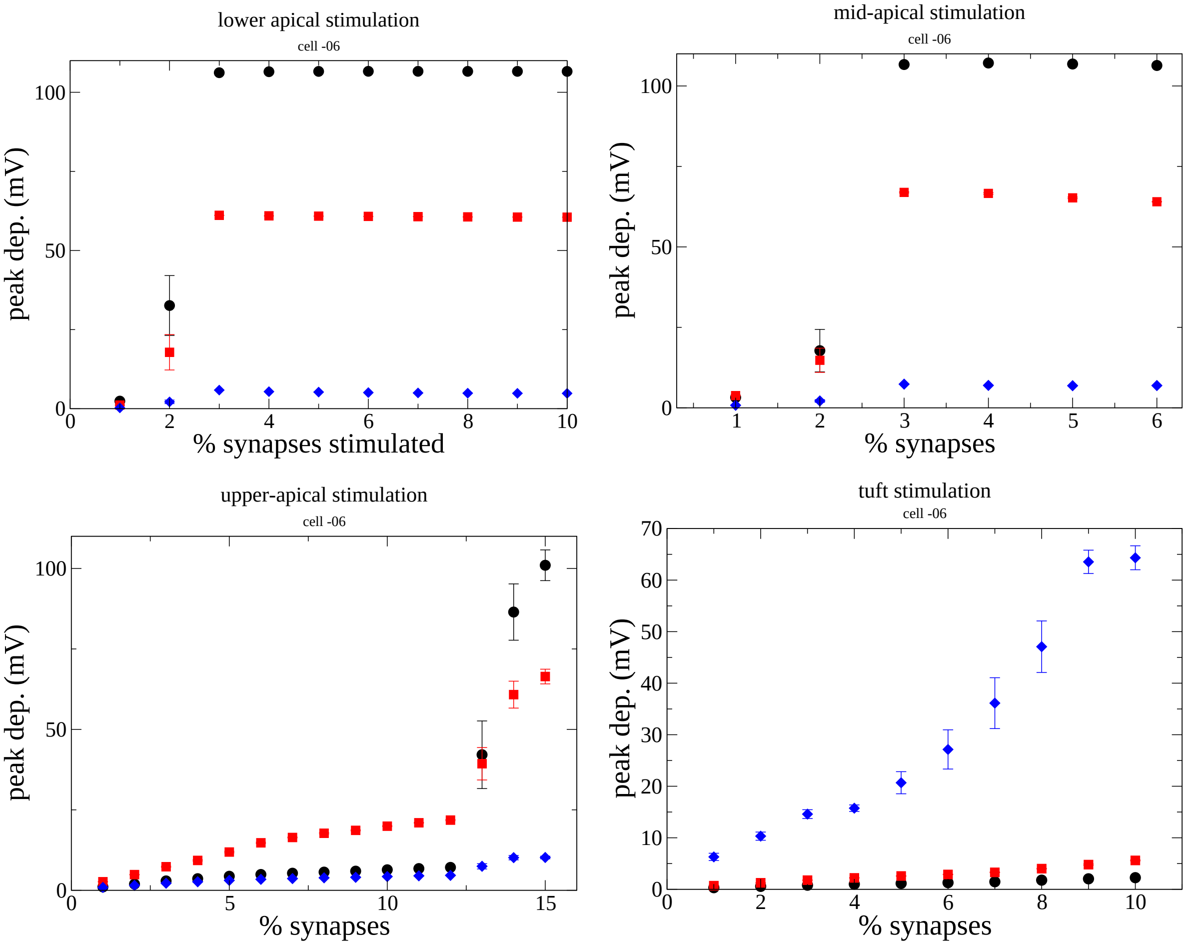

Figure 5.10: Response properties of the cell ri06.

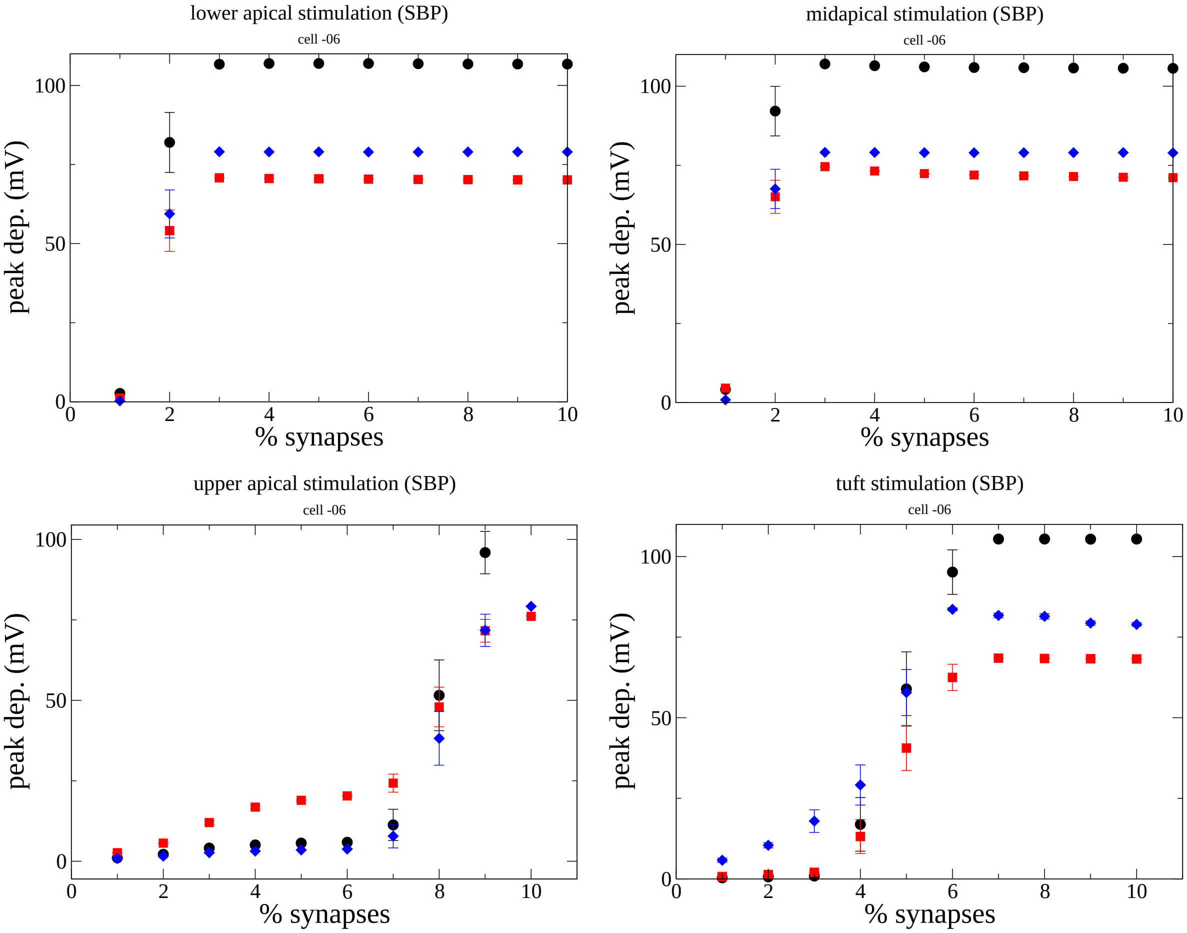

Figure 5.11: Response properties of the cell ri06 for the strongly back-propagating case.

removed from the dendrites (but not the soma or axon), would predict that more distant stimuli would be less likely to elicit a somatic AP than a proximal one of the same amplitude. The further away an EPSP occurs from the soma, the more attenuation there will be at the soma and thus a greater absolute stimulus intensity is needed for an AP. This notion is consistent with much of the data seen in figures 5.6 through 5.11. However, a close look at the initial site of spike generation reveals that the picture of passive attenuation (diffusion) and integration is not sufficient to understand the data.

Figure 5.12 shows the timing difference between the time of peak depolarization measured both at the soma and along the main-apical dendrite as a function of stimulus intensity for four different stimuli (lower-, mid- and upper apical and tuft). Data are shown only for those trials where an AP occured. Consider the case where this difference is negative (t(AP)-t(spike)$<$ 0). This means the time of the peak depolarization at the soma (due to the AP) occurs before the time of the peak depolarization in the dendrite (due to the backpropagating AP). The AP thus clearly occured first in the soma and propagated backwards. In the opposite case a spike must have been generated in the dendrite first and propagated to the soma, thereby eliciting a somatic spike. Where the timing difference is exactly zero both a somatic AP and a dendritic spike occured simultaneously!

Consider cell ri06 (lower left-hand panel). A proximal stimulus (lower-apical, black circles) always results in a somatic AP first. This is consistent with the notion that very proximal EPSPs diffuse without appreciable attenuation to the soma. Activating synapses in the mid-apical region (red squares) can cause APs both through passive diffusion and the propagation of dendritic spikes as this data straddles the line of

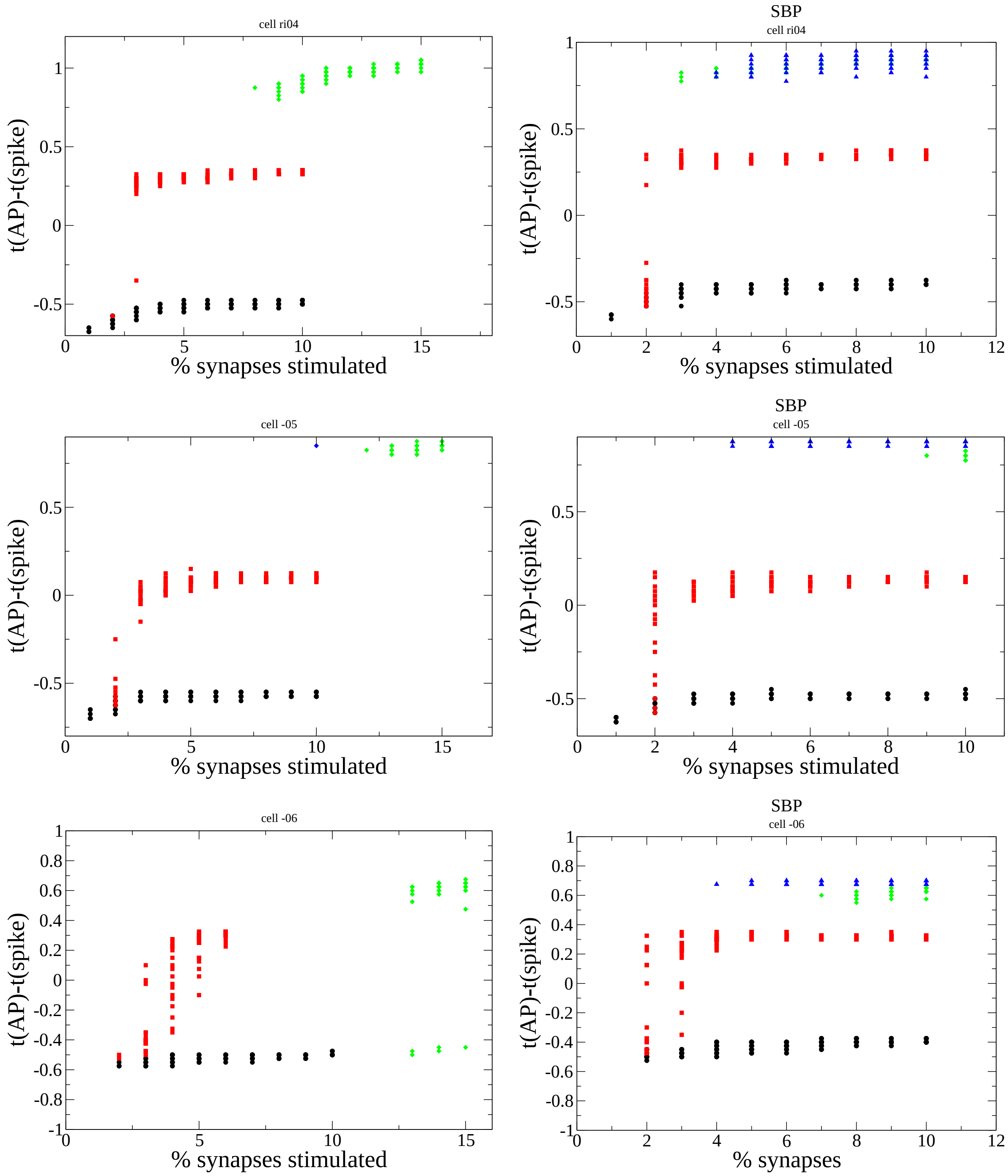

Figure 5.12: Data showing the dichotomy of action potential generation via passive integration and forward propagation of dendritic spikes. A negative timing-difference indicates that an AP was generated first, while a positive difference means a dendritic spike propagated to the soma and caused an AP. Colors correspond to the region of the apical dendritic tree to which the stimulus was applied: lower apicals (black), mid-apicals (red), upper apicals (green) and tuft (blue).

zero timing difference. Finally, a more distal stimulus (upper-apical) will always cause denditic spikes first. Intracellular recordings from CA1 pyramidal cells in vitro have revealed similar qualitative behavior in real cells [82].

5.4 Paired SC and TA inputs

We have now laid the groundwork for an investigation of the interaction between inputs via the two principal excitatory pathways to CA1 pyramidal cells. In particular, we have examined the response of three morphologically distinct pyramidal cells to stimuli focused at different points along the apical dendritic tree. We have seen that the distal-most inputs, those which are reasonably interpreted as occuring within SLM and thus from the TA pathway, reliably cause local Na-spikes, which however fail to significantly influence the potential at the soma. This is in stark constrast to a stimulus via the SC, which may cause action potentials through passive diffusion of EPSPs or propagation of dendritic spikes.

What is the role of the TA input if it is unlikely to affect the soma? How does the cell make use of the information it receives from these two pathways? In other words what is the input-output relationship? It has recently been documented experimentally that combining these two stimuli results in an enhanced efficacy of AP generation [83], but the mechanism remains unclear. It seems logical that two subthreshold stimuli may summate to provide sufficient depolarization at the soma for AP generation. Nevertheless we show in this section that an active, highly non-linear process is much more likely behind this increased efficacy. We compare simulations of a passive model in which summating inputs only marginally improve the likelihood of AP generation, with the above-studied active model where a very significant increase in AP generation is obtained by combining two subthreshold inputs. In this paradigm, a small, subthreshold depolarization via the SC is sufficient to 'gate' TA-generated dendritic Na-spikes in the tuft, allowing them to propagate to the soma thereby eliciting a somatic AP. The efficacy of the gating is furthermore dependent on the relative timing of the two inputs.

In order to differentiate between those cell responses that are due to passive properties from those that are a consequence of active (voltage-dependent) dendritic currents, we remove the Na channels from the dendrites of our simulation of cell ri06. Figure 5.13 shows data from representative trials in such a passive model, both for SC and TA inputs. The upper panels display the maximum voltage during each run as a function of distance x from the soma, while the bottom panels show traces of voltage as a function of time. Note the almost complete absence of backpropagation of AP's for the SC input.

Figure 5.14 shows analogous data for the active case (with Na channels intact in the dendrites). Here, for sufficiently large TA stimuli dendritic spikes are generated, which however do not propagate to the soma.

We now investigate the effect of pairing syncronous SC and TA inputs, both for the active and passive cases. Here we take a fixed TA stimulus (8%) while varying the SC stimulus intensity. Figure 5.15 shows data from the paired (simultaneous inputs) and unpaired protocols, with the active case in red and the passive case in black. Plotted is the probability of a somatic AP (100 trials).

While it is not at all surprising that a greater stimulus intensity is needed to generate AP's in the passive case, it is striking that the likelihood of AP generation

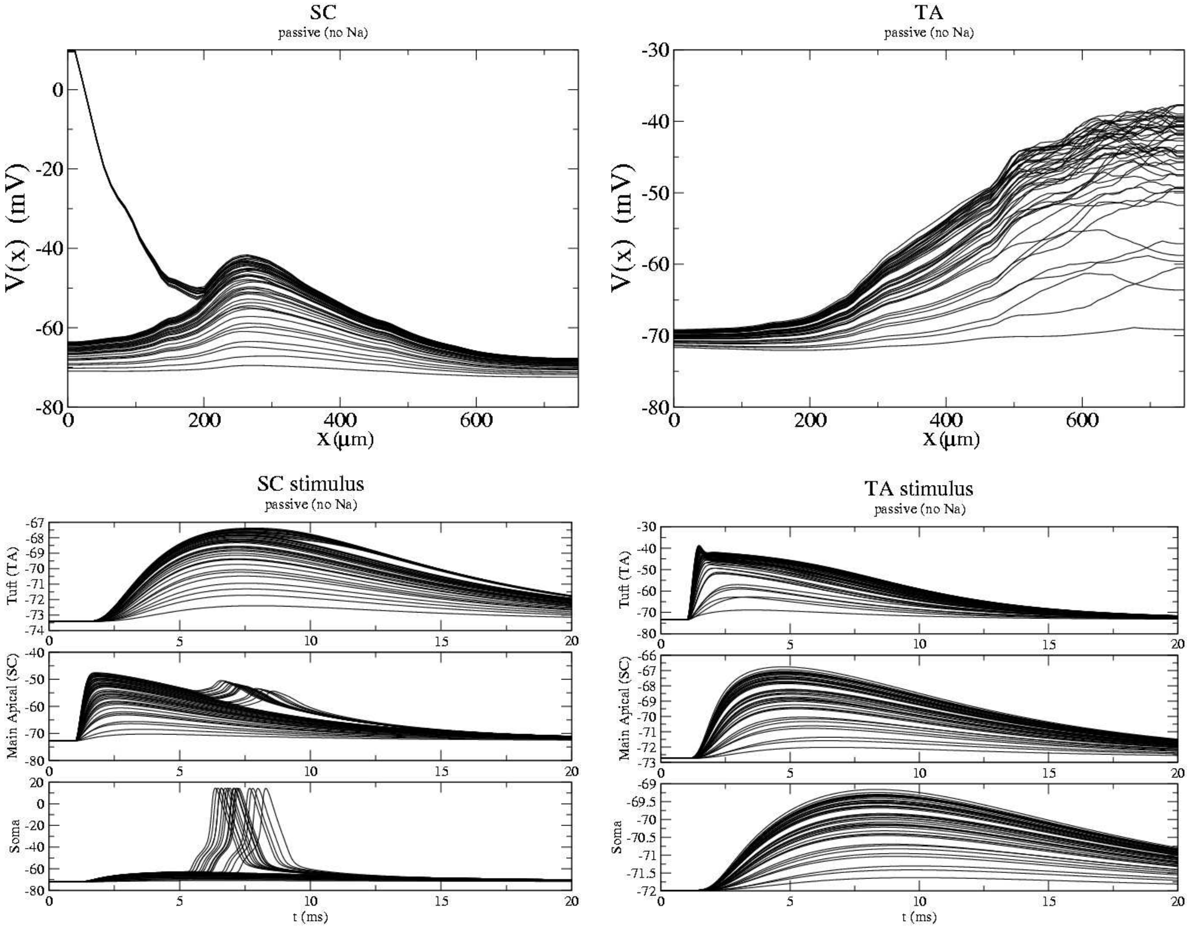

Figure 5.13: Response of cell ri06 to SC and TA inputs in a passive model.

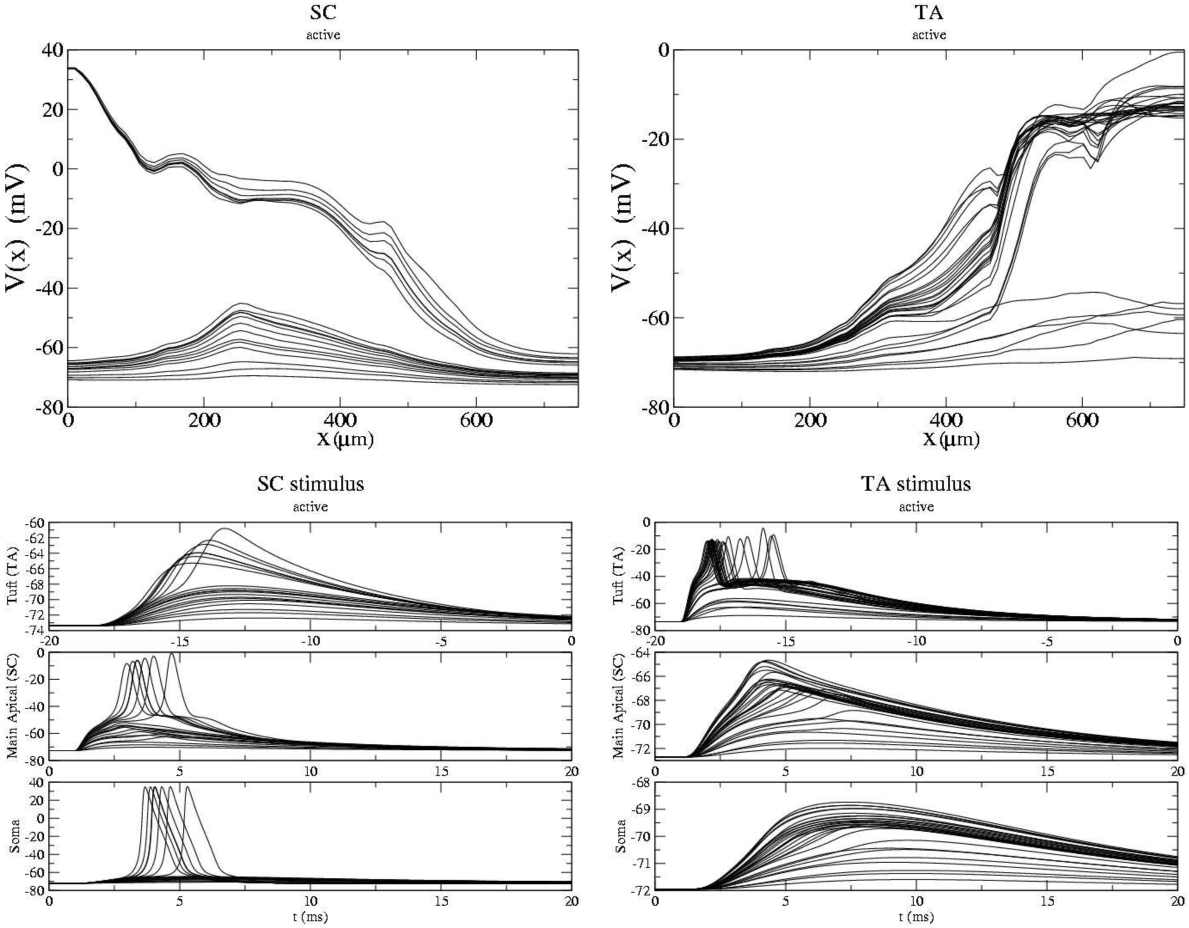

Figure 5.14: Response of cell ri06 to SC and TA inputs in an active model.

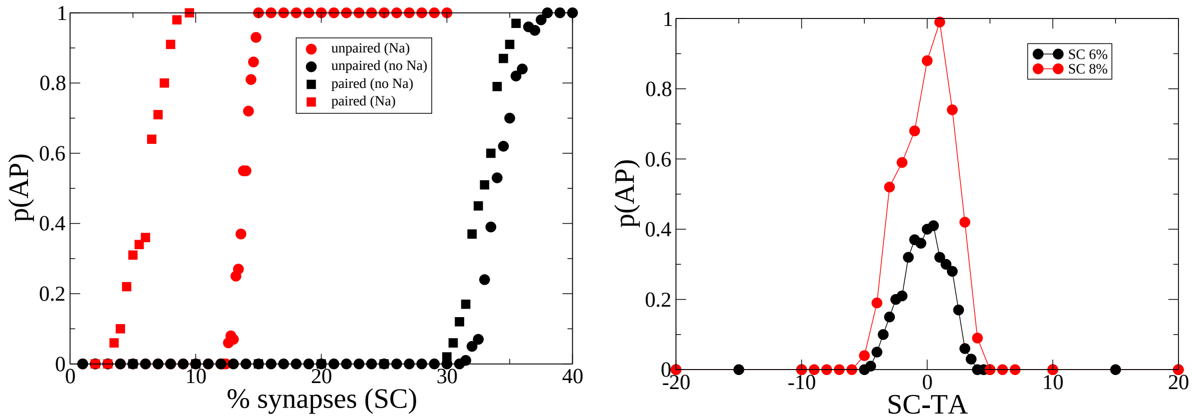

Figure 5.15: Response of cell ri06 to paired inputs. Left: Shift in the probability of eliciting an action potential due to pairing the inputs. Note the considerable shift in the active case in constrast to the passive case. Right: Probability of eliciting an action potential as a function of the timing difference in ms between the two stimuli. The function is more or less peaked around the synchronous-pairing protocol.

is nearly unaffected by pairing the stimuli in the passive case, while the curve is significantly shifted to the left in the active case. Note the greater than 50% reduction in the threshold for AP generation in the active case. Comparison with the passive case clearly shows this is not due to linear summation of the inputs.

Figure 5.17 provides an illustration of the mechanism underlying the increased efficacy of AP generation for paired SC-TA inputs. The traces in the top two panels correspond to the recording set-up shown in figure 5.16. This particular arrangement was chosen to maximize the resolution around the primary apical bifurcation, essentially the ‘gateway’ between the apical tuft and the main apical dendrite. Thus we observe the voltage just above, just below and right at the bifurcation as well as in the tuft, along the main apical dendrite and at the soma.

Consider the left-hand side of figure 5.17, for which the TA and SC stimuli are

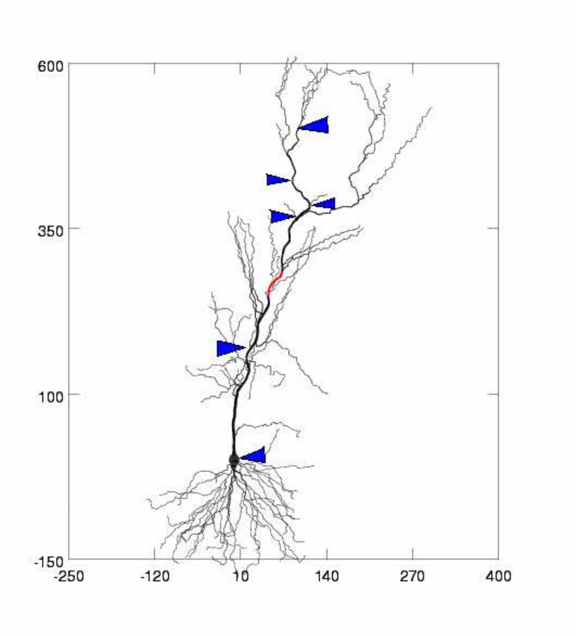

Figure 5.16: The recording configuration for results shown in figure 5.17.

8% and 6.5% respectively. The second through fourth traces (at the bifurcation) clearly show a depolarization beginning at 1ms atop of which there is even a small active event (see bottom three traces, a blow-up). This depolarization is, however, independent of the TA-driven Na-spike in the tuft. In fact, an artifact of the Na-spike is visible in the second trace (see top trace of bottom panel) although it occurs several ms after the intial, presumably SC-dependent depolarization. The amplitude of the TA-driven spike thus attenuates considerably, and the SC stimulus is not sufficient to elicit a somatic AP.

The right-hand side of figure 5.17 is for an identical simulation with a change only in the amplitude of the SC stimulus (now 6.6%). The SC stimulus is now sufficiently large to 'gate' the Na-spike through the primary apical bifurcation and to the soma. Specifically, the small-amplitude remnant of the Na-spike in the second trace of the

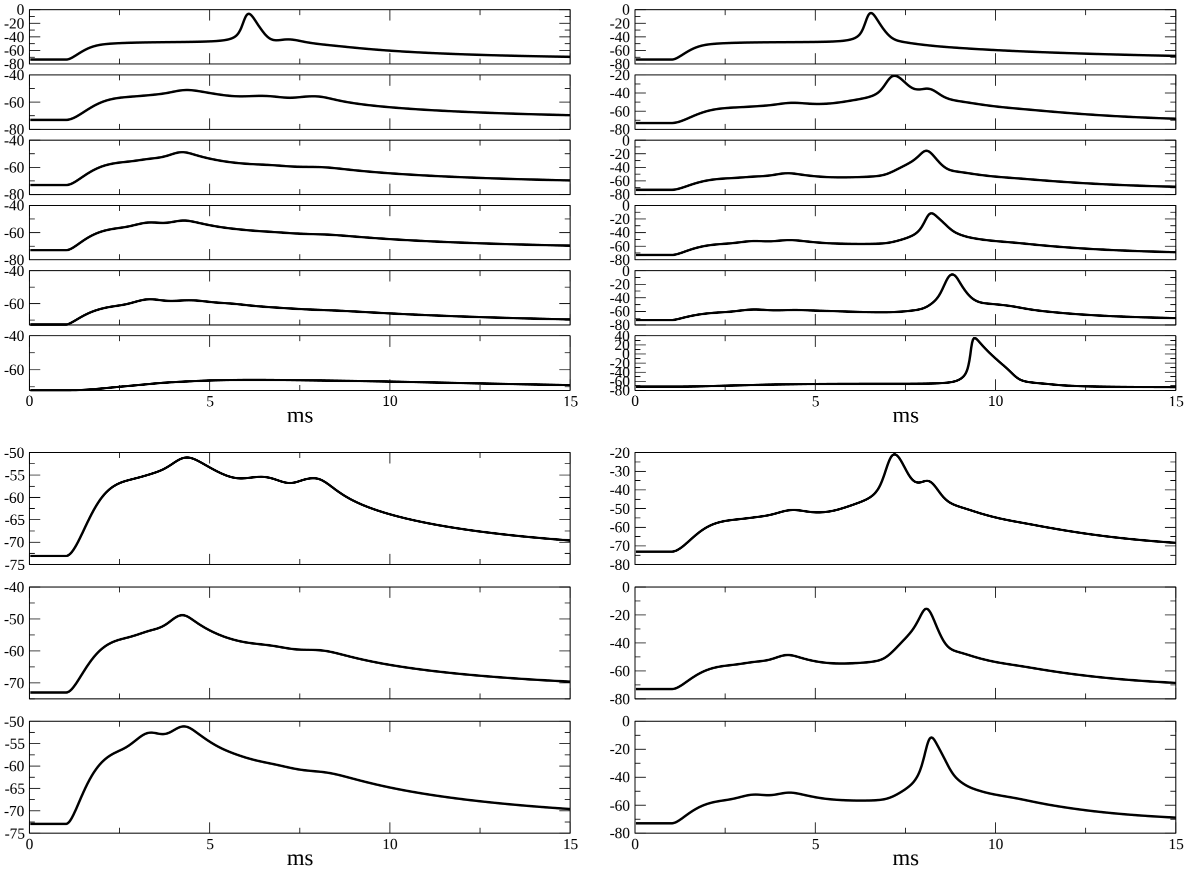

Figure 5.17: Rrespresentative traces of voltage vs. time from a paired-input protocol with a recording set-up as shown in figure 5.16. See text for details.

left-hand panel is now a large amplitude spike. Effective propagation of the TA-induced Na-spikes is thus a *threshold* phenomenon, requiring sufficient depolarization via SC inputs.

The relative timing of the two inputs strongly affects the efficacy of AP generation, as shown in figure 5.15. The inputs must be sufficiently synchronous in order for the Na-spikes to be gated. Two values of SC stimulus intensity are shown. Note that increasing the SC stimulus intensity in this range significantly improves the likelihood of eliciting an AP without resulting in a laxer criterion for synchronous inputs (the width of the distribution increases only marginally). This is most likely due to the presence of the A-type potassium currents K_A, which rapidly activate given a sufficient depolarization, thereby shunting it out unless overwhelmed by a strong regenerative event.

Burst protocol

In [83] the stimulus protocol for paired SC-TA inputs was a $100ms$, $100Hz$ burst to SLM via the TA pathway paired with a single SC stimulus. Results were obtained for various relative timings between the onset of the burst and the time of the SC input. These results indicated that the probability of eliciting an AP increased as a function of this timing difference (t(SC)-t(TA)) over about $40ms$, after which it decreased due to the activation of GABA-B synapses which have very slow kinetics. We seek to compare our simulations to this data by conducting an identical protocol, noting that inhibition has not been included in the model.

Figure 5.18 (left) shows the probability of generating an AP as a function of the

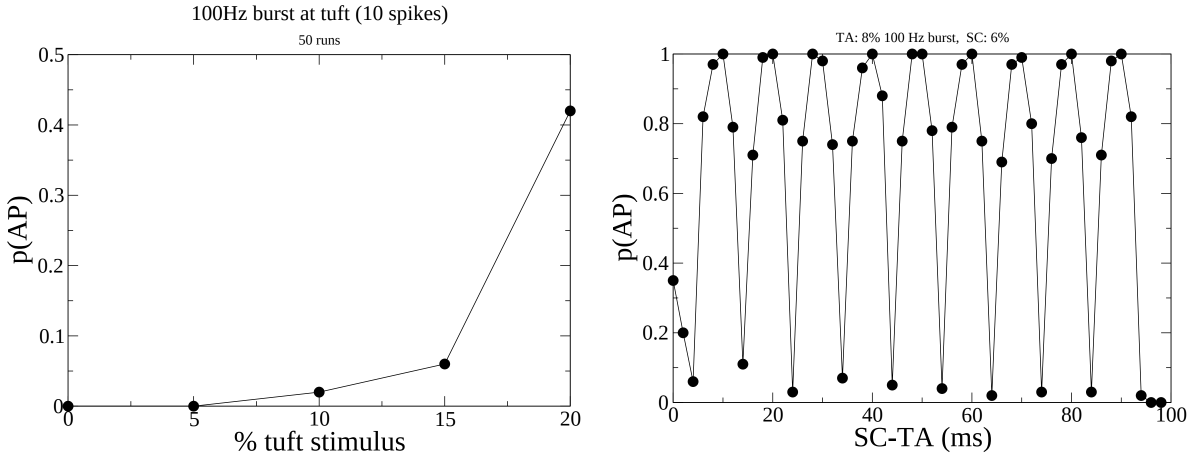

Figure 5.18: Left: Probability of generating a somatic action potential with a $100Hz$ burst of 10 spikes via the TA pathway (unpaired with SC). Right: Response of cell to TA burst paired with SC input. The timing difference SC-TA indicates the time lag between onset of the burst and activation of SC input. Symbols are averages of 100 trials and lines are meant as a guide to the eye.

TA stimulus intensity for a burst protocol. Note that whereas for a single stimulus at the tuft no AP occured, for a burst they do occur. Pairing with a single SC stimulus for various timing differences yields the curve given in figure 5.18 (right). Note that while the likelihood of eliciting an AP increases between 0 and 1, thereafter it saturates, oscillating in phase with the TA burst. Thus for these parameter values there is little if any summation of EPSPs via the TA pathway, and each spike in the burst acts essentially independently.

Figure 5.19 shows averaged traces from simulations with the burst protocol, grouped according to whether an AP occurred or not. It is clear from the data that Na-spikes generically occur, but APs occur only when the spikes are ‘gated’ through to the soma. In fact, Na-spikes occur after almost every post-synaptic potential (PSP) from the TA burst. The rapidly activating A-type potassium current then hyperpolarizes

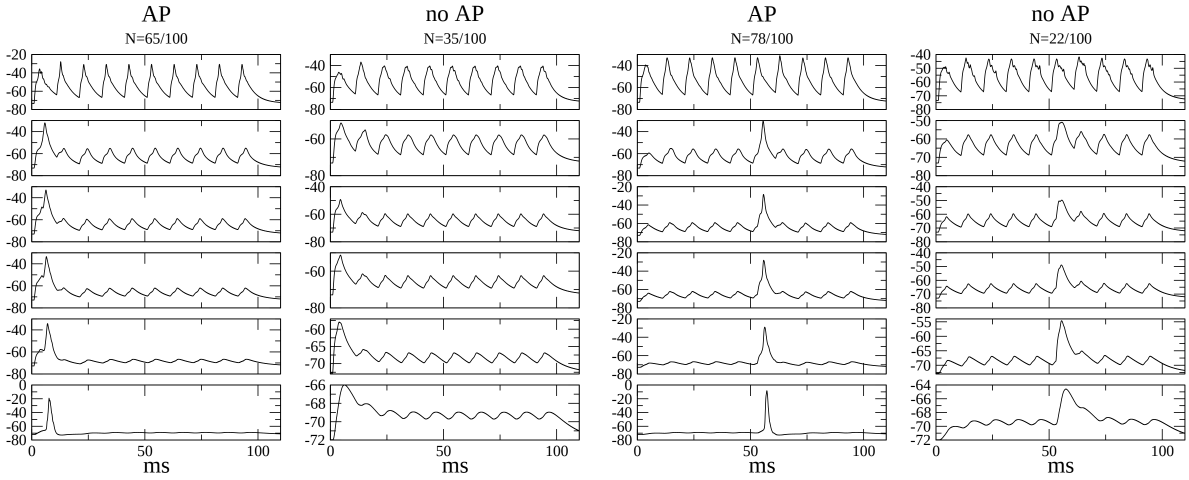

Figure 5.19: Averaged traces for the burst protocol with 8% stimulus via TA and 6% via SC. The time lag between onset of the burst and activation of SC input is 0 (left) and 52 ms (right).

the tuft and no summation occurs from spike to spike. Thus the likelihood of gating a Na-spike through to the soma depends only on the relative timing between the SC input and the next spike in the burst. This results in a probability which oscillates exactly in phase with the burst as in 5.18 (right).

Recent data indicates that the density of A-type potassium channels may actually decrease in the tuft [84]. We note that from 5.5 the density in the A-type potassium channels increases 5-fold from the soma to a distance of $500\mu m$ at which point it saturates. To investigate the effect of a decrease in this density in the apical tuft, we drop the density from $6g_K$ to just $2g_K$ for all dendrites at a distance $> 500\mu m$. The channel density thus increases linearly from the soma and then suddenly drops off at $500\mu m$.

Figure 5.20 shows the probability of generating an AP for the paired burst protocol with a decreased density of K_A channels in the tuft. The probability now increases on

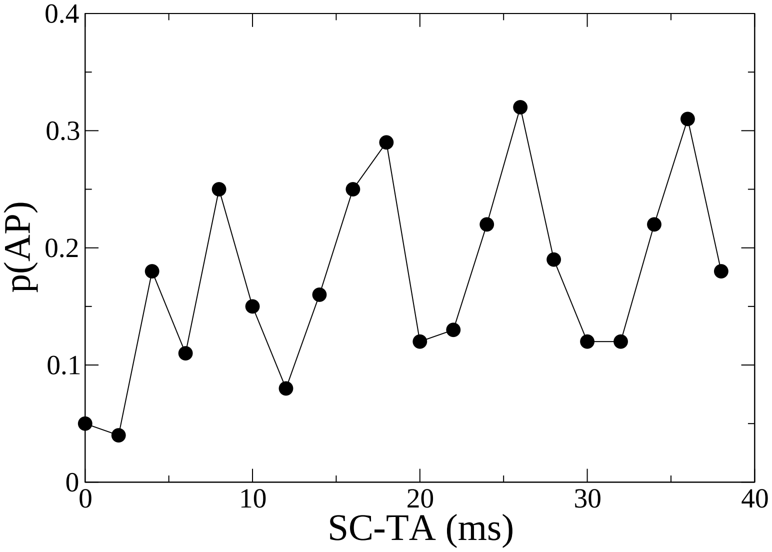

Figure 5.20: Response of cell to TA burst paired with SC input for low A-type K density of channels in the tuft. Stimulus values are 1% TA and 5% SC. Symbols are averages of 100 trials and lines are meant as a guide to the eye.

average until about 30 ms, indicating that summation is occuring. Furthermore, the saturation occurs for approximately the same time delay as in [83]. Note furthermore that the probability does not oscillate precisely in phase with the burst, i.e. the peak probability lies between the spikes in the burst.

Figure 5.21 shows both averaged (upper) and unaveraged (lower) traces, which clearly show the summation of spikes during the burst. Note, for example, for those runs where no AP was generated, the steady increase in the depolarization in the tuft over the course of the first 30 ms. Note, in addition, the latency between the SC input and the gating of the Na-spike compared with the analogous traces in figure 5.19. With a lower density of K_A in the tuft, smaller depolarizations may now summate (TA stimulus is now only 1%) making the optimal pairing with SC a few *ms before* the next spike in the TA burst. In this way the EPSPs have time to summate and

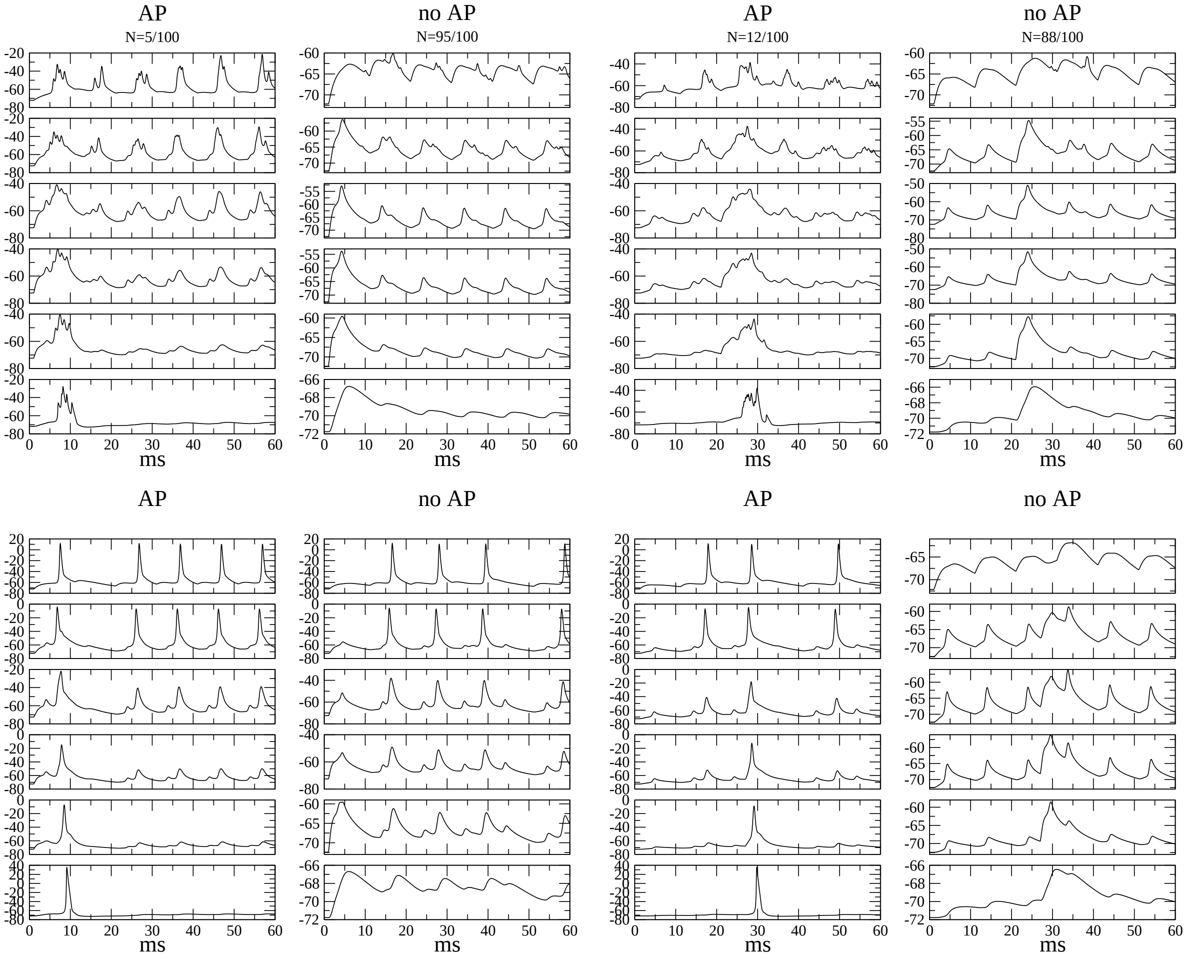

Figure 5.21: Averaged (upper) and unaveraged (lower) traces from the paired-burst protocol with a low density of A-type potassium chanels in the tuft. Stimulus delays are 0 and 26 *ms* respectively.

generate a Na-spike just at the point of maximal depolarization in the apical dendrite from SC input.

5.5 Conclusion

The dynamical picture for coincidence detection of TA and SC inputs in CA1 pyramidal cells presented here is experimentally verifiable. Experimental protocols involving double intracellular recording electrodes have been performed successfully in the past [82]. Such a double-electrode set-up allows the experimentalist to determine if somatic APs are being generated by forward-propagating Na-spikes much as we have done in figure 5.12.

Stimulating electrodes in TA and SC are needed and stimulus intensities should be chosen for which either input alone would be mostly subthreshold. Nonetheless, verification that even subthreshold stimulation via the TA pathway generates Na-spikes is needed. Verification of localized (no somatic AP) Na-spikes in the proximal apical dendrites has been made in intracellular recordings [82], which is not possible in the apical tuft given the very small diameter of the dendrites. Voltage-sensitive dyes might be a viable alternative.

The ability of CA1 pyramidal cells to act as coincidence detectors for TA and SC inputs provides a simple mechanistic description of how the two pathways converge before leaving the hippocampus. Both having originated initially in the entorhinal cortex, one takes a circuitous route through the dendate gyrus and CA3 region while the other projects directly to CA1. The output of CA1 pyramidal cells then reflects the relative timing and intensity of activity coming from these two pathways. This picture is, however, considerably complicated by the presence of inhibitory interneurons and various other intra- and extra-hippocampal projections.

Chapter 6

Excitable Integrate-and-Fire Neurons in a Small-World Network

6.1 Integrate-and-Fire neurons in networks

One of the major challenges of computational neuroscience is to describe the collective behavior of many coupled neurons. In the last chapter we saw the lengths to which it may be necessary to go in order to understand one aspect of the dynamics of just a single neuron. Even such complex, spatially extended models of neurons are greatly simplified and most likely fail to capture the full spectrum of dynamical states in real neurons. To tackle a network of potentially many thousands of neurons seems daunting indeed.

The hope is that certain simplified dynamical rules may be discerned, which govern the behavior of single neurons in some parameter regime. Perhaps, for some parameter values, the state of the neuron lingers near a low-dimensional manifold of an attractor, which in its entirety is very large and high-dimensional. In this case, with some ingenuity and luck, one can formulate a low-dimensional dynamical system to model the neuronal dynamics. Coupling these systems constitutes a network of neurons. It is known, for example, that Hodgkin-Huxley type, conductance-based models of neurons can be broadly classified as either class-I (saddle-node bifurcation on a circle) or class-II (Hopf bifurcation) excitable depending on the nature of the bifurcation from the rest state to the firing state. Near this bifurcation, the dynamics can be described via an asymptotically correct canonical model [85].

Still, the reduction to canonical form assumes that the original, ODE description of neuronal dynamics is the correct one. In the last chapter we show the importance of the spatial distribution of inputs in determining the response properties of the neuron. The fact then remains that the correct choice of model depends crucially on the specific aspect of neuronal dynamics that the researcher wishes to investigate. If we mean to study networks we must use reduced models with potentially unjustified and uncontrolled approximations. There is, as of yet, no alternative.

In this chapter we investigate a network of coupled, excitable integrate-and-fire neurons (IFN). The IFN is a heuristic model of class I excitability, which is characterized by a vanishing frequency near the bifurcation to repetitive firing. It is a one-dimensional model:

$$\begin{aligned} C\frac{dV}{dt} &= -g(V - V_{rest}) + I, \\ V(t^{+}) &= V_{\text{reset}} \quad \text{whenever} \quad V(t^{-}) = V_{\text{threshold}}, \end{aligned} \tag{6.1}$$

with the reset condition that introduces a discontinuity in the voltage whenever a threshold is exceeded. This discontinuity is meant to model the action potential. By throwing out information about the amplitude and profile of the action potential, (6.1) represents a major simplification of neuronal dynamics. Note that in the absence of external drive, $I = 0$, the neuron modeled by (6.1) just settles down to its rest potential. For subthreshold I, the neuron acts as a leaky integrator. Thus (6.1) describes neuronal dynamics as a linear, subthreshold regime with a sharp threshold to spiking. This is clearly a cartoon description of a neuron, but nonetheless one that captures the defining features of neuronal dynamics.

The true advantage of (6.1) becomes apparent when considering a large ensemble of coupled neurons. We note first that given a fixed, suprathreshold I, the interspike interval (period of spiking) of the neuron is given by

$$T = \tau \ln\left(\frac{I/g + (V_{\text{rest}} - V_{\text{reset}})}{I/g - (V_{\text{threshold}} - V_{\text{rest}})}\right), \qquad \tau = C/g, \tag{6.2}$$

which goes to infinity as $I/g \to (V_{\text{threshold}} - V_{\text{rest}})$. The result (6.2) is obtained through simple integration of (6.1). Consider now a network of N coupled neurons, where the ith neuron evolves according to (6.1) except that the current input I is given by

$$I_i(t) = I_0 + g_{syn} \sum_{j=1}^{N} w_{ij} \int_0^{\infty} d\tau J(\tau) E_j(t - \tau), \tag{6.3}$$

where E and J are the pre-synaptic spikes and post-synaptic responses, respectively. E might be modelled by a train of delta spikes, one for each action potential fired by the pre-synaptic cell, and J is typically an α-function or difference of exponentials. In (6.3), neuron i integrates over all inputs E, which are convolved with its response J, and if the neurons are connected ($w_{ij} \neq 0$), then this input results in a post-synaptic current (PSC) with an amplitude proportional to g_{syn}.

Even for a more complicated current as given by (6.3), we can integrate equation (6.1) to obtain the firing times of each neuron, which now depend on the firing times of all the other neurons. The dynamics of such a network of N coupled IFNs is thus equivalent to N coupled one-dimensional maps. The existence and stability of phase-locked states can be analyzed straightforwardly for such a system [86].

We can clearly see that all the complication of solving the network equations resides in (6.3), and in particular in the coupling coefficients w_{ij}. This is the conceptual advantage of coupled IFNs: we know the intrinsic dynamics are trivial and that all the interesting behavior comes about through the particular topology of the network. The problem is to predict the firing times T_i from the coupling coefficients w_{ij}.

The IFN is often proposed as a model to study the collective dynamics of cortical pyramidal neurons, the most prevalent principal excitatory neuron in the cerebral cortex. Pyramidal neurons are class-I excitable, and (6.1) is the simplest possible model of this type. One very robust feature of real cortical neurons is their low, intrinsic firing rate. This seemingly stochastic background firing is due to the large number of uncorrelated inputs each cell receives, both from inside and outside the brain region in which it resides. In the preceeding chapter, for example, we saw that realistic numbers of synapses for hippocampal pyramidal cells are on the order of sixty thousand. Cortical neurons generally receive fewer synapses, but still on the order of tens of thousands. Introducing noise into (6.1) makes the formulation via coupled maps impractical. In this case, advantageous use has been made of 'kinetic' descriptions of the probability distribution for the voltage of the neurons [87, 88, 89] using Fokker-Planck (FP) equations. If the coupling is weak and the inputs mostly uncorrelated, then the equilibrium states of the FP equations and the instabilities of these states can be studied with traditional methods of nonlinear analysis.

Fruitful analysis of the coupled-map formulation relies on the network exhibiting a high degree of symmetry, while the FP formulation can only be meaningfully solved when the network exhibits disordered dynamics. Unfortunately, it seems that real cortical networks are somewhere in between [90, 91]. Actual data on the patterns of synaptic connectivity in the cortex are scarce, but the propagation of waves of excitation observed in experiment [92] provides evidence for the existence of some degree of local connectivity. Yet it is also certainly true that long-range excitatory connections are also present [91, 93]. Finally, neither the local nor the long-range connections are expected to be completely regular; the network exhibits some degree of randomness.

While most work in the past has focused on either all-to-all coupling [94, 95, 96, 86], local coupling (such as nearest-neighbor) [97, 86], or random coupling [87, 88, 89], we shall try to incorporate some aspects of a real cortical network: the coexistence of local and long-range excitatory connections. This type of network, the small-world network (SWN) [98], has received much recent interest. The SWN is a regular, local lattice, complemented with an overlaid network of random connections that may have any length.

The dynamics of different types of networks of active elements with SWN topology have been studied. Both relaxational and non-equilibrium dynamics of spin models in SWNs have been considered [99, 100, 101]. Complex networks of excitable elements include models for propagation of epidemics [102], where the excited state corresponds to the infected state, and neuronal models [103], where the excited state is associated with firing activity. Complex networks of oscillatory elements have been analyzed [104, 105], with particular emphasis on their synchronization properties [106].

In this chapter we study a SWN of IFNs and find many interesting dynamical states. The hope is that, despite the great oversimplification inherent in the description of a neuronal network via coupled IFNs, some insight can be had as to the possible effect of long-range excitation in cortical networks.

6.2 Transition from Persistent Activity to Failure

We consider a simple, one-dimensional model of integrate-and-fire neurons (IFNs) in which the coexistence of regular local coupling and randomly placed global coupling provides a SWN topology. The membrane potential of the IFNs is determined by

$$\tau_m \frac{dV_i}{dt} = -V_i + I_{ext} + g_{syn} \sum_{j=1}^{N} \sum_{m} w_{ij} \delta(t - t_j^{(m)} - \tau_D). \tag{6.4}$$

The last term models input currents due to presynaptic firing as a delayed impulse: if w_{ij} is non-zero, then neuron i receives input of amplitude g_{syn} with a delay τ_D after neuron j has fired its m^{th} spike at time $t_j^{(m)}$. A neuron fires whenever its voltage exceeds $V_{\text{threshold}} = 1$; the voltage is then reset to $V_{\text{reset}} = 0$. The external current is chosen to satisfy $I_{ext} < 1$; in this regime the IFNs are not oscillatory, but excitable. The synaptic conductance is chosen to satisfy $I_{ext} + g_{syn} > 1$, so that a single input suffices to sustain firing activity. For simplicity we choose nearest-neighbor couplings ($w_{i,i\pm1} = 1$) for the underlying, regular lattice. A fixed fraction pN of *additional* unidirectional couplings $w_{ij} = 1$ is then randomly added to the network.

At $p = 0$, any excitation sufficient to cause a neuron to fire will generate two pulses which propagate through the regular lattice in opposite directions with velocity $v = 1/\tau_D$, and either exit the system or annihilate each other depending on boundary conditions (see top left panel of figure 6.1 for the case of periodic boundary conditions). No persistent activity results in either case. However, self-sustained activity may arise for nonzero p. Figure 6.1 shows typical network dynamics for four values of p (0.0,0.05,0.1,0.15, increasing from top to bottom, left to right). Each panel contains a raster plot indicating the times at which each neuron fires, and a plot of the instantaneous firing rate. The addition of long-range connections allows for the reinjection of activity into the network. This leads naturally to a state of persistent activity as seen for $p = 0.05, 0.1$. The firing pattern for $p = 0.05$ appears highly regular, and a Fourier spectrum of the instantaneous firing rate (figure 6.2) reveals a purely periodic pattern. In such a case the activity can truly be called persistent, since once the system settles into a limit-cycle attractor only external perturbations could cause the activity to die. For $p = 0.15$ the activity spreads through the network but once before dying.

Figure 6.1 merely offers an illustration of some representative dynamics, but it should be emphasized that for fixed parameter values many different realizations of the network topology are possible. In fact, for a fixed N and p there are N^{2pN} possible network realiztions (the factor of two arises from the choice of a pre- and a post-synaptic neuron for each global connection). Repeated numerical experimentation reveals that observation of periodic or higly ordered patterns is typical for low p. Still, given the random nature of the system, a statistical classification of the network

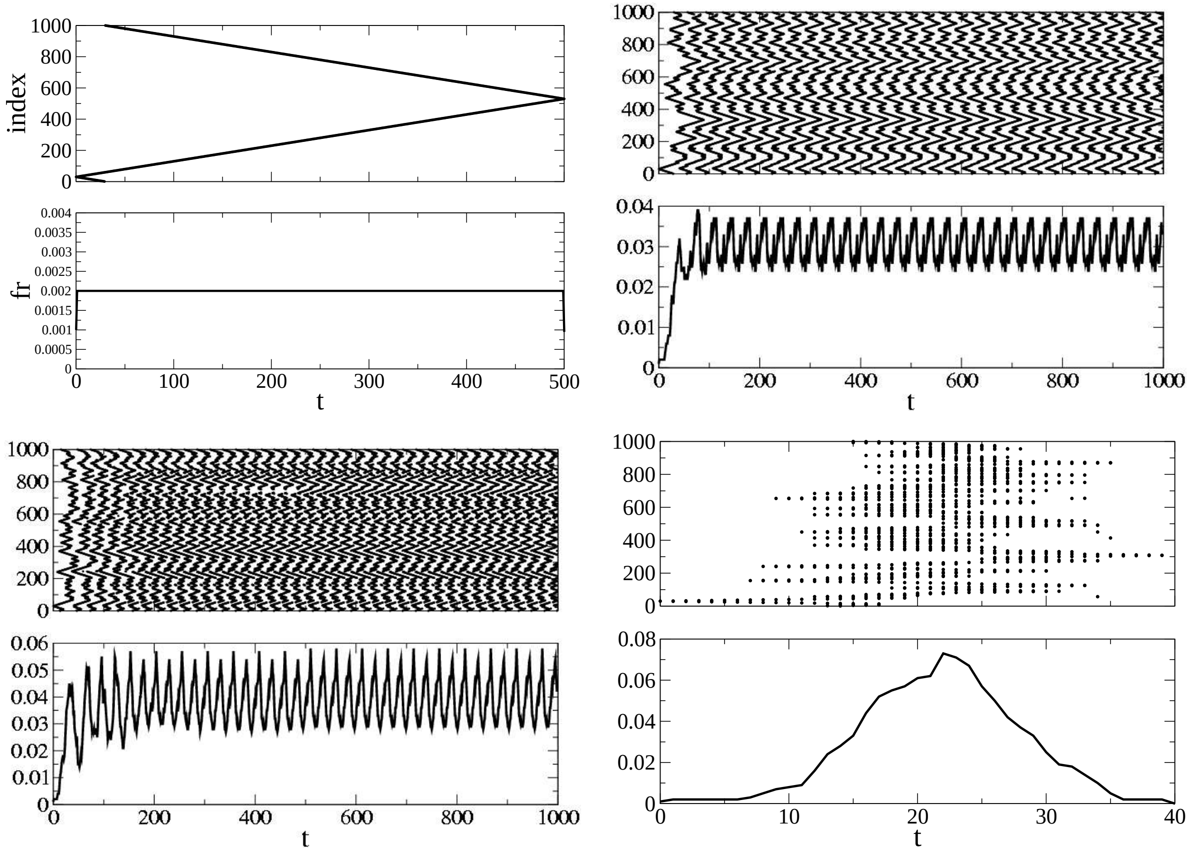

Figure 6.1: Representative raster plots (top of each panel) and instantaneous firing rates (bottom of each panel) for a system of 1000 neurons. Parameter values are $I_{ext} = 0.85, g_{syn} = 0.2, \tau_m = 10, \tau_D = 1, p = 0.0, 0.05, 0.1, 0.15$ from left to right and top to bottom. Same parameter values are used in subsequent figures unless otherwise noted.

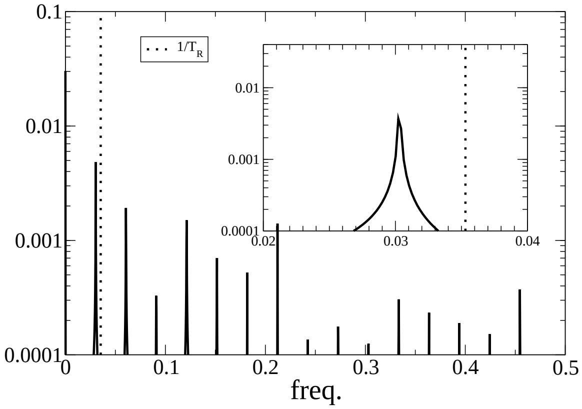

Figure 6.2: Fourier spectrum of the instantaneous firing rate for the periodic state ($p = 0.05$) shown in the upper-right panel in figure 6.1.

dynamics is natural.

In particular, for fixed p, some networks exhibit persistent activity, while in others the activity rapidly decays. It may be of interest to examine how this transition from persistent activity to failure occurs in a particular network realization, but we will restrict our analysis to a probabilistic description of this transition. We will ask: what is the probability, given fixed parameter values and thus a fixed density of shortcuts, that a network chosen at random will yield persistent activity? To obtain these probabilities we calculate long-time averages of the network for many different realizations. We emphasize that the random, global connectivity is fixed for each realization and (6.4) thus constitutes a quenched network.

We typically average over 2000 realizations to calculate the probability of persistent activity; the complementary probability of *failure* to sustain activity is shown in figure 6.3 as a function of the density p of random connections for four different system sizes N. In this regime, the probability of *failure* is an increasing function of p that crosses over from 0 to 1 with increasing steepness as the size N of the system

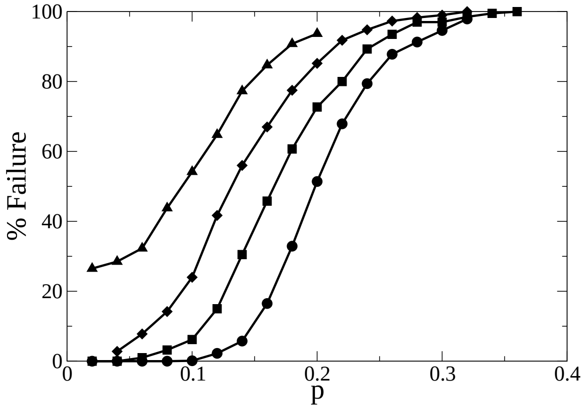

Figure 6.3: Failure rates for different system sizes, $N = 250, 500, 1000, 2000$ are denoted by triangles, diamonds, squares and circles, respectively ($\tau_D = 1$) .

increases.

Failure to sustain activity can be understood as a simple consequence of the intrinsic dynamics of the neurons. Pulses travel outwards from an initial seed of activity, and spawn new pulses more or less rapidly depending on the density of long-range connections p. A neuron j which fires at a time t_j will see activity return to itself at a time $t_j + T_j$. The neuron will fire in response to this input only if sufficiently recovered from the previous firing. This recovery time T_R is easily calculated from 6.4,

$$T_R = \tau_m \ln\Big(\frac{I_{ext}}{I_{ext} + g_{syn} - 1}\Big). \tag{6.5}$$

Note that in figure 6.2 the frequency of the global oscillatory activity is smaller than $1/T_R$ (dotted line), as it must be. Therefore, for $T_j \geq T_R$ neuron j will fire again. For a given realization, the T_j's may differ for all j and, in fact, will change from one cycle to the next. The preceeding argument, while correct, is thus impractical for determing whether network activity will persist or die out. We can overcome this difficulty through a mean-field approximation in which the T_j's are assumed to be all identical, and thus depend only on the density of connections p and not the particular topology of any specific network realization. We make the further assumption that this uniform value of T_j is equal to the time $T_A(p)$ needed for activity to spread throughout the entire network. This argument assumes that each neuron only receives one input per cycle, via either a local or a global connection. Equating the recovery time with the time for activity to spread throughout the network yields the critical density at which a transition from persistent activity to failure is expected to occur

$$T_A(p_{cr}) = T_R. \tag{6.6}$$

An approximate form for $T_A(p)$ is easily derived. We assume that a single neuron fires at time $t = 0$. Given a density p of shortcuts we expect a long-range connection will be reached after $1/p$ neurons have fired, which occurs after a time $\tau_D/2p$ since there are two waves. Four wave fronts are now present and so $2/p$ neurons will fire in a time $\tau_D/2p$ at which point on average two new wave fronts are generated, and so on. During the k^{th} cycle, the number of neurons excited is $2^{k-1}/p$. After n cycles all the neurons have been excited, which results in

$$\sum_{k=0}^{n-1} 2^k = pN, \tag{6.7}$$

which leads to a time

$$T_A(p) = \frac{\ln(1+pN)}{2p\ln 2}. \tag{6.8}$$

Using (6.8) we can solve for $p_{cr}(N)$ in (6.6), and rescale the curves shown in figure

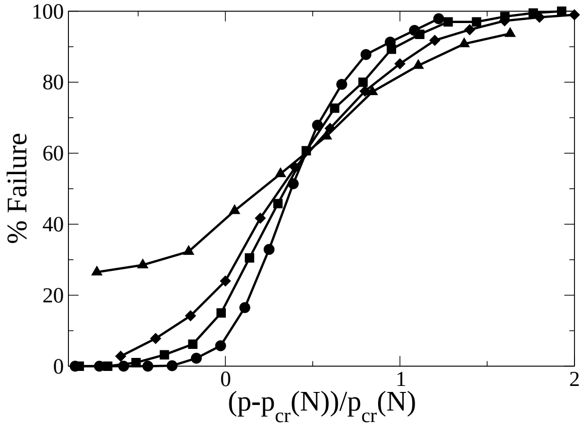

Figure 6.4: Failure rates as a function of a rescaled density of shortcuts.

6.3 to obtain figure 6.4. The intersection of all the curves at the predicted critical value of the density indicates that the transition does indeed occur as hypothesized. Note, however, the fixed offset of the rescaled curves (the crossing should occur at zero), due to approximations made in deriving (6.8), as discussed below.

The local dynamics in equation (6.4) are simple: waves travel outward with a constant velocity $1/\tau_D$. Locally, the waves trace out the topology of the network (although global connections may be traversed in one direction only). The intrinsic dynamics of the neurons makes the resulting dynamics complex, i.e. the 'tracing-out' may be hindered if neurons are not sufficiently recovered. Nonetheless, equation (6.8) is a purely geometric result, since the time it takes for activity to traverse the entire extent of the network is related trivially to the largest distance in the network.

Mean-field properties of small-world networks have been worked out by Newmann, Moore and Watts in [107, 108]. In [107] they calculate the fraction of a small-world network covered by starting at a single point and extending outwards a distance r in both directions (equivalent to waves having spread for a time $r\tau_D$ in our case) in a continuum limit. In [108] they refine the continuum limit calculation by taking into account two effects that were omitted from their earlier calculation and from ours. Firstly, as they trace out the network, a jump via a long-range connection may reach a part of the network that has already been traced over and should therefore not be counted. We interpret this as activity spreading via long-range connections, which may be injected into a neuron which has already fired and is not ready yet. Such a connection would therefore be ineffectual. Secondly, when two 'traced-out' sections meet, they stop and no longer contribute. We interpret this as wavefronts which meet and annihilate and thus, thereafter, do not contribute. Considering these two additional mechanisms, they develop a two-component model that describes, effectively, the fraction of the network covered and the number of fronts. The result, interpreted within the context of equation (6.4), yields,

$$\sqrt{\left(1+\frac{4}{pN}\right)}\tanh\left[\sqrt{\left(1+\frac{4}{pN}\right)}\frac{pT_A(p)}{2\tau_D}\right]=1. \tag{6.9}$$

Figure 6.5 shows the failure rates, rescaled by 6.9. The more sophisticated mean-field model clearly captures the transition correctly.

6.3 Activity for slow waves.

The failure rate may become a non-monotonic function of p for large enough delay time τ_D (slow enough waves). Figure 6.6 shows the percentage of realizations in which the activity has died out within a fixed time ($T = 2000$) for seven values of the delay time, increasing from left to right. The first five curves exhibit the

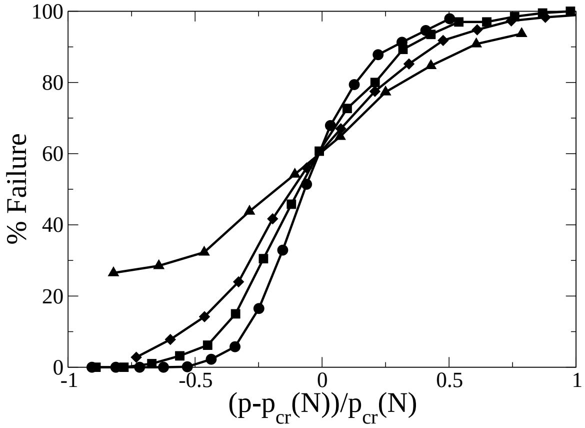

Figure 6.5: Failure rates as a function of the density of shortcuts rescaled according to the mean-field model in [108].

transition from persistent activity to failure at low p discussed in the preceeding section. The failure rate for larger delays is non-monotonic. For $\tau_D = 1.6$ there is an initial increase in the percentage of failing realizations as p increases from zero, in accordance with the analysis from the previous section, but the failure rate does not saturate at 100%. Rather, it reaches a maximum and decreases at higher values of p. For yet larger delays, the maximum both shifts to the left and decreases in magnitude. For sufficiently slow waves, the failure rate (measured at a fixed time) appears to go to zero for all $0 < p < 1$.

Figure 6.7 shows representative patterns of neural activity and firing rates for slower waves for increasing p (top to bottom, left to right). Most striking is the contrast between the regular, often periodic patterns seen in the low-p regime, and the highly disorded patterns seen at values of p near 1. Also clear, especially from the instantaneous firing rates, is the larger magnitude of the population-oscillation for high p. In fact, while for a low density of global connections the spread of activity

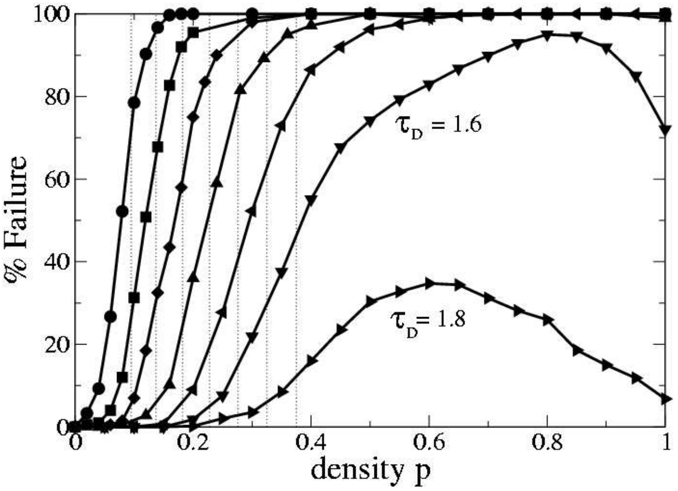

Figure 6.6: Failure rates for a system of 1000 neurons. Curves representing the failure rate after $T = 2000$ are shown for $\tau_D = 0.6, 0.8, 1.0, 1.2, 1.4, 1.6, 1.8$, left to right. The predicted value of p from equation (6.9) at which the failure transition occurs, is given by a dotted line for each curve.

appears conspicuously wavelike (see upper-lefthand panel of figure 6.7), at higher densities the activity spreads extremely rapidly, resulting in a near synchronous firing of the entire population (see lower-right hand panel of same figure). The Fourier spectrum for the latter realization is shown in figure 6.8; the spectrum is clearly noisy although well-defined peaks can be discerned.

The near-synchronous firing of the neurons for high p is not surprising and, in fact, follows from 6.8; the time needed for activity to spread is a decreasing function of p for fixed system size. That is, as p increases, the firing of the neurons will be more and more synchronous. Nonetheless, the re-emergence of *persistent* activity in this regime is unexplained by our earlier description. Also unexpected is the high degree of disorder in the resulting patterns. While the population fires relatively periodically with a well defined frequency, the individual spikes occur in a seemingly

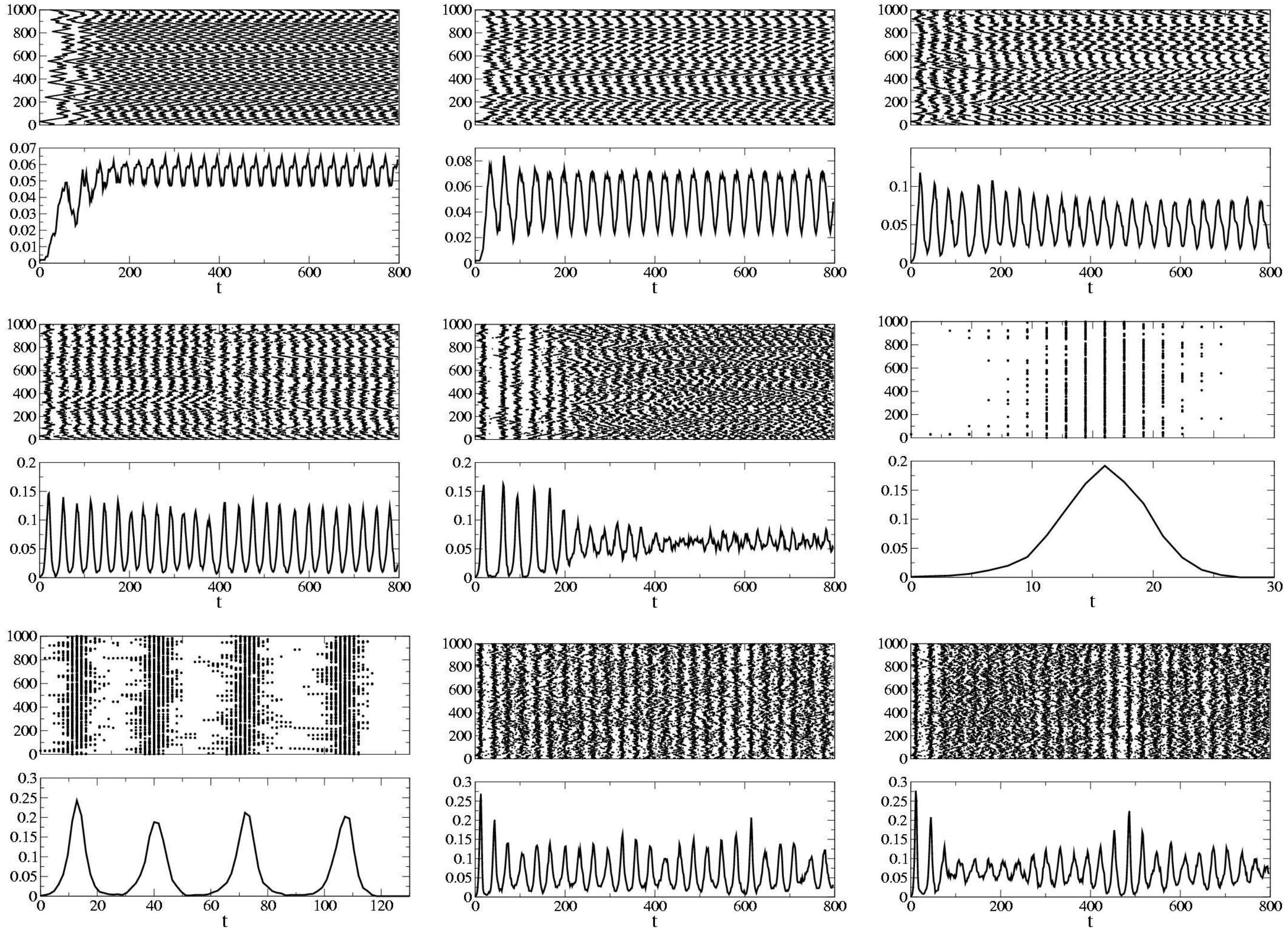

Figure 6.7: Representative raster plots (top of each panel) and instantaneous firing rates (bottom of each panel) for a system of 1000 neurons. Parameter values are $I_{ext} = 0.85, g_{syn} = 0.2, \tau_m = 10, \tau_D = 1.6, p = 0.1, 0.2, 0.3, 0.4, 0.5, 0.6, 0.8, 0.9, 1.0,$ from left to right and top to bottom.

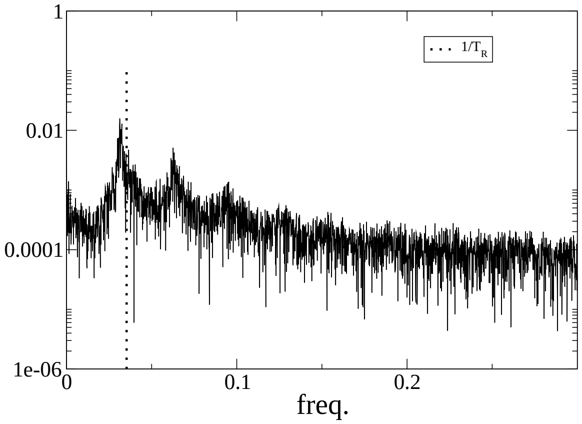

Figure 6.8: Fourier spectrum of the instantaneous firing rate in the lower-right panel of figure 6.7, $p = 1$.

chaotic manner with respect to this oscillation (see lower panels in figure 6.7). The resulting patterns appear as noisy homogeneous oscillations in the firing rate. In addition, modulation of the firing rate on long time-scales is evident.

As a final note on patterns for slow waves, one can see in figure 6.7 that even for values of p below the persistence-failure transition (top and middle rows), several qualitative types of patterns can be found. Note, for example, the dynamics exhibited in the central panel: there is an initial transient of nearly-synchronous population spikes, as seen to the other side of the transition at high p. However, it seems that for p not sufficiently large ($p = 0.5$ in this case) this state is unstable and the system settles into a highly disordered firing pattern for which the firing rate is almost constant.

The network topology

The drastic change in patterns from low to high p is due to changes in the topology of the network, as we shall show. The topology of random networks is often characterized by means of the likelihood of picking a node at random and finding that it has exactly c connections. This likelihood is given by the degree distribution $p(c)$. In a network with N nodes and a fixed probability of making a connection $\bar{p}$ between any two nodes, the distribution is the binomial distribution

$$p(c) = \binom{N}{c}\bar{p}^c(1-\bar{p})^{N-c}, \tag{6.10}$$

which for large N and small $\bar{p}$ can be approximated by the Poisson distribution

$$p(c) = \frac{(\bar{p}N)^c}{c!}e^{-\bar{p}N}. \tag{6.11}$$

Note that for $\bar{p} = 1$ the system is fully connected, i.e. the number of connections is N^N. In our model, a value of $p = 1$ means that there are N connections. Thus here $\bar{p} = p/N$ and 6.11 becomes

$$p(c) = \frac{p^c}{c!}e^{-p}. \tag{6.12}$$

The degree distribution 6.12 does not apply to our model 6.4, since we have stipulated that there be *exactly* pN connections in the network. This choice was made to facilitate the averaging over many realizations of the network. For the case where the degree distribution is given by 6.12, not only are there many possible network topologies for a fixed number of connections, but the number of connections itself is a random variable whose expected value is given by $E = pN$.

Given that the number of connections is fixed in our model, the relevant degree distribution must be derived by keeping track of all the nodes. We consider that the network consists of N nodes of which s_0 have no connections, s_1 have but a single connection and, in general, s_c have c connections. If the total number of oriented shortcuts is k, then c may vary between 0 and k. The constraints

$$s_0 + s_1 + \cdots + s_k = N, \tag{6.13}$$

$$s_1 + 2s_2 + \cdots + ks_k = k, \tag{6.14}$$

indicate that the probabilities will not be independent as in the Poisson distribution. The derivation is therefore more involved than that of 6.12. We first note that the total number of possible shortcut configurations is N^k. The probability of a certain configuration is then just the number of ways to get that configuration divided by N^k.

The number of ways of getting a certain configuration consists of two parts. First, we count the number of ways of choosing s_0 nodes without any connections. The remaining nodes can be ordered in $(N - s_o)!$ ways, but of these many are identical. For example, the s_1 nodes with one connection can be ordered in $s_1!$ ways, all of which are equivalent. Finally, the k connections can be ordered in $k!$ ways, but again we must be careful not to overcount. For example, a node with 3 connections has 3! ways to order those connections, and so there are a total of $(3!)^{s_3}$ ways to order the ‘triple’ connections in the network. The distribution is then given by

$$p(s_0, s_1 \ldots, s_k) = \frac{N!k!}{\prod_{i=0}^{k} s_i!(i!)^{s_i}}. \tag{6.15}$$

Note that this is also the appropriate distribution for the case of choosing k times amongst N objects with replacement. The formula 6.15 is difficult to utilize for computing expectations. We note that (6.15) satisfies the normalization condition

$$\sum_{s_0} \cdots \sum_{s_k} p(s_0, s_1, \ldots, s_k) = 1, \tag{6.16}$$

where the upper bounds on the sums are finite and depend on all earlier sums. The expected number of nodes with $0 \leq n \leq k$ connections is given by

$$E(s_n) = \sum_{s_0} \cdots \sum_{s_k} s_n p(s_0, s_1, \ldots, s_k). \tag{6.17}$$

Note that the distribution 6.15 is valid both for incoming and outgoing connections.

A numerical calculation of the fraction of neurons with two or more incoming (or outgoing) connections as a function of the density p is given in figure 6.9. It is evident that the number of neurons with two incoming connections increases dramatically as p increases towards 1. In addition, it is clear that the majority of neurons with more than one incoming connection has exactly two incoming connections for $p < 0.4$. This observation allows us to make the following assumption in 6.15

$$s_0 = N - k + s_2 \tag{6.18}$$

$$s_1 = k - 2s_2 \tag{6.19}$$

thus ignoring all s_n for $n > 2$. In addition, we calculate the *most likely* value of s_2 rather than the expectation (for simplicity). The most likely value and the expectation coincide for a symmetric distribution, whereas 6.15 only approaches a symmetric distribution as $N \to \infty$. We thus seek the value of s_2 for which $p(s_2+1) - p(s_2) = 0$, and is a maximum. This gives

$$2(s_2+1)(N-k+s_2+1) = (k-2s_2)(k-2s_2-1), \tag{6.20}$$

which for large N becomes

$$s_2 \sim \left[(1+p) - \sqrt{1+2p-p^2}\right]\frac{N}{2}. \tag{6.21}$$

This curve is plotted in figure 6.9 and compared to numerical data. The agreement is good, although for p near 1 the number of neurons with three or more incoming connections is not negligible and causes some discrepancy. Finally we note that for $p \ll 1$, (6.21) gives

$$s_2 = \frac{1}{2}p^2 N, \tag{6.22}$$

which is identical to the small p limit of the expectation from the Poisson distribution

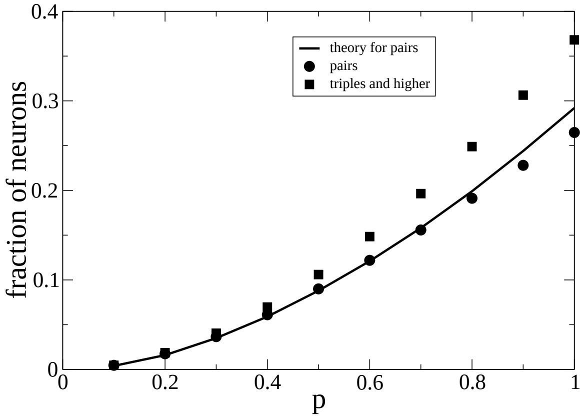

Figure 6.9: Fraction of neurons with two or more incoming connections. Shown are pairs (squares) and three or more connections (circles). Solid line is the prediction from (6.21).

(6.12). For p near 1, (6.21) yields

$$s_2 = \left(1 - \frac{\sqrt{2}}{2}\right)N - \frac{(1-p)}{2}N. \tag{6.23}$$

Comparing this to the value of the expectation for s_2 according to the Poisson distribution for p near 1,

$$E(s_2) = \frac{1}{2e}N - \frac{(1-p)}{2e}N, \tag{6.24}$$

reveals that assuming a fixed number of connections increases the number of neurons with two incoming connections with respect to the case where the number of connections is not fixed by a factor of about 1.6 for $p = 1$.

We thus see that a major topological difference between those networks for which $p \sim 0.1$ and those for which $p \sim 1$ is the fraction of neurons with two or more incoming and outgoing long-range connections. What is the dynamical consequence of this topological change? One consequence is an increased likelihood that a neuron will receive *more* than a single input during each cycle of the network oscillation. In section 6.2 the critical density p_{cr} was calculated with the assumption that each neuron receive only a single input during a cycle. This assumption is implicit in equating the time required to activate each neuron once with the recovery time T_R. In general, in fact, the recovery time will depend on the total number of inputs subsequent to the last firing of a neuron. If the neuron has two or more incoming connections, it may be that as activity spreads throughout the network, a particular neuron will receive several inputs. This has the potential of making the neuron fire earlier than the previously calculated recovery time T_R.

The simplicity of the network equation (6.4) allows us to integrate it explicitly and express the voltage of neuron i since its last firing as

$$V_i(t) = I_{ext}(1 - e^{-t/\tau_m}) + g_{syn} \sum_{r=1}^{n} e^{-(t-t^{(r)})/\tau_m} H(t - t^{(r)}) \tag{6.25}$$

where H is the Heaviside function and the neuron has recieved n inputs since its last firing. When the voltage exceeds $V_{\text{threshold}} = 1$, the neuron will fire. The time at which the voltage first reaches threshold is given by

$$T_R(n) = \tau_m \ln\Big(\frac{I_{ext} - g_{syn} \sum_{r=1}^{n-1} e^{t^{(r)}/\tau_m}}{I_{ext} + g_{syn} - 1}\Big), \tag{6.26}$$

which is clearly less than the value of T_R in equation (6.5) for $n > 1$, but depends on the firing times of those neurons providing input to neuron i, which are unknown.

However, the value of $T_R(n)$ in equation (6.26) is bounded below by

$$T_R(n) = \tau_m \ln\Big(\frac{I_{ext}}{I_{ext} + ng_{syn} - 1}\Big), \tag{6.27}$$

which occurs when all n inputs coincide at $T_R(n)$ itself. The formula (6.27) reduces to (6.5) for $n = 1$.

The time between subsequent spikes of a particular neuron is called the interspike-interval (ISI). If a neuron only receives a single input per oscillation of the network, then the ISI is bounded below by $T_R(1)$. We can determine the ISI of neurons numerically, in order to indirectly discern between those with a single active incoming connection and those with several. Figure 6.10 shows the dynamics of a system for $p = 1$; all those neurons with ISI less than $T_R(1)$ are colored in red. It seems reasonable from this figure to consider the populations of slow and fast spiking neurons as dynamically distinct. In particular, those neurons with large ISIs (black) undergo highly synchronized oscillations, the amplitude of which dips to zero. In fact, this oscillation *should* be synchronized and go to zero according to (6.8). However, for large p there is now a second population of neurons which, by virtue of having received more inputs over the course of the oscillation, are primed to fire before $T_R(1)$. They carry over the activity in the network until the first population has once again recovered. We further remark that the members of the population of fast-spiking neurons change from one oscillation to the next. That is, those neurons which are utilized by the network to bridge the epochs of zero firing rate in the slow-spiking neurons, vary in a seemingly random manner. In fact, it can be seen in figure 6.10 that there is a sudden increase in the number of fast-spiking neurons around $t = 200$, indicating that many more neurons have the potential to fire more quickly than $T_R(1)$ than are typically utilized in a single oscillation.

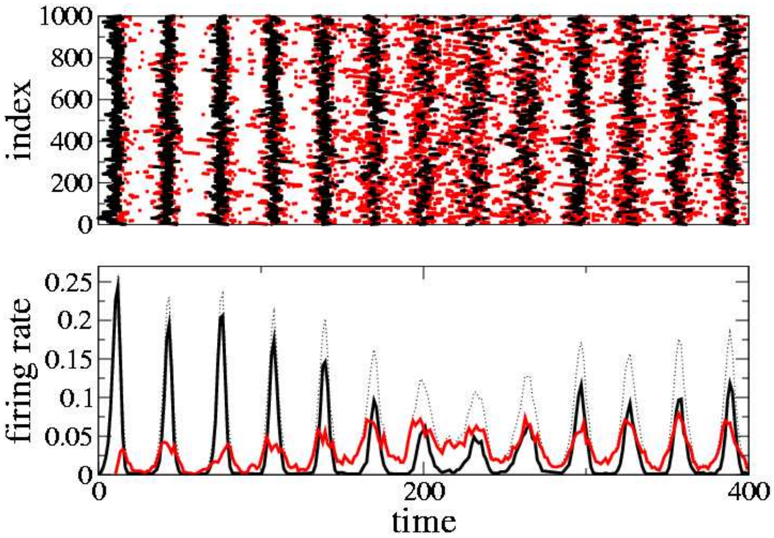

Figure 6.10: Raster plot (top) and instantaneous firing rate (bottom) for a system of 1000 neurons at $\tau_D = 1.5$ and $p = 1.0$. Dotted line (bottom) is the total firing rate. Neurons colored red have $ISI < T_R(1)$.

Consider also figure 6.11, which contrasts the distribution of ISIs for low ($p = 0.1$) and high ($p = 1.0$) densities of random connections. Note that the ISI appears bounded below by $T_R(1)$ in the former case (solid line), while in the latter there are fast-spiking neurons with ISI less than $T_R(1)$. Figure 6.12, for which $p = 0.15$ and $\tau_D = 1.0$, shows that a small number of neurons actually do have ISIs less than $T_R(1)$ (see inset). Note, in addition, that there is a subset neurons with very long ISIs, as indicated by the grouping around 130.

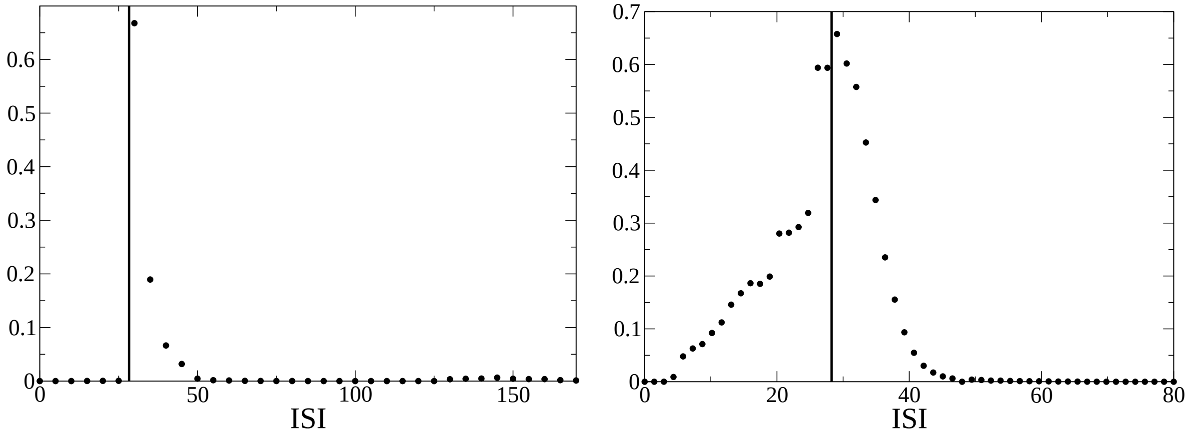

Figure 6.11: Normalized histograms of the ISI for $\tau_D = 1.5$ and $p = 0.1$ (left) and $p = 1.0$ (right). The solid line is $T_R(1)$. Data includes ISIs for all 1000 neurons over many network realizations.

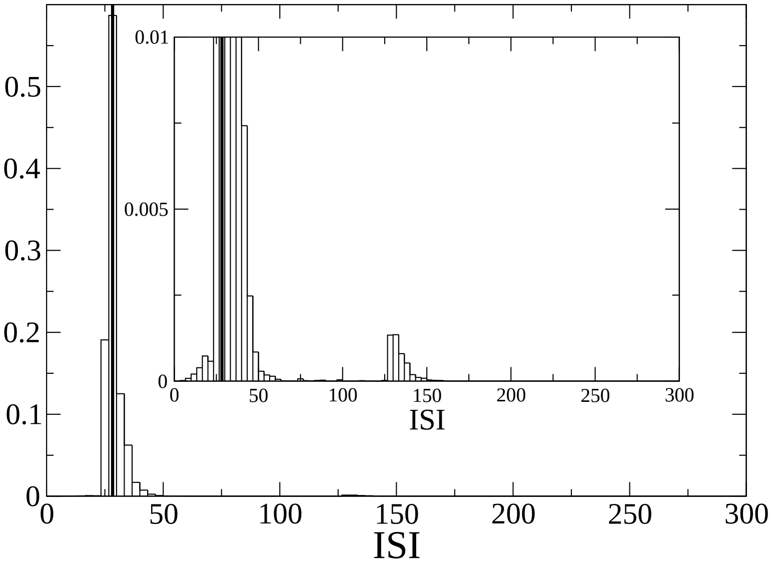

Figure 6.12: Normalized histogram of the ISI for $\tau_D = 1.0$ and $p = 0.15$. The solid line is $T_R(1)$. Data includes ISIs for all 1000 neurons over many network realizations.

Persistence and failure of activity for $p \sim 1$

Typical patterns of activity for $p \sim 1$ are highly disordered. The absence of a limit-cycle attractor introduces the possibility that the activity may fail at long times. This is indeed the case. While in figure 6.6 failure rates are shown for a fixed time $T = 2000$, an analogous figure for failure rates determined at a later time, e.g. $T = 3000$, would show the portion of the curves for $\tau_D = 1.6, 1.8$ near $p = 1$ moving upwards, indicating more failures. For sufficiently large times $T \to \infty$, it appears that all curves would tend towards 100% failure for $p \sim 1$.

Figure 6.13 shows typical examples of such failure of activity at variable times. The top panel ($\tau_D = 1.4$) shows failure occuring after a dozen or so network oscillations. As the delay is increased, for the exact same network and initial conditions, the activity persists for longer times (see middle ($\tau_D = 1.6$) and lower panels ($\tau_D = 1.8$)). The trend therefore seems to be towards longer lifetimes for longer delay and this is true in general.

However, the dependence of the average lifetime on the delay is quite subtle. Figure 6.14 (left) shows cumulative failure rates for various values of the delay τ_D as a function of time. Each curve is determined by finding the times at which failure occurs in 2000 realizations of a network for fixed parameter values. A histogram of the frequency of failures binned by time is then made and integrated. Figure 6.14 shows that the rate of failures indeed decreases as the waves become slower. Nonetheless, the curves for $\tau_D = 1.65$ and 1.7 actually cross indicating that the rate of failures actually *decreases* as the delay increases from 1.65 to 1.7.

The righthand panel of the same figure indicates that such a scenario is ubiquitous

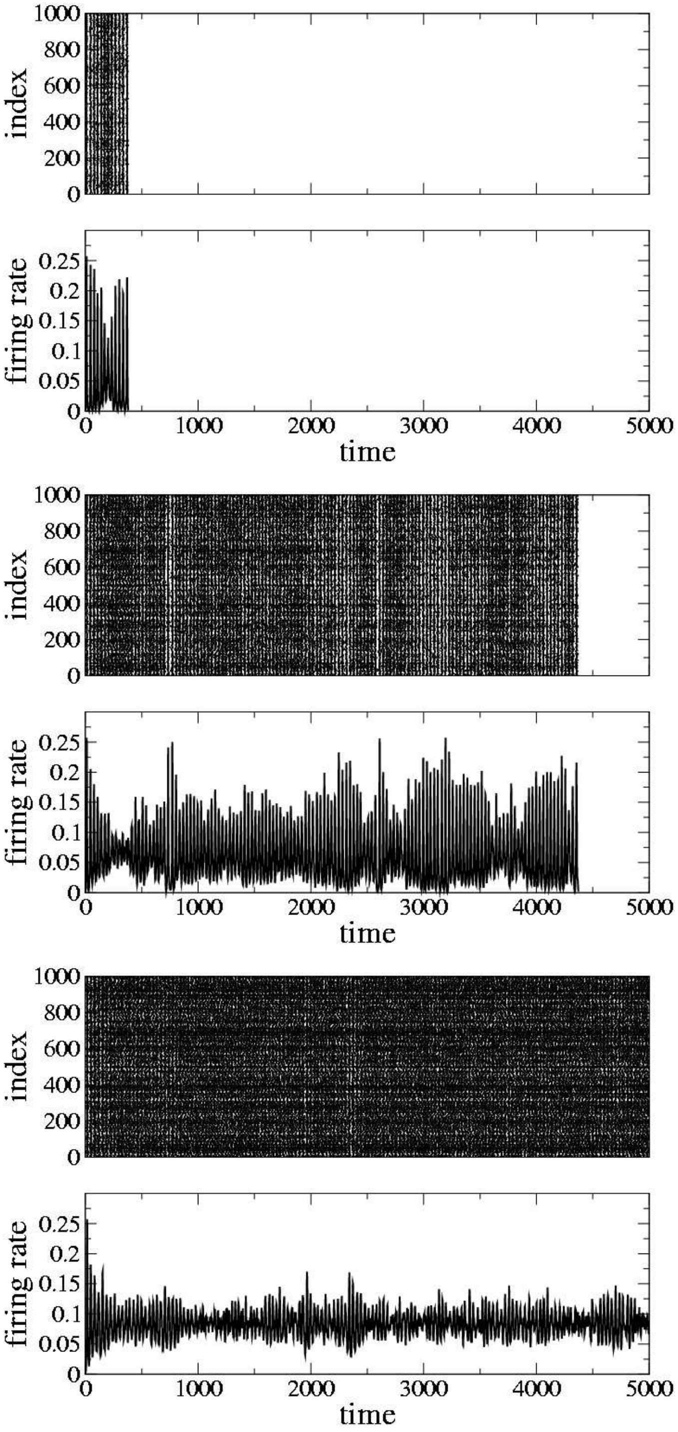

Figure 6.13: Raster plots and instantaneous firing rates for $\tau_D = 1.4, 1.6, 1.8$ from top to bottom and $p = 1$. The network topology and all parameters are identical for all three figures, only the delay has been changed.

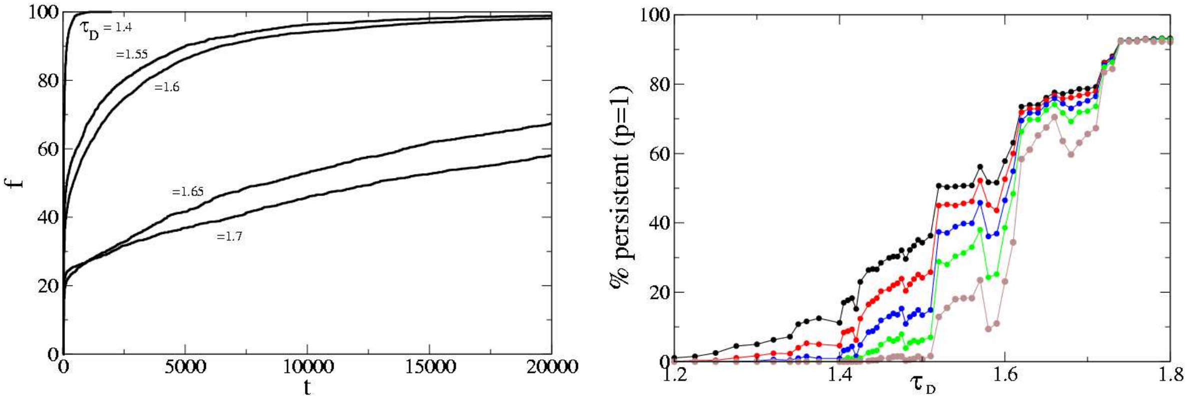

Figure 6.14: Cumulative distributions f of failure times at $p = 1$. Dashed lines show fits to stretched exponentials. Right: Failure rates at 5, 10, 20, 40 and 100 multiples of $T_R(1) = 28.3$, black to brown. Symbols are averages of 2000 realizations.

as a function of the delay. The percentage of persistent realizations are shown as a function of the delay at 5 different fixed times (see caption for times), increasing from the top to the bottom curve. The high degree of structure shows that the failure times depend sensitively on the delay. The non-monotonic nature of the curves furthermore points to the fact that there are *preferred* values of the delay (locally speaking) for which activity persists longer. Such values might be considered 'resonant'.

The cummulative failure rates in figure 6.14 are well fit by a stretched exponential function of the form

$$f = f_\infty - ce^{-\alpha t^\beta}, \tag{6.28}$$

where the value f_∞ gives the percentage of realizations for which activity will have failed at infinite time. While the fits are good, the coefficients obtained from fitting the data in figure 6.14 to this form are not reliable. Table 6.1 shows some sample fit values; [1] the data has been fitted starting from $T_s = 0, 1000$ and 5000. The

---

[1] All fits were done with the intrinsic non-linear curve-fitting function in xmgrace.

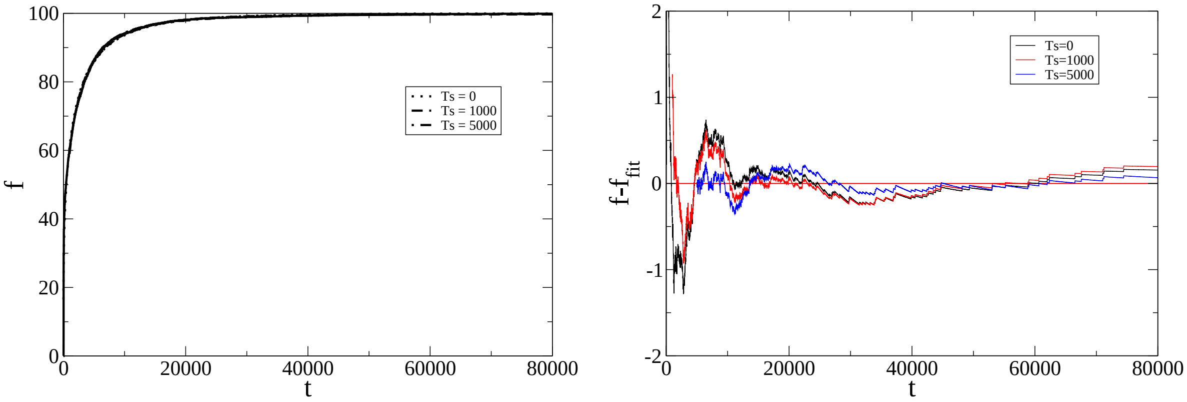

Figure 6.15: Left: Stretched exponential fits to cumulative failure rates. Here $\tau_D = 1.6$. Fits are to data with $0 < t < T_s$. Right: Difference between cummulative failure rate and stretched exponential fit.

T_s	f_∞	c	α	β
0	100	80.6	0.015	0.558
1000	100	88.2	0.017	0.550
5000	100	678	0.330	0.290

Table 6.1: Coefficients of stretched exponential fit.

coefficients vary non-monotonically and do not converge. In fitting many such curves for various starting and ending times, at no point were the coefficients found to converge. Nonetheless, figure 6.15 (left) shows that the three curves given by these coefficients are nearly indistinguishable from each other and fit the data well. The difference between the cummulative failure rates and the fits (figure 6.15, right) show that deviations are not random and seem to have an oscillatory time dependence.

As a note on the use of a stretched exponential fit, if we assume that each realization has a probability of failure p_f and that these probabilities are distributed across realizations according to $\rho(p_f)$, then the percentage of failures over many realizations is given by

$$< f(t) >= 100(1 - \int_0^\infty dp_f \rho(p_f) e^{-p_f t}). \tag{6.29}$$

Equation 6.29 is known to have a stretched exponential solution of the form $< f(t) >= 100(1 - e^{-\alpha t^\beta})$ for $\beta = 1/2$ when

$$\rho(p_f) = \frac{1}{2p_f^{3/2}} \sqrt{\frac{\gamma}{\pi}} e^{-\frac{\gamma}{4p_f}}, \tag{6.30}$$

with $\gamma = \alpha^{1/\beta}$ [109].

The trend towards longer life-times for larger delay τ_D can be explained simply. In order to bridge the quiescent periods between near-synchronous firing of the population of slow-spiking neurons ($ISI \geq T_R(1)$), the network makes use of those neurons which, having received additional excitation during the oscillation, are primed to fire earlier than $T_R(1)$. Such neurons must be arranged in a topological chain so that they can be activated one after another. If such a chain has length l, the time bridged via this chain is $l \cdot \tau_D$. Thus, given a fixed topology, more and more chains can be utlilized as τ_D increases. Put another way, the probability that the quiescent period can be bridged must depend on the distribution of available chains and the time bridged by each chain. Because the time bridged by each chain goes up as τ_D increases, the likelihood that the quiescent period will be successfully bridged also increases.

6.4 Bistability and Noise

One of the salient features of the emergent dynamics of the model (6.4) in the presence of random, long-range connections is persistent *self-sustained* activity in the low p

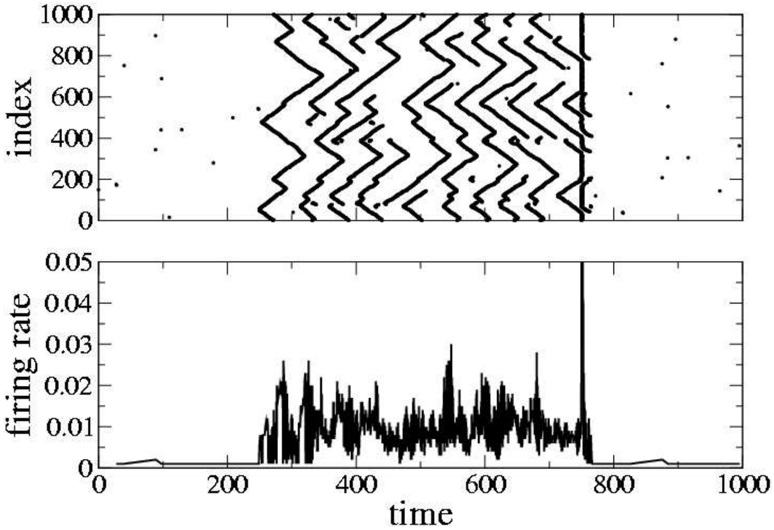

Figure 6.16: Raster plot (top) and instantaneous firing rate (bottom) for a system of 1000 neurons and 100 interneurons ($p = 0.10$) with $k = 5$. Noise causes the neurons to fire stochastically but is insufficient to generate traveling pulses. About 10 adjacent neurons are stimulated synchronously at $t = 250$; 20% of the neurons are activated at $t = 750$ to turn the active state off.

regime. In this regime the network is in fact bistable between 'off' and 'on' states, and can be switched between them with a sufficiently large stimulus, as illustrated in figure 6.16. The synchronous stimulation of a sufficiently large number of neurons while the network is in the 'on' state will increase the level of activity and effectively push the network above the failure transition (cf. figure 6.3), causing a transition into the 'off' state.

Network bistability has been hypothesized to be the neural correlate underlying the type of short-term memory known as 'working' memory in the prefrontal cortex of monkeys and humans. Much more realistic and physiologically plausible models of cortical layers have been studied within the context of working memory (e.g. [110]). The central feature of all such models is the ability of the network to sustain elevated activity through recurrent excitatory connections. Not much attention has been given to heterogeneities in network topology or to long-range excitatory connections. The work presented here suggests a closer look at the possible role of these factors in generating and maintaining the active state in more realistic models.

Central to the computational usefulness of bistability in the level of activity of a network is its robustness to perturbation. For neural networks in particular, such external perturbations are often in the form of a low level of noisy background activity due to the integration of many uncorrelated inputs. Such inputs result in a low, seemingly stochastic firing rate in real cortical neurons (a few Hz). We note that the current model is not robust to noise levels sufficient to elicit spikes, since this would trivially initiate the on-state of the network. Such 'epileptic' behavior is to be expected from (6.4) since we have neglected the stabilizing influence of inhibition. This system could be viewed as a coarse-grained model, in which each neuron represents a small emsemble of neurons (cortical column). The firing of a neuron then represents the synchronized output from this small ensemble, while the non-firing state of the neuron may include low-level, non-synchronous firing within the ensemble.

A more realistic model that would allow for comparison with realistic firing rates, would include both inhibition and a topologically more complex local coupling. As an example of how modifiying the local coupling alone can already make the network more robust to noise, we extend the local excitatory coupling to include up to $2k$ neighbors ($w_{i,i\pm j} = 1$ for $j = 1 \ldots k$) and model long-range connections via a population of intermediate excitatory neurons which both receive input from and project to multiple adjacent neurons. Under these conditions, spontaneous activity is highly unlikely to initiate traveling pulses; a sufficiently large stimulus, synchronous across several neurons, is needed to turn the state of elevated activity on and off (cf. figure 6.16).

Even in the presence of noise, the probabilistic transition from persistent activity to failure is expected to occur, given that the noise intensity is not too large. For larger amplitude noise, qualitatively new behavior is seen. Consider figure 6.17, which shows the firing rate of a typical network for fast waves ($\tau_D = 1.0$) and eight different values of the noise amplitude increasing from top to bottom, left to right (note that $k = 1$ again). Gaussian noise with amplitude a is added to the model. Note that Gaussian noise may drive the neuron towards threshold or lower its voltage, in the latter case reflecting some inhibitory input.

The upper two panels of figure 6.17 show the case of a low density of global connections $p = 0.1$. We will refer to noise levels [1] through [8]. We see a periodic pattern in the absence of noise (top left [1]). The addition of noise can actually cause the network to switch between a number of distinct periodic patterns [2] (see figure 6.18). Larger amplitude noise causes the pattern to break up and become disordered [3] and sufficiently strong noise can even turn the activity off [4]. Once the noise is sufficiently strong to force the firing rate to zero one can properly speak of population bursts. The length of the burst decreases for increasing noise amplitude [5], [6] although the bursting itself is intermittent and does not appear to have a well-defined period. Even stronger noise causes the mean inter-burst interval (IBI) to shrink to zero [7], [8].

The lower two panels of figure 6.17 show the case of a high density of global connections ($p = 1.0$), for which activity always fails in the absence of noise [1]. The presence of noise causes synchronized population spikes [2]. Isolated spikes occur

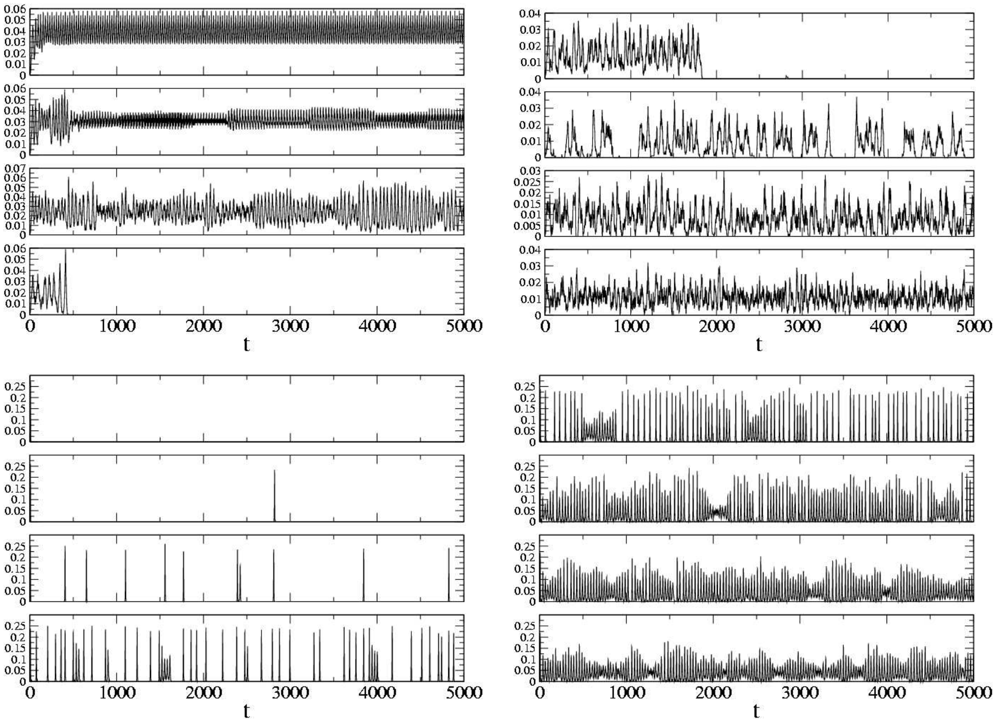

Figure 6.17: The effect of noise on the instantaneous firing rate in a system of 1000 neurons. Parameters are $\tau_D = 1.0$ and $p = 0.1, 1.0$ for the top and bottom figures respectively. Noise amplitude is $a = 0.0, 0.1, 0.2, 0.3$ (upper-left) $0.4, 0.5, 0.6, 0.7$ (upper-right) $0.0, 0.4, 0.45, 0.5$ (lower-left) and $0.55, 0.6, 0.65, 0.7$ (lower-right).

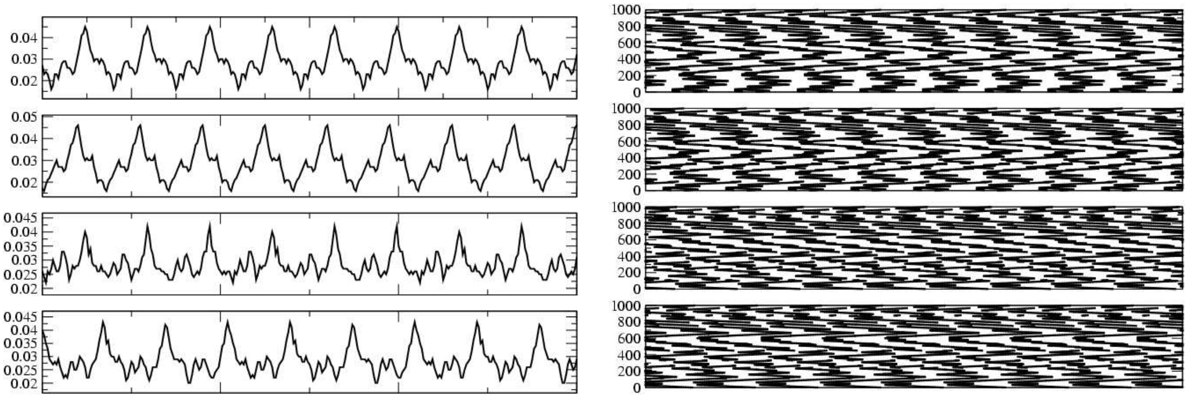

Figure 6.18: Noise can cause networks with low p to switch between various, apparently periodic attractors. The figure shows four distinct patterns which arose during the course of a single simulation for $p = 0.1$, $a = 0.01$ and $\tau_D = 1.0$. Over a dozen distinct patterns arose during the course of this simulation which was ended at a time $T = 20000$.

precisely because the network activity dies out after a single oscillation in this regime. Increasing the noise reduces the ISI [3], [4] and even causes some intermittent bursting if sufficiently strong [5]. Increasing the noise even further reduces the interval between population spikes to zero [7], [8].

Note that the persistence-failure transition discussed in section 6.2 can now be reinterpreted for various levels of noise. Section 6.2 deals with case [1], $a = 0$. For case [2] the transition is between a regular firing state in which the system explores various periodic attractors to a state of highly synchronous population spikes. For case [4] there is a transition with increasing p between population bursting with very long IBI (note that this run was not sufficiently long to include more than a single burst), and population spiking with relatively shorter ISI.

Figure 6.19 shows the effect of noise for slow waves; $\tau_D = 1.6$. Four values of p are shown $(0.1, 0.4, 0.7, 1.0)$ from top to bottom. For $p = 0.1$ the patterns are much as before, ranging from a switching between attractors [2] through bursting [5].

For $p = 1.0$, where activity in the absence of noise is long-lived [1], the addition of noise can cause activity to fail early [2]. The noisy dynamics are essentially indistinguishable from the case where noise is absent, at least as far as the firing rate is concerned. The only discernible effect is the reduction in amplitude of the modulation of the firing rate as the noise is increased [3]-[8]. The cases $p = 0.4, 0.7$ are intermediate in nature to $p = 0.1$ and $p = 1.0$.

6.5 Conclusion

We have investigated the types of network activity in the model defined by equation (6.4) as a function of the parameters p, τ_D and a which measure the density of global connections, the inverse of the speed of the waves and the noise intensity, respectively. Figure 6.20 shows a schematic representation of the network behavior as a function of these three variables, and summarizes the findings we have presented thus far.

One additional interesting aspect of the dynamics in the low p regime is the existence of a unique 'pathway' of activity. This 'pathway' is defined for a fixed network and intial condition, as the subset of neurons that, if disconnected from the rest of the network, would continue to propagate the activity normally. Consider figure 6.21, in which the 'pathway' is highlighted in red. Ignoring the initial transient, once the system has settled into a limit cycle only those neurons in red are needed to propagate the activity. The 'pathway' is determined by looking at the state of the system at long times and retracing the activity backwards, highlighting only those neurons which caused other neurons to fire later on.

We note, finally, that many of the details of the network dynamics are not fully understood. In particular, the distribution of topological chains and the use of these chains dynamically, as briefly remarked upon at the end of section 6.3, is a difficult question and, as yet, an unanswered one.

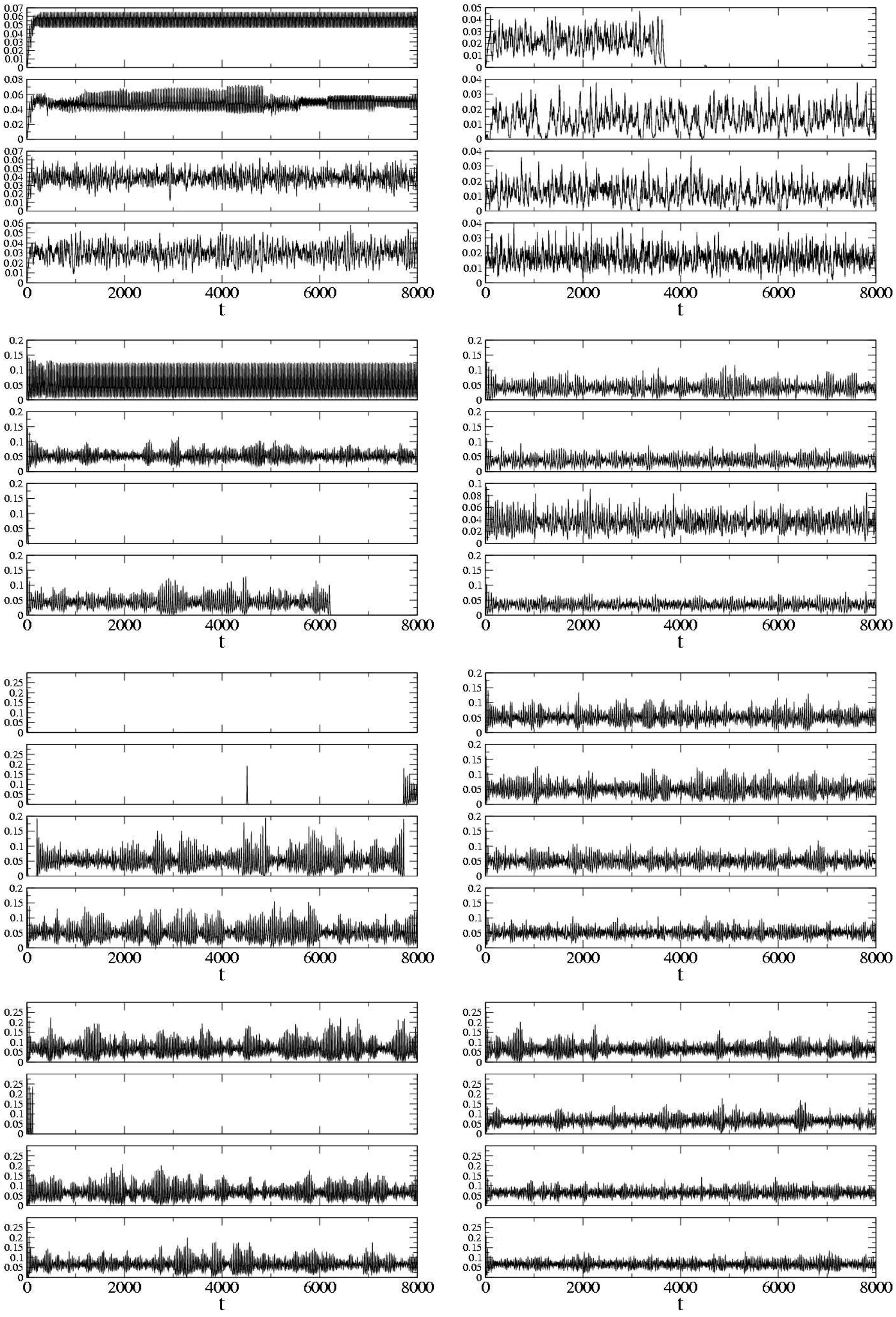

Figure 6.19: The effect of noise on the instantaneous firing rate in a system of 1000 neurons. Parameters are $\tau_D = 1.6$ and $p = 0.1, 0.4, 0.7, 1.0$ going from top to bottom. The noise amplitude for each value of p ranges between 0.0 and 0.07 from top to bottom, left to right.

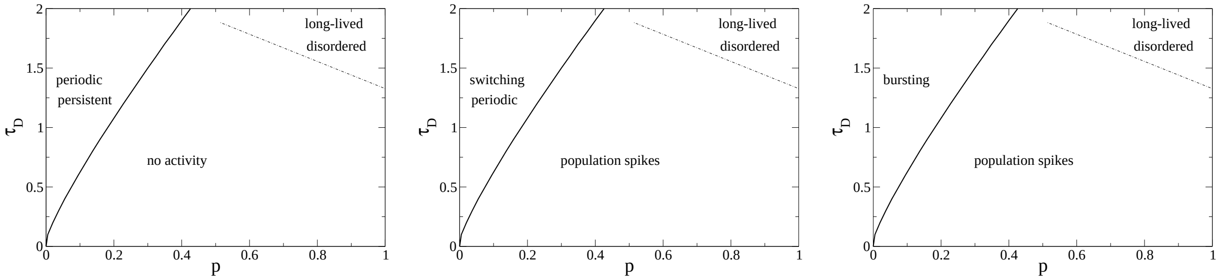

Figure 6.20: Schematic phase diagram of the network behavior for no noise, low amplitude, and high amplitude noise, respectively (left to right).

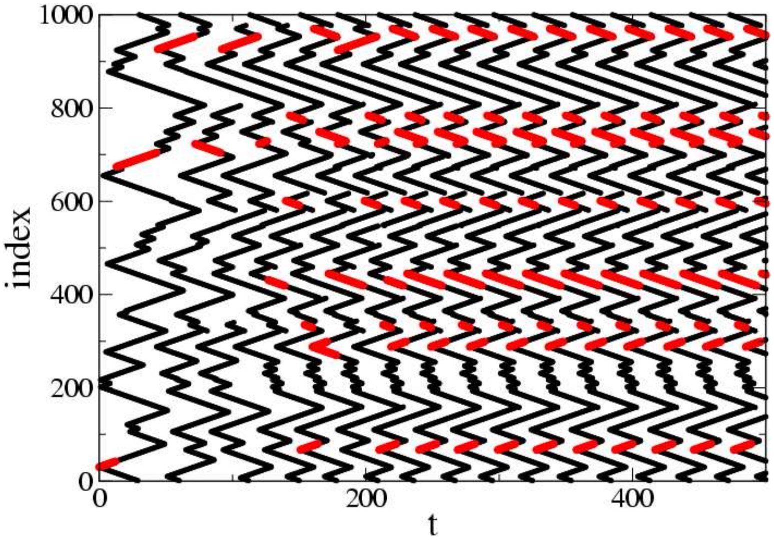

Figure 6.21: An activity 'pathway' (see text) for $p = 0.05$ and $\tau_D = 1.0$.

Appendix A

Derivation of amplitude equations

Here we outline the derivation of the amplitude equation (2.47) which describes the slow-time evolution of modulations of plane waves in (2.23, 2.24). We consider finite-wavenumber modulations p_{cr} of waves with wavenumber q_{cr} as given by (2.43) and (2.42). We first expand the phase and C-field as,

$$\begin{pmatrix} \phi \\ C \end{pmatrix} = \begin{pmatrix} q_{cr} X \\ 0 \end{pmatrix} + \epsilon \boldsymbol{\Phi_0} + \epsilon^2 \boldsymbol{\Phi_1} + \dots, \tag{A.1}$$

where $\epsilon = \sqrt{\frac{a-a_0}{a_2}}$ and a_0 is the value of the control parameter at onset of the fastest-growing mode. We rewrite (2.23, 2.24) symbolically as,

$$\mathcal{L} \begin{pmatrix} \phi \\ C \end{pmatrix} + \mathcal{N}(\phi, C) = 0, \tag{A.2}$$

and expand the linear and nonlinear operators in ϵ,

$$\mathcal{L} = L_0 + \epsilon L_1 + \epsilon^2 L_2 + \ldots, \tag{A.3}$$

$$\mathcal{N} = \epsilon^2 N_1 + \epsilon^3 N_2 + \ldots, \tag{A.4}$$

$$D_E = D + \epsilon^2 D_2, \tag{A.5}$$

with

$$L_0 = \begin{pmatrix} D\partial_X^2 - \partial_T & \frac{q_{cr}}{R^2}\partial_X \\ -2hq_{cr}\partial_X^2 & \delta\partial_X^2 - \partial_T - \alpha_2 + (s+h)\partial_X \end{pmatrix}, \tag{A.6}$$

$$L_1 = 0, \tag{A.7}$$

$$L_2 = \begin{pmatrix} D_2\partial_X^2 - \partial_\tau & R_2\partial_X \\ 0 & -\partial_\tau \end{pmatrix}, \tag{A.8}$$

$$N_1 = \begin{pmatrix} K_1 C\partial_X^2\phi + K_2\partial_X\phi\partial_X^2\phi + K_3 C\partial_X C + K_4\partial_X\phi\partial_X C, & -2h\partial_X\phi\partial_X^2\phi \end{pmatrix}^T, \tag{A.9}$$

$$N_2 = \begin{pmatrix} K_5\partial_X^2\phi(\partial_X\phi)^2 + K_6 C^2\partial_X^2\phi + K_7 C\partial_X\phi\partial_X^2\phi + K_8(\partial_X\phi)^2\partial_X C + \\ K_9 C\partial_X C\partial_X\phi + K_{10}C^2\partial_X C, \quad 0 \end{pmatrix}^T. \tag{A.10}$$

where the coefficients are given by,

$$\begin{aligned} R &= \sqrt{a_0 - q_{cr}^2}, R_2 = -\frac{a_2 q_{cr}}{R^4}, && \text{(A.11)} \\ D &= \frac{R^2 - 2q_{cr}^2}{R^2}, D_2 = \frac{a_2}{R^2}(1-D), && \text{(A.12)} \\ K_1 &= \frac{(1-D)}{R^2}, K_2 = \frac{2q_{cr}}{R^2}(D-3), && \text{(A.13)} \\ K_3 &= -\frac{q_{cr}}{R^4}, K_4 = \frac{1}{R^2}(1+\frac{2q_{cr}^2}{R^2}), && \text{(A.14)} \\ K_5 &= \frac{1}{R^2}(D-3-\frac{8a_0 q_{cr}^2}{R^4}), K_6 = -\frac{2q_{cr}}{R^6}, && \text{(A.15)} \\ K_7 &= \frac{4q_{cr}}{R^6}(q_{cr}^2 + a_0), K_8 = \frac{q_{cr}}{R^4}(3+\frac{4q_{cr}^2}{R^2}), && \text{(A.16)} \\ K_9 &= -\frac{1}{R^4}(1+\frac{4q_{cr}^2}{R^2}), K_{10} = \frac{q_{cr}}{R^6}. && \text{(A.17)} \end{aligned}$$

The slow time is given by $\tau = \epsilon^2 T$. At order ϵ we recover the homogeneous, linearized system,

$$L_0 \mathbf{\Phi_0} = 0. \tag{A.18}$$

The zero-mode $\mathbf{\Phi_0}$ we take, as in 3.1, to be of the form,

$$\mathbf{\Phi_0} = \begin{pmatrix} \Phi_0 \\ C_0 \end{pmatrix} A_0(\tau) e^{i(p_{cr}X + \omega_{cr}T)} + c.c. \tag{A.19}$$

The eigenvector $(\Phi_0, C_0)^T$ is determined by solving (A.18),

$$\begin{pmatrix} \Phi_0 \\ C_0 \end{pmatrix} = \begin{pmatrix} iq_{cr}\frac{p_{cr}}{R^2} \\ Dp_{cr}^2 + i\omega_{cr} \end{pmatrix} \tag{A.20}$$

The left-null eigenvector is found by solving the adjoint problem,

$$\mathbf{\Phi_0^\dagger} = \begin{pmatrix} 2hq_{cr}p_{cr}^2 \\ Dp_{cr}^2 - i\omega_{cr} \end{pmatrix} e^{i(p_{cr}X + \omega_{cr}T)}. \tag{A.21}$$

At O(ϵ^2) we have

$$L_0\mathbf{\Phi_1} + N_1(\mathbf{\Phi_0}) = 0. \tag{A.22}$$

The nonlinear term N_1 contributes both spatio-temporally homogeneous modes and modes of twice the critical modulation. We thus take $\mathbf{\Phi_1}$ to be of the form,

$$\mathbf{\Phi_1} = \begin{pmatrix} \Phi_{12} \\ C_{12} \end{pmatrix} A_0^2 e^{2i(p_{cr}X + \omega_{cr}T)} + c.c + \begin{pmatrix} T\Phi_{10} \\ C_{10} \end{pmatrix} |A_0|^2. \tag{A.23}$$

With this ansatz, (A.22) reduces to two linear, algebraic systems. The system corresponding to the forced second harmonic is

$$\begin{pmatrix} -4Dp_{cr}^2 - 2i\omega_{cr} & 2ip_{cr}\frac{q_{cr}}{R^2} \\ 8hq_{cr}p_{cr}^2 & -4\delta p_{cr}^2 - \alpha + 2i(s+h) - 2i\omega_{cr} \end{pmatrix} \begin{pmatrix} \Phi_{12} \\ C_{12} \end{pmatrix} + \begin{pmatrix} K_1\Phi_0C_0p_{cr}^2 + iK_2\Phi_0^2p_{cr}^3 - iK_3C_0^2p_{cr} + K_4\Phi_0C_0p_{cr}^2 \\ -2ih\Phi_0^2p_{cr}^3 \end{pmatrix} = 0, \tag{A.24}$$

and that for the homogeneous forcing

$$\begin{pmatrix} -1 & 0 \\ 0 & -\alpha \end{pmatrix}\begin{pmatrix} \Phi_{10} \\ C_{10} \end{pmatrix} + \begin{pmatrix} -K_1 p_{cr}^2(\Phi_0^* C_0 + \Phi_0 C_0^*) + K_4 p_{cr}^2(\Phi_0^* C_0 + \Phi_0 C_0^*) \\ 0 \end{pmatrix} = 0 \qquad \text{(A.25)}$$

Note that the homogeneous forcing causes a response in the phase which grows linearly with time, i.e. it changes the frequency of the wave (cf. (A.23)).

At $O(\epsilon^3)$ we have

$$L_0\mathbf{\Phi_2} + L_2\mathbf{\Phi_0} + \mathbf{N_1}(\mathbf{\Phi_0}, \mathbf{\Phi_1}) + \mathbf{N_1}(\mathbf{\Phi_1}, \mathbf{\Phi_0}) + \mathbf{N_2}(\mathbf{\Phi_0}, \mathbf{\Phi_0}, \mathbf{\Phi_0}) = 0. \qquad \text{(A.26)}$$

At this order the critical Fourier mode appears through the nonlinear forcing terms and the action of the linear operator L_2 on the eigenvalue of the linearized operator of the original system. In order for a solution to exist, these contributions must lie orthogonal to the left nullspace of the operator L_0. We thus obtain the solvability condition,

$$\langle \mathbf{\Phi_0^{\dagger}}^{*}, L_2\mathbf{\Phi_0} + \mathbf{N_1}(\mathbf{\Phi_0}, \mathbf{\Phi_1}) + \mathbf{N_1}(\mathbf{\Phi_1}, \mathbf{\Phi_0}) + \mathbf{N_2}(\mathbf{\Phi_0}) \rangle = 0, \qquad \text{(A.27)}$$

where the inner product is defined as an integral over one period of the critical Fourier mode and the scalar product of the scalar vectors in Φ, C-space. The solution of (A.27) results in a differential equation (2.47) for the complex amplitude A_0, the expression for which is extremely long and involved.

Here we follow the same procedure as in the previous derivation in outlining the derivation of the Landau equation for the amplitude-driven instability. The calculation is carried out at bandcenter, i.e. $q = 0$. We perturb the basic, plane-wave state in equations (2.50, 2.51) by expanding the real amplitude R and real field C in $\hat{\epsilon} = \sqrt{\frac{a-\hat{a_0}}{\hat{a_2}}}$ where $\hat{a_0}$ is defined as in Appendix A,

$$\begin{pmatrix} R \\ C \end{pmatrix} = \begin{pmatrix} \sqrt{\hat{a_0}} \\ 0 \end{pmatrix} + \hat{\epsilon}\boldsymbol{\Psi_0} + \hat{\epsilon}^2\boldsymbol{\Psi_1} + \ldots . \tag{A.28}$$

We rewrite (2.50, 2.51) symbolically as,

$$\mathcal{L}\begin{pmatrix} R \\ C \end{pmatrix} + \mathcal{N}(R, C) = 0. \tag{A.29}$$

We now expand the linear and nonlinear operators in ϵ,

$$\mathcal{L} = L_0 + \hat{\epsilon}L_1 + \hat{\epsilon}^2 L_2 + \ldots, \tag{A.30}$$

$$\mathcal{N} = \hat{\epsilon}^2 N_1 + \hat{\epsilon}^3 N_2 + \ldots, \tag{A.31}$$

with

$$\begin{aligned} L_0 &= \begin{pmatrix} \partial_x^2 - \partial_t - 2\hat{a_0} & \sqrt{\hat{a_0}} \\ 2h\sqrt{\hat{a_0}}\partial_x & \delta\partial_x^2 - \partial_t - \alpha + s\partial_x \end{pmatrix}, \quad (A.32) \\ L_1 &= 0, \quad (A.33) \\ L_2 &= \begin{pmatrix} -2a_2 - \partial_\tau & \frac{\hat{a_2}}{2\sqrt{\hat{a_0}}} \\ h\frac{\hat{a_2}}{\sqrt{\hat{a_0}}}\partial_x & -\partial_\tau \end{pmatrix}, \quad (A.34) \\ N_1 &= \begin{pmatrix} RC - 3\sqrt{\hat{a_0}}R^2, & 2hR\partial_x R \end{pmatrix}^T, \quad (A.35) \\ N_2 &= \begin{pmatrix} -R^3, & 0 \end{pmatrix}^T. \end{aligned}$$

(A.36)

At order $\hat{\epsilon}$ we recover the homogeneous, linearized system,

$$L_0\mathbf{\Psi_0} = 0. \quad (A.37)$$

The zero-mode $\mathbf{\Psi_0}$ we take, as in 4.1, to be of the form,

$$\mathbf{\Psi_0} = \begin{pmatrix} R_0 \\ C_0 \end{pmatrix} A_0(\tau)e^{i(p_{cr}X+\omega_{cr}t)} + c.c. \quad (A.38)$$

The eigenvector $(R_0, C_0)^T$ is determined by solving (A.37),

$$\begin{pmatrix} R_0 \\ C_0 \end{pmatrix} = \begin{pmatrix} \sqrt{\hat{a_0}} \\ p_{cr}^2 + i\omega_{cr} + 2\hat{a_0} \end{pmatrix}. \quad (A.39)$$

The left-null eigenvector is found by solving the adjoint problem,

$$\mathbf{\Psi_0^\dagger} = \begin{pmatrix} -2h\sqrt{\hat{a_0}}ip_{cr} \\ p_{cr}^2 + 2\hat{a_0} - i\omega_{cr} \end{pmatrix} e^{i(p_{cr}X+\omega_{cr}T)}. \tag{A.40}$$

At O($\hat{\epsilon}^2$) we have

$$L_0\mathbf{\Psi_1} + N_1(\mathbf{\Psi_0}) = 0. \tag{A.41}$$

The nonlinear term N_1 contributes both spatio-temporally homogeneous modes and modes of twice the critical modulation. We thus take $\mathbf{\Psi_1}$ to be of the form

$$\mathbf{\Psi_1} = \begin{pmatrix} R_{12} \\ C_{12} \end{pmatrix} A_0^2 e^{2i(p_{cr}X+\omega_{cr}T)} + c.c + \begin{pmatrix} R_{10} \\ C_{10} \end{pmatrix} |A_0|^2. \tag{A.42}$$

With this ansatz, (A.41) reduces to two linear, algebraic systems. The system corresponding to the forced second harmonic is

$$\begin{pmatrix} -4p_{cr}^2 - 2i\omega_{cr} - 2\hat{a_0} & \sqrt{\hat{a_0}} \\ 4h\sqrt{\hat{a_0}}ip_{cr} & -4\delta p_{cr}^2 - 2i\omega_{cr} - \alpha + 2isp_{cr} \end{pmatrix} \begin{pmatrix} R_{12} \\ C_{12} \end{pmatrix} + \begin{pmatrix} R_0C_0 - 3\sqrt{\hat{a_0}}R_0^2 \\ 2ihp_{cr}R_0^2 \end{pmatrix} = 0, \tag{A.43}$$

and that for the homogeneous forcing

$$\begin{pmatrix} -2\hat{a_0} & \sqrt{\hat{a_0}} \\ 0 & -\alpha \end{pmatrix} \begin{pmatrix} R_{10} \\ C_{10} \end{pmatrix} + \begin{pmatrix} R_0 C_0^* + R_0^* C_0 - 6\sqrt{\hat{a_0}}|R_0|^2 \\ 0 \end{pmatrix} = 0. \tag{A.44}$$

Solving these systems yields the following expression for the scalar quantities,

$$\begin{aligned}
R_{12} &= \frac{m_{12}}{d_{12}}, && \text{(A.45)}\\
C_{12} &= \frac{n_{12}}{d_{12}}, && \text{(A.46)}\\
m_{12} &= -\frac{1}{2}\sqrt{\hat{a_0}}(4\hat{a_0}\delta p_{cr}^2 + 4\delta p_{cr}^4 + \hat{a_0}\alpha + p_{cr}^2\alpha + 2\omega_{cr} s p_{cr} - 2\omega_{cr}^2 + i[4\delta p_{cr}^2\omega_{cr} \\
&\quad +\alpha\omega_{cr} - 2\hat{a_0} s p_{cr} - 2sp_{cr}^3 + 2\hat{a_0}\omega_{cr} + 2\omega_{cr}p_{cr}^2 + 2\hat{a_0}hp_{cr}]), && \text{(A.47)}\\
n_{12} &= -4\hat{a_0}hp_{cr}\left(-\omega_{cr} + i[\hat{a_0} + \frac{3}{2}p_{cr}^2]\right), && \text{(A.48)}\\
d_{12} &= -8\delta p_{cr}^4 - 2(\alpha + 2\hat{a_0}\delta)p_{cr}^2 - \hat{a_0}\alpha + 2\omega_{cr}(\omega_{cr} - sp_{cr}) \\
&\quad i[4sp_{cr}^3 - 4\omega_{cr}(1+\delta)p_{cr}^2 + 2\hat{a_0}p_{cr}(s+h) - \omega_{cr}(2\hat{a_0} + \alpha)], && \text{(A.49)}\\
R_{10} &= -\sqrt{\hat{a_0}} + \frac{1}{\sqrt{\hat{a_0}}}(p_{cr}^2 + 2\hat{a_0}), && \text{(A.50)}\\
C_{10} &= 0. && \text{(A.51)}
\end{aligned}$$

At cubic order projection onto the left null eigenvector yields the amplitude equation for A_0,

$$\begin{aligned}
\partial_\tau A_0 &= l(p_{cr})(p_{cr}^2 + i\omega_{cr})A_0 + l(p_{cr})\sqrt{\hat{a_0}} \\
&\quad [C_{12}\sqrt{\hat{a_0}} - 3\hat{a_0}^{3/2} + 2R_{12}(p_{cr}^2 - \hat{a_0}) + 2R_{10}(p_{cr}^2 - \hat{a_0} + i\omega_{cr})]|A_0|^2 A_0. && \text{(A.52)}\\
l(p_{cr}) &= 2ihp_{cr}\frac{\{(p_{cr}^2 + 2\hat{a_0})^2 - \omega_{cr}^2 - 2i[\omega_{cr}(p_{cr}^2 + 2\hat{a_0}) + h\hat{a_0}p_{cr}]\}}{[(p_{cr}^2 + 2\hat{a_0})^2 - \omega_{cr}^2]^2 + 4[\omega_{cr}(p_{cr}^2 + 2\hat{a_0}) + h\hat{a_0}p_{cr}]^2}. && \text{(A.53)}
\end{aligned}$$

Appendix B

Derivation of Peierls-Nabarro potential

Here we outline the derivation of the Peierls-Nabarro potential for a kink in the FK model in the limit of weak coupling ($k \to 0$). We begin by solving for the stable and unstable configurations given by

$$\sin x_i = k(x_{i+1} - 2x_i + x_{i-1}) + f. \tag{B.1}$$

Outside the region of distortion caused by the defect, the solution to B.1 is

$$x_n = 2\pi n + \psi \tag{B.2}$$

where $\psi = \sin^{-1} f$.

The defect region of the stable configuration is given by

$$\begin{aligned} x_1 &= 2\pi n + \psi \\ x_2 &= 2\pi(n+1) + \psi - \bar{x_2} \\ x_3 &= 2\pi(n+1) + \psi + \bar{x_3} \\ x_4 &= 2\pi(n+2) + \psi. \end{aligned} \tag{B.3}$$

We solve B.1 with $x_i = x_2$ which upon expanding in the small parameters $\bar{x_2}, \bar{x_3}$ yields

$$\bar{x_2} = \frac{2\pi k}{\sqrt{1-f^2}} + \mathcal{O}(k^2) \tag{B.4}$$

where we note that $\cos\psi = \sqrt{1-f^2}$. Solution of B.1 with $x_i = x_3$ reveals $x_3 = x_2$.

The defect region of the unstable configuration is given by

$$\begin{aligned} x_1 &= 2\pi n + \psi + \hat{x_1}, \\ x_2 &= 2\pi(n+1) + \pi - \psi + \hat{x_2}, \\ x_3 &= 2\pi(n+2) + \psi + \hat{x_3}, \\ x_4 &= 2\pi(n+3) + \psi. \end{aligned} \tag{B.5}$$

Solving B.1 for x_i where $i = 1, 2, 3$ respectively results in the linear system

$$\begin{pmatrix} \sqrt{1-f^2} + 2k & -k & 0 \\ -k & -\sqrt{1-f^2} + 2k & -k \\ 0 & -k & \sqrt{1-f^2} + 2k \end{pmatrix} \begin{pmatrix} \hat{x_1} \\ \hat{x_2} \\ \hat{x_3} \end{pmatrix} = \begin{pmatrix} -k(\pi + 2\psi) \\ 4k\psi \\ k(\pi - 2\psi) \end{pmatrix} \tag{B.6}$$

the soution of which is

$$
\begin{aligned}
\hat{x_1} &= \frac{-k(\pi + 2\psi)}{\sqrt{1-f^2}} + \mathcal{O}(k^2), && \text{(B.7)} \\
\hat{x_2} &= \frac{-4k\psi}{\sqrt{1-f^2}} + \mathcal{O}(k^2), && \text{(B.8)} \\
\hat{x_3} &= \frac{k(\pi - 2\psi)}{\sqrt{1-f^2}} + \mathcal{O}(k^2). && \text{(B.9)}
\end{aligned}
$$

The energies of both the stable and unstable configurations are given by

$$
E = \sum_{i=0}^{N} \left(\frac{k}{2}(x_{i+1} - xi - 2\pi)^2 + 1 - \cos x_i \right) \tag{B.10}
$$

which yields equations 4.31 and 4.32.

Note however, that these expressions break down as $f \to 1$. In this limit we scale

$$
\begin{aligned}
k &= \mathcal{O}(\epsilon) \\
f &= 1 - \epsilon \hat{f} \\
\hat{x}_i &= \mathcal{O}(\epsilon^{1/2})
\end{aligned}
$$

which leads to, for the stable configuration

$$
\begin{aligned}
\bar{x}_2 &= -\sqrt{2\bar{f}}^{1/2} \Big(1 - \sqrt{1 + \frac{2\pi k}{\bar{f}}}\Big), && \text{(B.11)} \\
\bar{x}_3 &= \sqrt{2\bar{f}}^{1/2} \Big(1 - \sqrt{1 - \frac{2\pi k}{\bar{f}}}\Big), && \text{(B.12)}
\end{aligned}
$$

and for the unstable configuration

$$\hat{x}_1 = \sqrt{2\bar{f}}\Big(1 - \sqrt{1 + \frac{k(\pi + 2\psi)}{\bar{f}}}\Big), \tag{B.13}$$

$$\hat{x}_2 = -\sqrt{2\bar{f}}\Big(1 - \sqrt{1 - \frac{4k\psi}{\bar{f}}}\Big), \tag{B.14}$$

$$\hat{x}_3 = \sqrt{2\bar{f}}\Big(1 - \sqrt{1 - \frac{k(\pi - 2\psi)}{\bar{f}}}\Big). \tag{B.15}$$

Using B.10 we arrive at equations 4.36 and 4.37.

Appendix C

Probabilities for defect generation

The variable-density Frenkel-Kontorova (vdFK) equation is given by 4.2 coupled to a rule for determining the number of particles in the chain which varies in time and space $N(x,t)$. As a simple rule we will consider the case that there is a probability that a particle is added p_+dt and a probablity that one is taken away p_-dt in a time dt. In this case, the probability that a particles have been added in a time t is given by

$$p(a,t) = \binom{n}{a} \bar{p_+}^{a} (1 - \bar{p_+})^{n-a} \tag{C.1}$$

where $n = \frac{t}{dt}$ and $\bar{p_+} = p_+dt$. This is simply a binomial distribution, which for long times (and small dt) can be approximated as a poisson distribution

$$p(a,t) \sim \frac{(p_+t)^a}{a!} e^{-p_+t}. \tag{C.2}$$

The probability density function *pdf* for s is found by C.1 with $a \rightarrow s$ and $p_+ \rightarrow p_-$.

We are concerned not with the number of particles added or taken away, but with the number of defects present $d = |a - s|$. We first note that the probability of having added a particles and taken away s particles is just

$$p(a, s) = p(a)p(s) = p(s)p(a) = p(s, a). \tag{C.3}$$

The probability of d defects is given by

$$\begin{aligned} p(|a - s| = d) &= p(s = a + d) + p(a = s + d) = p(a, a + d) + p(s + d, s) \\ &= 2 \sum_{u=0}^{n-d} p(u + d, u) \quad d \neq 0 \end{aligned} \tag{C.4}$$

which makes use of C.3. For $d = 0$ we have clearly overcounted by a factor of two, so

$$p(d = 0) = \sum_{u=0}^{n} p(u, u). \tag{C.5}$$

We choose the probabilities

$$p_+ = p + \alpha[(s - a)]_+ \tag{C.6}$$

$$p_- = p + \alpha[(a - s)]_+ \tag{C.7}$$

where $[(\cdot)]_+$ is the positive rectifying function. The term proportional to α reflects the fact that the system prefers a state with no defects $a = s$.

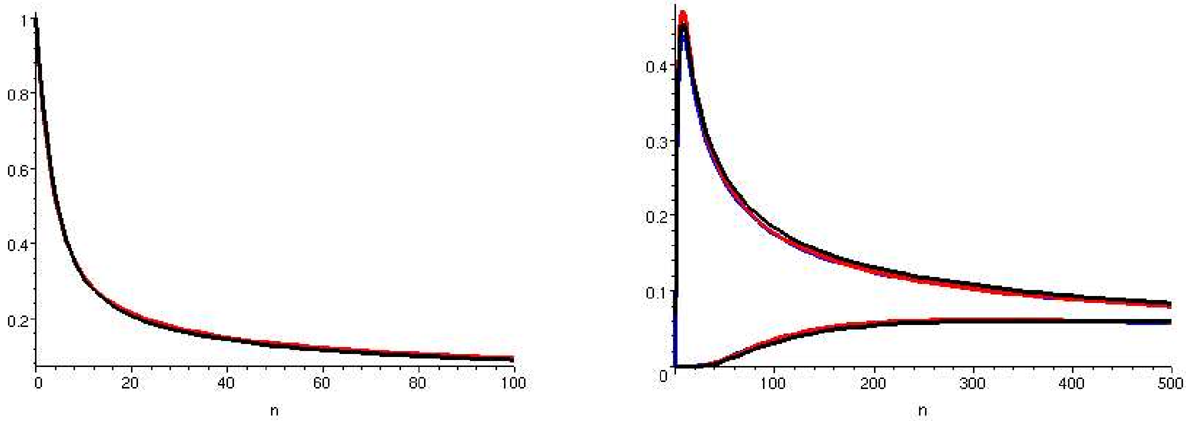

Figure C.1: Left: The probability of the defect-free state as a function of time (note that n is proportional to time, i.e. $n = \frac{t}{dt}$) for $p = 0.15$. Lines are from C.8 (black) and C.10 (red). Right: The probability of a single (top) and eight defects (bottom). Lines are C.8 (black), C.13, (red) and C.15 (blue).

For $\alpha = 0$ the sums C.5 and C.4 can be expressed in closed form [1] , yielding

$$p(d) = \begin{cases} (1-p)^{2n}\big(1-(\frac{p}{1-p})^2\big)^n P_n^0\left[\frac{1+(\frac{p}{1-p})^2}{1-(\frac{p}{1-p})^2}\right] & d = 0 \\ 2\binom{n}{d}(1-p)^{2n-2d}\Gamma(1+d)\big(1-(\frac{p}{1-p})^2\big)^n P_n^{-d}\left[\frac{1+(\frac{p}{1-p})^2}{1-(\frac{p}{1-p})^2}\right] & d > 0 \end{cases} \tag{C.8}$$

where P_n^{-d} is the Legendre function of degree n and order $-d$. Figure C.2 shows typical histograms for the number of added particles and the number of defects.

An alternative form for $p(d)$ can be derived in the limit of large n and small p. It is analogous to the derivation of the poisson distribution from the binomial distribution. Consider first the probability for $d = 0$

$$p(u,u) = \sum_{u=0}^{n}\left[\binom{n}{u}p^u(1-p)^{n-u}\right]^2. \tag{C.9}$$

---

[1] The properties of Legendre, Bessel, and Hypergeometric functions can be found in [111]

Substituting $p = \frac{\lambda}{n}$, we take the limit $n \to \infty$ keeping λ fixed, yielding

$$\begin{aligned} p(d=0) &= \sum_{u=0}^{\infty} \frac{(\lambda)^{2u}}{(u!)^2} e^{-2\lambda} \\ &= I_o(2pt) e^{-2pt} \end{aligned} \tag{C.10}$$

where I_o is the 0th order modified Bessel function. The probability for nonzero d can similarly be written

$$p(d) = \sum_{u=0}^{n-d} \binom{n}{u+d} \binom{n}{u} p^{2u+k} (1-p)^{2n-2u-k} \tag{C.11}$$

where we rewrite

$$p(d) = \sum_{u=0}^{n-k} \left[\binom{n}{u} p^u (1-p)^{n-u} \right]^2 \prod_{r=1}^{k} \left(\frac{(n-u-k+r)}{(u+r)} \right) \left(\frac{p}{1-p} \right)^k . \tag{C.12}$$

We now take the step of letting $n \to \infty$ while allowing for the possibility that the difference $n-k$ may not be large, thus retaining it in the initial sum

$$\begin{aligned} p(d) &= 2\lambda^k e^{-2\lambda} \sum_{u=0}^{n-k} \frac{\lambda^{2u}}{(u!)^2} \frac{\Gamma(n-u+1)\Gamma(u+1)}{\Gamma(u+k+1)\Gamma(n-u-k+1)} \frac{1}{n^k} \left(1 - \frac{\lambda}{n}\right)^{-k} \\ &= 2 \left(\frac{\lambda}{\left(1 - \frac{\lambda}{n}\right)} \right)^k e^{-2\lambda} \frac{\Gamma(n+1)}{n^k \Gamma(1+k) \Gamma(n-k+1)} \\ &\quad \cdot F([-n+k], [-n, 1+k], \lambda^2) \end{aligned} \tag{C.13}$$

where F is the generalized Hypergeometric function. Finally, making use of the

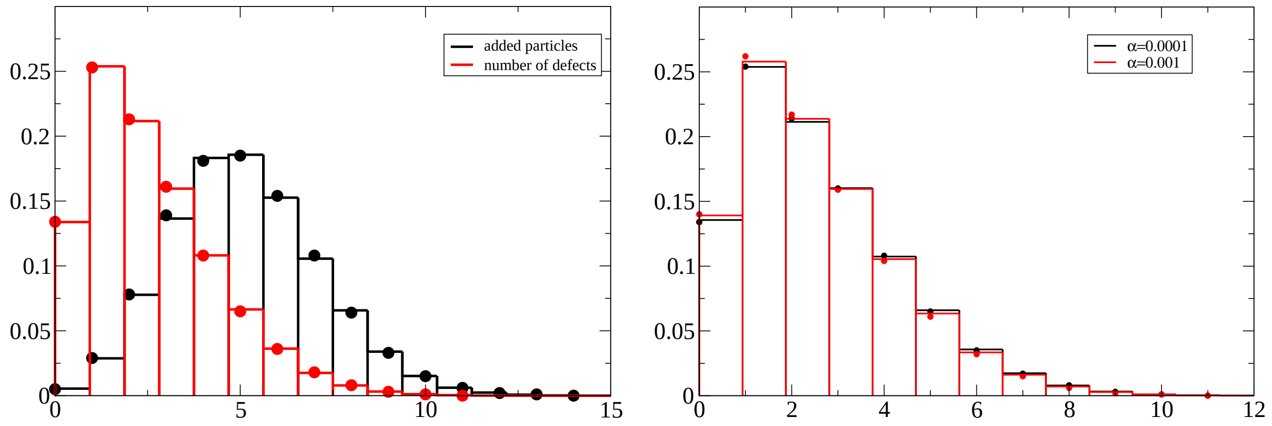

Figure C.2: Left: Numerically generated histograms for the number of added particles and number of defects respectively. Symbols are predictions from C.1 and C.8 for $n = 50$ and $p = 0.1$. Right: Histograms for nonzero α. Symbols are from C.16.

relationship

$$\lim_{n\to\infty} n^k P_n^{-d}(x) = I_d(na\cosh x) \tag{C.14}$$

we can take the limit $n \to \infty$ in C.8 yielding

$$p(d) = \begin{cases} I_0(2pt)e^{-2pt} & d = 0 \\ 2\frac{\Gamma(1+k)}{k!} I_k(2pt)e^{-2pt} & d > 0 \end{cases} \tag{C.15}$$

where I_k is the kth order modified Bessel function. Figure C.1 shows that all the above forms for the probability give equivalent results. Equations C.15 have a particularly convenient form for integration in time. The case $\alpha = 0$ is unfortunately not of interest for comparison to MD simulations.

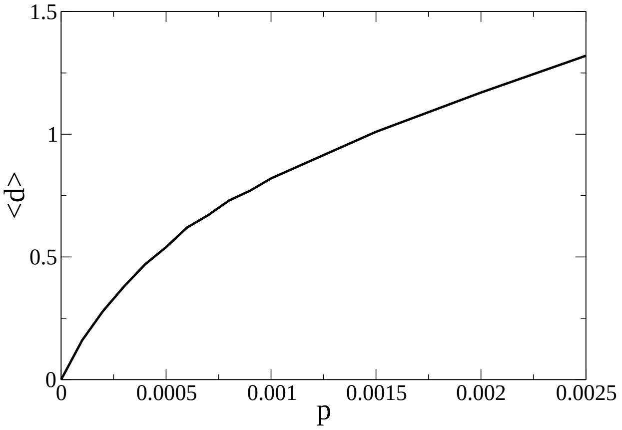

Figure C.3: Long time mean of the number of defects as a function of p for $\alpha = 0.001$.

For $\alpha \neq 0$ we have, making use of C.3,

$$p(d,\alpha) = \begin{cases} p(d,0) & d = 0 \\ 2\sum_{u=0}^{n-k} \binom{n}{u+d}\binom{n}{u} p^{u+k}(1-p)^{n-u+k}\bar{p}^u(1-\bar{p})^{n-u} & d > 0 \end{cases} \tag{C.16}$$

where $\bar{p} = p + \alpha \cdot d$.

The quantitity of interest for the determination of the slip velocity in 4.67 is the expected number of defects at long time since if $\lim_{t\to\infty} E(d(t)) = d_o$ where d_o is a constant, then one can choose a $\bar{T}$ sufficiently large such that

$$\begin{aligned} \lim_{T\to\infty} \frac{1}{T}\int_0^T dtE(d(t)) \;\; &\sim \;\; \lim_{T\to\infty} \frac{1}{T}\Big[\int_0^{\hat{T}} dtE(d(t)) + \int_{\hat{T}}^{T} dtd_o\Big] \\ &= d_o. \end{aligned} \tag{C.17}$$

See figure C.3.

References

[1] F. Charru, P. Barthelet, Secondary instabilities of interfacial waves due to coupling with a long wave mode in a two-layer Couette flow, Physica D 125 (1999) 311.

[2] B. Malomed, Patterns produced by a short-wave instability in the presence of a zero mode, Phys. Rev. A 45 (1992) 1009.

[3] H. Riecke, Self-trapping of traveling-wave pulses in binary mixture convection, Phys. Rev. Lett. 68 (1992) 301.

[4] H. Riecke, Ginzburg-Landau equation coupled to a concentration field in binary-mixture convection, Physica D 61 (1992) 253–259.

[5] M. Ipsen, P. Soerensen, Finite wavelength instabilities in a slow mode coupled complex Ginzburg-Landau equation, Phys. Rev. Lett. 84 (2000) 2389–2392.

[6] P. Matthews, S. Cox, Pattern formation with a conservation law, Nonlinearity 13 (2000) 1293–1320.

[7] P. Bartelet, F. Charru, Benjamin-Feir and Eckhaus instabilities with galilean invariance: the case of interfacial waves in viscous shear flows, Eur. J. Mech., B/Fluids 17 (1998) 1–18.

[8] M. Renardy, Y. Renardy, Derivation of amplitude equations and analysis of sideband instabilities in two-layer flows, Phys. Fluids 5 (1993) 2738.

[9] A. Bernoff, Finite amplitude convection between stress-free boundaries; Ginzburg-Landau equations and modulation theory, Euro. J. Appl. Math. 5 (1994) 267.

[10] E. Siggia, A. Zippelius, Pattern selection in Rayleigh-Bénard convection near threshold, Phys. Rev. Lett. 47 (1981) 835.

[11] F.H.Busse, E.W.Bolton, Instabilities of convection rolls with stress-free boundaries near threshold, J.Fluid Mech. 146 (1984) 115–125.

[12] P. Kolodner, Drifting pulses of traveling-wave convection, Phys. Rev. Lett. 66 (1991) 1165.

[13] W. Barten, M. Lücke, M. Kamps, Localized traveling-wave convection in binary fluid mixtures, Phys. Rev. Lett. 66 (1991) 2621.

[14] H. Riecke, G. Granzow, Localization of waves without bistability: Worms in nematic electroconvection, Phys. Rev. Lett. 81 (1998) 333.

[15] M. Dennin, G. Ahlers, D. Cannell, Chaotic localized states near the onset of electroconvection, Phys. Rev. Lett. 77 (1996) 2475.

[16] P. C. Matthews, S. M. Cox, One dimensional pattern formation with Galilean invariance near a stationary bifurcation, Phys. Rev. E 62(2) (2000) R1473.

[17] H. Riecke, Solitary waves under the influence of a long-wave mode, Physica D 92 (1996) 69–94.

[18] C. Martel, J. Vega, Dynamics of a hyperbolic system that applies at the onset of the oscillatory instability, Nonlinearity 11 (1998) 105.

[19] G. Küppers, D. Lortz, Transition from laminar convection to thermal turbulence in a rotating fluid layer, J. Fluid Mech. 35 (1969) 609.

[20] R. Clever, F. Busse, Nonlinear properties of convection rolls in a horizontal layer rotating about a vertical axis, J. Fluid Mech. 94 (1979) 609.

[21] F. Busse, K. Heikes, Convection in a rotating layer: a simple case of turbulence, Science 208 (1980) 173.

[22] Y. Hu, R. Ecke, G. Ahlers, Convection under rotation for Prandtl numbers near one: I. linear stability wavenumber selection and pattern dynamics, Phys. Rev. E 55 (1997) 6928.

[23] Y. Hu, W. Pesch, G. Ahlers, R. Ecke, Convection under rotation for Prandtl numbers near one:II Küppers-Lortz instability, Phys. Rev. E 58 (1998) 5821.

[24] K. L. Thompson, K. M. Bajaj, G. Ahlers, Traveling concentric-roll patterns in Rayleigh-Bénard convection with modulated rotation, Phys. Rev. E 65 (2002) 046218.

[25] Y. Ponty, T. Passot, P. Sulem, A new instability for finite Prandtl number rotating convection with free-slip boundary conditions, Phys. Fluids 9 (1997) 67.

[26] M. Neufeld, R. Friedrich, H. Haken, Order-parameter equation and model equation for high Prandtl number Rayleigh-Bénard convection in a rotating large aspect ratio system, Z. Phys. B 92 (1993) 243.

[27] A. Mancho, H. Riecke, F. Sain, Instabilities and spatio-temporal chaos of long-wave hexagon patterns with rotation, Chaos 12 (2002) 706.

[28] J. Millán-Rodríguez, C. Perez-Garcia, M. Bestehorn, M. Fantz, R. Friedrich, Pattern formation in convection of rotating fluids with broken vertical symmetry, Phys. Rev. A 46 (1992) 4729.

[29] M. Fantz, R. Friedrich, M. Bestehorn, H. Haken, Pattern-formation in rotating Bénard convection., Physica D 61 (1992) 147.

[30] F. Sain, H. Riecke, Instabilities and spatio-temporal chaos of hexagonal patterns with broken chiral symmetry, Physica D 144(1-2) (2001) 124.

[31] M. Cross, D. Meiron, Y. Tu, Chaotic domains: a numerical investigation, Chaos 4 (1994) 607.

[32] S. L. Pollicott, P. C. Matthews, S. M. Cox, Instability of convection in a fluid layer rotating about an oblique axis, Phys. Rev. E 67 (2003) 016301.

[33] A. Roxin, H. Riecke, Rotating convection in an anisotropic system, Phys. Rev. E 65 (2002) 046219.

[34] R. Worthing, The stability of infinite Prandtl number rotating conduction, Phys. Lett. A 237 (1998) 381.

[35] R. E. Kelly, The onset and development of Rayleigh-Bénard convection in shear flows: A review, in Physiochemical Hydrodynamics, edited by D. B. Spalding 1987, p.65 .

[36] G. A. Y. Hu, R. Ecke, Behavior of focus patterns in low Prandtl number convection, Phys. Rev. Lett. 72 (1994) 2191.

[37] R. Ecke, Y. Hu, R. Mainieri, G. Ahlers, Excitation of spirals and chiral symmetry breaking in Rayleigh-Bénard convection, Science 269 (1995) 1704.

[38] G. A. Y. Hu, R. Ecke, Convection near threshold for Prandtl numbers near one, Phys. Rev. E 48 (1993) 4399.

[39] W. Pesch, (private communication).

[40] V. Moroz, (private communication).

[41] Y. Pomeau, P. Manneville, Wavelength selection in axisymmetric cellular structures, J. Phys. (Paris) 42 (1981) 1067.

[42] M. C. Cross, P. G. Daniels, P. C. Hohenberg, E. D. Siggia, Phase-winding solutions in a finite container above the convective threshold, J. Fluid Mech. 127 (1983) 155.

[43] P. Hohenberg, L. Kramer, H. Riecke, Effects of boundaries on one-dimensional reaction-diffusion equations near threshold, Physica 15D (1985) 402–420.

[44] L. Kramer, E. Ben-Jacob, H. Brand, M. Cross, Wavelength selection in systems far from equilibrium, Phys. Rev. Lett. 49 (1982) 1891.

[45] H.-G. Paap, H. Riecke, Drifting vortices in ramped Taylor vortex flow: quantitative results from phase equation, Phys. Fluids A 3 (1991) 1519.

[46] R. Pit, H. Hervet, L. Léger, Direct experimental evidence of slip in hexadecane: Solid interfaces, Phys. Rev. Lett. 85(5) (2000) 980.

[47] Y. Zhu, S. Granick, Rate-dependent slip of a Newtonian liquid at smooth surfaces, Phys. Rev. Lett. 87(9).

[48] V. S. J. Craig, C. Neto, D. R. M. Williams, Shear-dependent boundary slip in an aqueous Newtonian liquid, Phys. Rev. Lett. 87(5) (2001) 054504.

[49] E. Bonaccurso, M. Kappl, H. J. Butt, Hydrodynamic force measurements: Boundary slip of water on hydrophilic surfaces and electrokinetic effects, Phys. Rev. Lett. 88(7) (2002) 076103.

[50] E. Bonaccurso, H.-J. Butt, V. S. J. Craig, Surface roughness and hydrodynamic boundary slip of a Newtonian fluid on a completely wetting system, Phys. Rev. Lett. 90(14) (2003) 144501.

[51] P. A. Thomson, M. O. Robbins, Shear flow near solids: Epitaxial order and flow boundary conditions, Phys. Rev. A 41(12) (1990) 6830.

[52] P. A. Thomson, S. M. Troian, A general boundary condition for liquid flow at solid surfaces, Nature 389 (1997) 360.

[53] J.-L. Barrat, L. Bocquet, Large slip effect at a nonwetting fluid-solid interface, Phys. Rev. Lett. 82(23) (1999) 4671.

[54] M. Cieplak, J. Koplik, J. R. Banavar, Boundary conditions at a fluid-solid interface, Phys. Rev. Lett. 86(5) (2001) 803.

[55] O. M. Braun, Y. S. Kivshar, Nonlinear dynamics of the Frenkel-Kontorova model, Physics Reports 306 (1998) 109.

[56] L. M. Floría, J. J. Mazo, Dissipative dynamics of the Frenkel-Kontorova model, Advances in Physics 45(6) (1996) 505.

[57] F. G. Bass, Y. S. Kivshar, V. V. Konotop, Y. A. Sinitsyn, Dynamics of solitons under random perturbations, Physics Reports 157(2) (1988) 63.

[58] Y. S. Kivshar, B. A. Malomed, Dynamics of solitons in nearly integrable systems, Rev. Mod. Phys. 61(4) (1989) 763.

[59] D. Menzel, Water on a metal surface, Science 295 (2002) 8.

[60] S. Aubry, P. Y. L. Daeron, The twist map, the extended Frenkel-Kontorova model and the devil's staircase, Physica D 8 (1983) 381.

[61] S. N. Coppersmith, D. S. Fisher, Pinning transition of the discrete sine-Gordon equation, Phys. Rev. B 28(5) (1983) 2466.

[62] T. Strunz, F.-J. Elmer, Driven Frenkel-Kontorova model. I Uniform sliding states and dynamics domains of different particle densities, Phys. Rev. E 58(2) (1998) 1601.

[63] T. Strunz, F.-J. Elmer, Driven Frenkel-Kontorova model. II. Chaotic sliding and nonequilibrium melting and freezing, Phys. Rev. E 58(2) (1998) 1612.

[64] M. Paliy, O. Braun, T. Dauxios, B. Hu, Dynamical phase diagram of the dc-driven underdamped Frenkel-Kontorova chain, Phys. Rev. E 56(4) (1997) 4025.

[65] O. M. Braun, A. R. Bishop, J. Röder, Hysteresis in the underdamped driven Frenkel-Kontorova model, Phys. Rev. Lett. 79(19) (1997) 3692.

[66] O. M. Braun, Y. S. Kivshar, Kinks in a system of adatomic chains, J. Phys.: Condens. Matter 2 (1990) 5961.

[67] B. Ermentrout, Type I membranes, phase resetting curves, and synchrony, Neural Computation 8 (1996) 979.

[68] C. Willis, M. El-Batanouny, P. Stancioff, Sine-Gordon kinks on a discrete lattice. i. Hamiltonian formalism, Phys. Rev. B 33(3) (1986) 1904.

[69] S. N. Coppersmith, D. S. Fisher, Threshold behavior of a driven incommensurate harmonic chain, Phys. Rev. A 38(12) (1988) 6338.

[70] B. Li, D. Y. Kwok, Discrete Boltzmann equation for microfluidics, Phys. Rev. Lett. 90(12) (2003) 124502.

[71] V. P. Sokhan, D. Nicholson, N. Quirke, Fluid flow in nanopores: An examination of hydrodynamic boundary conditions, J. of Chem. Phys. 115(8) (2001) 3878.

[72] S. Lichter, A. Roxin, S. Mandre, Slip at a liquid-solid interface, preprint .

[73] M. J. Z. et al. (Ed.), Fundamental Neuroscience, Academic Press, 1999.

[74] D. G. Amaral, M. P. Witter, The Rat Nervous System, 2nd Edition, Academic Press, Inc., 1995, Ch. Hippocampal Formation, p. 443.

[75] T. F. Freund, G. Buzsáki, Interneurons of the hippocampus, Hippocampus 6 (1996) 347.

[76] R. Bartesaghi, T. Gessi, Activation of perforant path neurons to field CA1 by hippocampal projections, Hippocampus 13 (2003) 193.

[77] P. Vetter, A. Roth, M. Häusser, Propagation of action potentials in dendrites depends on dendritic morphology, J. Neurophysiol 85 (2001) 926.

[78] N. L. Golding, W. L. Kath, N. Spruston, Dichotomy of action-potential back-propagation in CA1 pyramidal neuron dendrites, J. Neurophysiol 86 (2001) 2998.

[79] M. Migliore, D. A. Hoffman, J. C. Magee, D. Johnston, Role of an A-type K+ conductance in the back-propagation of action potentials in the dendrites of hippocampal pyramidal neurons, J. Comp. Neuroscience 7 (1999) 5.

[80] M. Megias, Z. Emri, T. F. Freund, A. I. Gulyas, Total number and distribution of inhibitory and excitatory synapses on hippocampal CA1 pyramidal cells, Neuroscience 102 (2001) 527.

[81] G. Stuart, N. Spruston, B. Sakmann, M. Häusser, Action potential initiation and backpropagation in neurons of the mammalian CNS, TINS 20 (1997) 125.

[82] N. L. Golding, N. Spruston, Dendritic sodium spikes are variable triggers of axonal action potentials in hippocampal CA1 pyramidal neurons, Neuron 21 (1998) 1189.

[83] M. Remondes, E. M. Schumann, Direct cortical input modulates plasticity and spiking in CA1 pyramidal neurons, Nature 416 (2002) 736.

[84] J. Trimmer, (private communication) .

[85] E. M. Izhikevich, Class I neural excitability: conventional synapses, weakly connected networks, and mathematical foundations of pulse-coupled models, IEEE 10 (1999) 499.

[86] P. C. Bressloff, S. Coombes, A dynamical theory of spike train transitions in networks of integrate-and-fire oscillators, SIAM J. Appl. Math. 60 (2000) 820.

[87] N. Brunel, V. Hakim, Fast global oscillations of integrate-and-fire neurons with low firing rates, Neural Computation 11 (1999) 1621.

[88] N. Brunel, Dynamics of networks of randomly connected excitatory and inhibitory spiking neurons, J. Physiol. (Paris) 94 (2000) 445.

[89] N. Brunel, Dynamics of sparsely connected networks of excitatory and inhibitory spiking neurons, J. Comp. Neuroscience 8 (2000) 183.

[90] V. B. Mountcastle, The columnar organization of the neocortex, Brain 120 (1997) 701.

[91] G. González-Burgos, G. Barrionuevo, D. A. Lewis, Horizontal synaptic connections in monkey prefrontal cortex: An in vitro electrophysiological study, Cerebral Cortex 10 (2000) 82.

[92] J.-Y. Wu, L. Guan, Y. Tsau, Propagating activation during oscillations and evoked responses in neocortical slices, J. Neurosci. 19 (1999) 5005.

[93] R. Demir, L. B. Haberly, M. B. Jackson, Epileptiform discharges with in-vivo-like features in slices of rat piriform cortex with longitudinal association fibers, J. Neurophys. 86 (2001) 2445.

[94] C. van Vreeswijk, L. F. Abbott, Self-sustained firing in populations of integrate-and-fire neurons, SIAM J. Appl. Math. 53 (1993) 253.

[95] D. Hansel, G. Mato, C. Meunier, Synchrony in excitatory neural networks, Neural Computation 7 (1995) 307.

[96] P. C. Bressloff, S. Coombes, Desynchronization, mode locking and bursting in strongly coupled integrate-and-fire oscillators, Phys. Rev. Lett. 81 (1998) 2168.

[97] P. H. Chu, J. G. Milton, J. D. Cowan, Connectivity and the dynamics of integrate-and-fire neural networks, Int. J. Bif. Chaos 4 (1994) 237.

[98] D. J. Watts, S. H. Strogatz, Collective dynamics of 'small world' networks, Nature 393 (1998) 440.

[99] A. D. Sánchez, J. López, M. A. Rodriguez, Nonequilibrium phase transitions in directed small-world networks, Phys. Rev. Lett. 88 (2002) 048701.

[100] A. Pekalski, Ising model on a small-world network, Phys. Rev. E 64 (2001) 057104.

[101] B. J. Kim, H. Hong, P. Holme, G. S. Jeon, P. Minnhagen, M. Y. Choi, XY model in small-world networks, Phys. Rev. E 64 (2001) 056135.

[102] M. Kuperman, G. Abramson, Small world effect in an epidemiological model, Phys. Rev. Lett. 86 (2001) 2909.

[103] L. F. Lago-Fernández, R. Huerta, F. Corbacho, J. A. Sigüenza, Fast response and temporal coherent oscillations in small-world networks, Phys. Rev. Lett. 84 (2000) 2758.

[104] M. Barahona, L. M. Pecora, Synchronization in small-world systems, Phys. Rev. Lett. 89 (2002) 054101.

[105] H. Hong, M. Y. Choi, B. J. Kim, Synchronization on small-world networks, Phys. Rev. E 65 (2002) 026139.

[106] X. F. Wang, G. Chen, Synchronization in small-world dynamical netoworks, Int. J. Bif. Chaos 12 (2002) 187.

[107] M. E. J. Newman, D. J. Watts, Scaling and percolation in the small-world network model, Phys. Rev. E 60 (1999) 7332.

[108] M. E. J. Newmann, C. Moore, D. J. Watts, Mean-field solution of the small-world network model, Phys. Rev. Lett. 84 (2000) 3201.

[109] J. D. G. Eran Rabani, B. J. Berne, Direct observation of stretched-exponential relaxation in low-temperature Lennard-Jones systems using the cage correlation function, Phys. Rev. Lett. 82 (1999) 3649.

[110] A. Compte, N. Brunel, P. S. Goldman-Rakic, X.-J. Wang, Synaptic mechanisms and network dynamics underlying spatial working memory in a cortical network model, Cereb. Cortex 10 (2000) 910.

[111] M. Abramowitz, I. Stegun (Eds.), Handbook of Mathematical Functions, Dover, 1972.